DOCTORAL DISSERTATION

THERMODYNAMIC STUDY ON PHYSISORBED MONOLAYERS OF SIMPLE MOLECULES ON GRAPHITE SURFACE

A Dissertation Presented

by

TATSUYA SHIRAKAMI

Submitted to the Graduate School
of Faculty of Science,
Osaka University.
in partial fulfillment of the
requirements for the degree of
Doctor of Science

September, 1992

Department of Chemistry

Acknowledgments

I would like to express my most sincere thanks to Emeritus Professor Hideaki Chihara for his valuable suggestions as my former supervisor. Under his guidance throughout my undergraduate and graduate courses I could learn much about the thermodynamics, surface chemistry and other related fields.

I wish to express my gratitude to Professor Hiroshi Suga for his critical reading of the manuscript and for his instructive suggestion.

I am indebted for Professor Kizashi Yamaguchi's kindness to give me the good circumstances for writing this dissertation.

I am also very grateful to Dr. Akira Inaba for his introducing me to detailed techniques of thermodynamic measurements, and for his repeated encouragement, many critical advices and stimulated suggestions throughout the course of this study.

Finally, I gratefully acknowledge many valuable discussions by the members of Quantum Chemistry Laboratory. Especially I am indebted to Mr. Kenji Kawagishi. I was often stimulated by his novel and eccentric opinions.

Abstract

Thermodynamic investigations have been carried out for the monolayers of simple molecules adsorbed on the surface of graphite. As the admolecules, Kr, N_2, CO/N_2 mixture, CH_4 and CD_4 were selected. All the molecules are expected to form a $\sqrt{3}\times\sqrt{3}$ commensurate structure on the substrate at low coverages.

The heat capacity of the Kr monolayer showed new anomalies at 49.2 and 80.5 K, near the boundary coverage of the commensurate and the incommensurate phases. This fact suggests the existence of re-entrant fluid phase between them.

The vibrational state of the Kr monolayer is deduced from the heat capacity. The phonon density of states has two cut-offs, one at the high-frequency end and the other at the low-frequency end. The latter comes from the surface corrugation of the substrate.

For the system of N_2 on graphite, an orientational order-disorder phase transition with respect to molecular axis was found at 24 K for the triangular incommensurate monolayer. The commensurate-incommensurate phase transition was also found at 67.6 K.

The vibrational state of the N_2 monolayer is considered by using a simple lattice dynamics. The feature is described in terms of the density of states for the three phases with different coverages; commensurate, uniaxially compressed incommensurate, and triangular incommensurate phases. The heat capacity of the mixture of CO and N_2 on graphite suggested that CO and N_2 were miscible at any composition even on the graphite surface. It is also suggested from the analysis of the mixing entropy that the mixture forms a Wannier lattice.

An anomalous heat capacity was found at 32 K for the commensurate CD_4 monolayer, which is due to the rotational phase transition.

For CH_4 on graphite, conversion between the different spin species of the molecule was found to be very slow. Introduction of a small amount of O_2 allowed us to determine the equilibrium heat capacity including the spin system. The results support the energy scheme which was determined previously by changing the temperature, the coverage and the concentration of O_2.

Contents

Chapter I Introductory Remarks

I-1 Introduction

The physical adsorption of simple molecules on solid surfaces has received much attention over the years both experimentally and theoretically. The structure and properties of physisorbed layers can provide a means for studying the balance between surface-molecule and molecule-molecule interactions. These forces may lead to a variety of structures with similar energies, as is often manifested in a complex phase diagram in the sub-monolayer region.

One of the highlights of the study is thus the understanding of the dynamical properties of physisorbed monolayers. An early study of the Ar monolayer on graphite by inelastic neutron scattering study (ref. 1) delineated the two-dimensional nature of the vibrational properties: The in-plane modes can be described by two-dimensional harmonic-phonons, whereas the out-of-plane modes are almost dispersionless although a coupling with the collective motions of the graphite substrate cannot be ignored. The quantitative understanding of the dynamical properties, however, still remains poor because of the lack of the details of surface-molecule interactions. In principle, the heat of adsorption can give the direct information, but unfortunately it is not sensitive enough to see the details. Instead, as will be discussed, it turned out that the low temperature heat capacity of the adsorbed monolayers carries fruitful information on the dynamical properties.

I-2 Effect of Surface Corrugation

If the two-dimensional solid to be considered has no substrate underneath, which is called as a floating monolayer (ref.2), and it is spread out boundlessly, then the vibrational state would be simple because of the dimensionality and the continuity. A simple argument allows us to apply the two-dimensional Debye model, in which the vibrational properties are

characterized by only one parameter, ν_D, the Debye's cut-off frequency. The heat capacity thus obeys the Debye's T^2 law at sufficiently low temperatures. In actual system, however, the size of the adsorbed monolayer as well as that of the substrate are limited. Moreover, the existence of the surface corrugation may change the vibrational state substantially. Therefore such effects ought to be assessed when the experimental heat capacity is analyzed.

The realization of a "commensurate" phase is the most prominent effect of the surface corrugation. Admolecules are arranged along the periodic potential produced externally by the substrate. Because of the absence of any invariant for lateral translation in this circumstance, the acoustic normal modes in the monolayer have necessarily a nonzero minimum value of the frequency at the Brillouin-zone center. This is a logical consequence from the group theory (ref. 6). In other words, there is another cut-off frequency, ν_c, at the low-frequency end in the phonon density of states. The heat capacity thus changes exponentially at low temperatures (ref. 3).

$$C \propto (h\nu_c/kT)\exp(-h\nu_c/kT). \qquad \text{(I-1)}$$

The vibrational properties of commensurate solid can therefore be characterized by two parameters ν_c and ν_D, or the corresponding characteristic temperatures Θ_c and Θ_D.

According to the Steele's Fourier representation, the adatom-substrate potential (ref. 4) can be written as

$$V(\vec{r},z) = V(z) + \Sigma\, V_g(z)\exp(i\vec{g}\cdot\vec{r}), \qquad \text{(I-2)}$$

where $\vec{r}$ is a vector parallel to the surface, $\vec{g}$ is the reciprocal lattice vector for the substrate surface, and z is the distance between the adatom and the substrate. In the case of spherical admolecules adsorbed on the site of three-fold or higher symmetry, such as rare gases on graphite, the magnitude of the potential V_g is directly related to the ν_c. Since the V_g vanishes exponentially with increasing $|\vec{g}|$, the

first reciprocal lattice would be enough to be taken into account. Thus the second term of Eq. (I-2) is approximately given by

$$\Sigma\, V_g(z)\exp(i\vec{g}\cdot\vec{r}) \simeq 2V_g \{\cos[4\pi x/a_0] + \cos[2\pi(x-y\sqrt{3})/a_0] + \cos[2\pi(x+y\sqrt{3})/a_0]\}, \quad \text{(I-3)}$$

where $\vec{r} = x\vec{i} + y\vec{j}$ and a_0 is the nearest neighbor distance (ref. 5). The second derivative of this equation gives the ν_c as

$$\nu_c = 2(-3V_g/m)^{1/2}/a_0, \quad \text{(I-4)}$$

where m is the mass of the adatom (ref. 6). The Eqs. I-1 and I-4 are thus what we need to deduce the vibrational state of the monolayer from the heat capacity data.

In the case of incommensurate solids, the situation is rather complicated. A perturbation theory (ref. 7) demonstrated that the structure is degenerate. The low temperature heat capacity may be useful for the characterization of this situation. The vibrational spectrum is expected to start from zero frequency, because of the translational invariance for the lateral arrangement of molecules in monolayer with respect to their centers of mass.

I-3 Two-dimensional Molecular Solid

The solid overlayer can be regarded as one of the polymorphs, a two-dimensional molecular solid, receiving a field offered by the neighboring molecules and the substrate. The site symmetry is now completely different from that in the bulk solid. Such situation stimulates our interest in many ways.

Is there any phase transition which is inherent in the two-dimensional system? Some of the bulk solids have residual entropies, indicating that some disorder is frozen in at low temperatures. A new phase transition can be expected to appear in the adsorbed system.

How is the miscibility problem? Since the molecules of the binary system are forced to sit on a particular site in the commensurate phase, only the composition of the mixture can be changed at will in the actual experiment. All other intensive variables as well as the lattice parameters are fixed. The way of ordering of the mixture is thus one of the subjects to be examined.

How is the methane problem in the adsorbed system? Methane molecules show the rotational tunneling. The splitting of the rotational ground state strongly depends upon the site symmetry and the strength of the field. The nuclear spin species may convert with each other in different ways. How do they behave in the adsorbed system?

Overall, the objective of the present study is to investigate the adsorbed monolayers on graphite from thermodynamic point of view. Low temperature heat capacities were measured by using two types of calorimeter for this purpose. Several systems of some simple molecules were selected: krypton (Chapter II), nitrogen (Chapter III), mixture of CO/N_2 (Chapter IV) and methane (Chapters V and VI).

References to Chapter I

1. H. Tube, K. Carneiro, J.K. Kjems, L. Passell and J.P. McTague, *Phys. Rev.* B16, 4551 (1977).
2. L.K. Moleko, B. Joos, J.M. Hakim, H.R. Glyde and S.T. Chui, *Phys. Rev.* B34, 2815 (1986).
3. J.G. Dash, *Films on Solid Surfaces*, Academic Press, New York, (1975).
4. W.A. Steele, *Surf. Sci.* 36, 317 (1973).
5. T.M. Hakim, H.R. Glyde and S.T. Chui, *Phys. Rev.* B37, 974 (1988).
6. L.W. Bruch, *Phys. Rev.* B37, 6658 (1988).
7. S.C. Ying, *Phys. Rev.* B3, 4160 (1971).

Chapter II Krypton on Graphite

II-1 Introduction

The monolayer of krypton adsorbed on the surface of graphite has been considered to be a prototype for studying the physical adsorption. Graphite provides a uniform basal plane and krypton is the simplest molecule. Structual aspect of the system can be studied by various methods, including x-ray and neutron diffractions and LEED. Thus the system has been widely investigated over the years (refs. 1-8). However, the simple molecules did not lead us simple results. It turned out that the surface corrugation of graphite plays an important role in determining the phase behavior and the structure of the monolayer.

At low coverages, krypton forms a ($\sqrt{3}\times\sqrt{3}$) triangular commensurate structure (Fig. II-1) at low temperatures, in which the nearest neighbor distance between the adatoms is expanded by about 6 % compared with that of the bulk solid. According to an EXAFS study (ref. 8), krypton atoms sit on the center of the hexagon of graphite. As the coverage is increased, the commensurate phase transforms into an incommensurate (but still triangular) solid phase, where the interatomic distance is almost the same as that in the bulk solid (ref. 2). The transition between the two solid phases was originally found by an isotherm measurement (ref. 1) and the melting process was examined by an x-ray scattering (ref. 3). A complete phase diagram was then obtained by heat capacity measurements (refs. 4 and 5). However, a synchrotron x-ray scattering study (refs. 6 and 7) came out later. The result suggested that the commensurate phase does not transform directly into the incommensurate phase, but does transform through a fluid phase. It was claimed that a re-entrant fluid phase should exist between the two phases.

The aim of the subject here is three-fold. Firstly, we investigate the phase diagram near the monolayer completion region to detect the transition between the commensurate and incommensurate phases. Secondly, we apply the two-dimensional

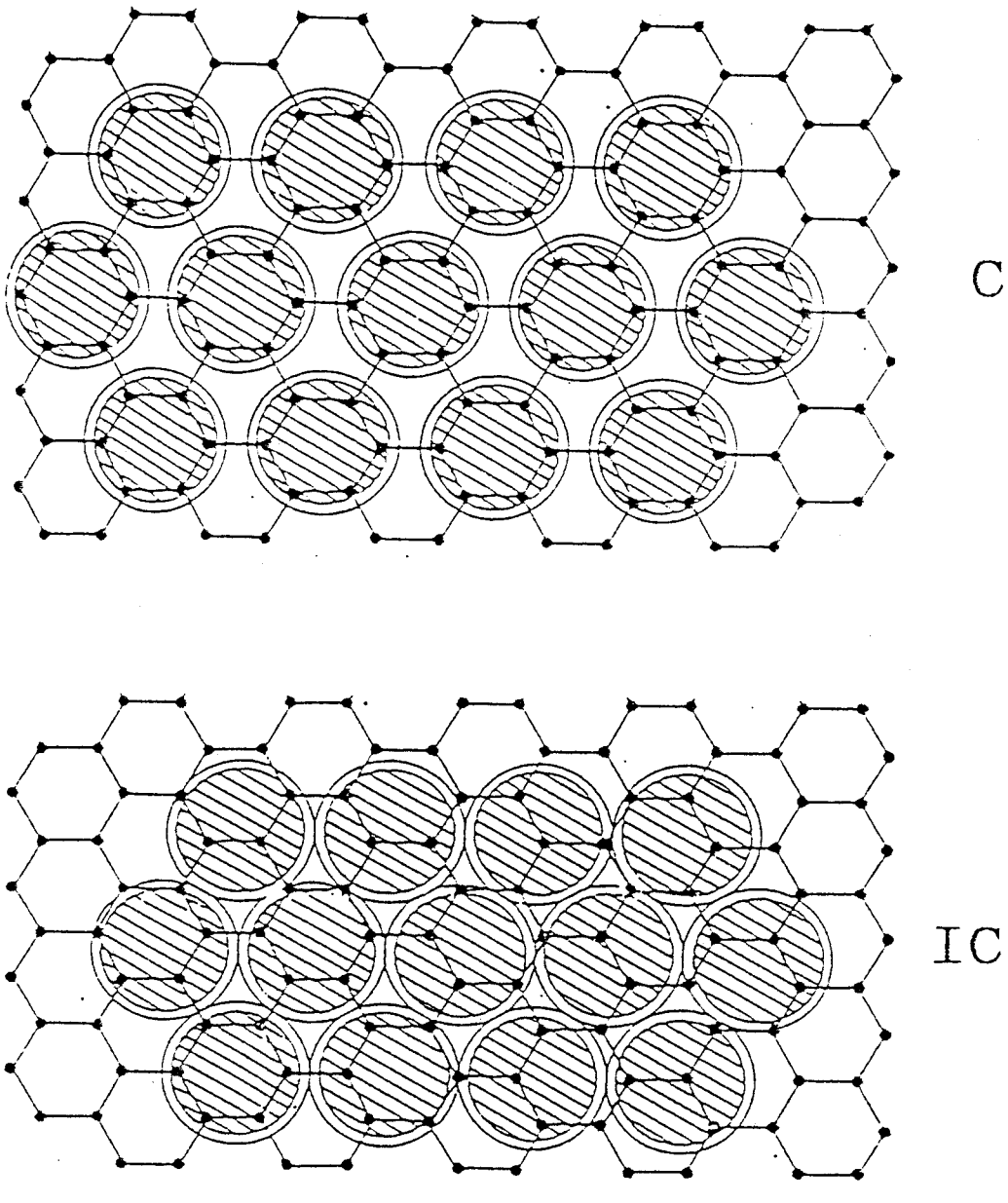

Fig. II-1 Schematic drawings of Kr monolayers on graphite (ref. I-1). C, commensurate phase; IC, incommensurate phase

Debye model to the monolayer for the investigation of the vibrational properties. Thirdly, we estimate the amplitude of the surface corrugation of graphite. In order to achieve this, we measured the heat capacity of krypton/graphite in the temperature range 3 ~ 120 K.

II-2 Experimental Details

An adiabatic calorimeter assembly, which has been described previously (ref. 9), was employed for the measurement. A new calorimeter vessel (fig. II-2) made of copper was equipped with a needle valve. It carried a platinum resistance thermometer (R_0 = 100 Ω, MINCO Inc.), and germanium resistance thermometer (SI Inc.) and a heater (ref. 10). The resistance of the platinum thermometer was measured by an a.c. resistance bridge (model 5840D, H. Tinsley & Co., Ltd.), while that of the germanium thermometer was measured by a digital multimeter (model TR-6877D, Takeda Riken Industries Co., Ltd.). The temperature scales used are the IPTS-68 for the platinum thermometer above 14 K, and the helium gas thermometric scale and the helium-4 vapor pressure scale for the germanium thermometer below 15 K.

The graphite specimen used as a substrate was Grafoil MAT (7.67 g), which was obtained from Union Carbide. It had a specific surface area of 24 m^2g^{-1} (ref. 11). The sheets were packed tightly into the vessel and heated to 400 °C *in vacuo* before use. Krypton gas of research purity (99.99 %), purchased from Takachiho Kagaku, was purified further by fractional distillation before placed in the calorimetric vessel. The amount of the gas to be introduced was measured by using a calibrated bulb (410.22 cm^3) and a Baratron gage (0-1000 torr* type, MKS Instr. Inc.), both of which were connected to the gas handling system. Four coverages were explored; 1.42, 1.60, 2.00 and 2.20 mmol. The former two correspond to the commensurate coverage and the last to the incommensurate one at low temperatures. The amount of 2.00 mmol seems to lie very close

---

* 1 torr ≡ 101325/760 Pa.

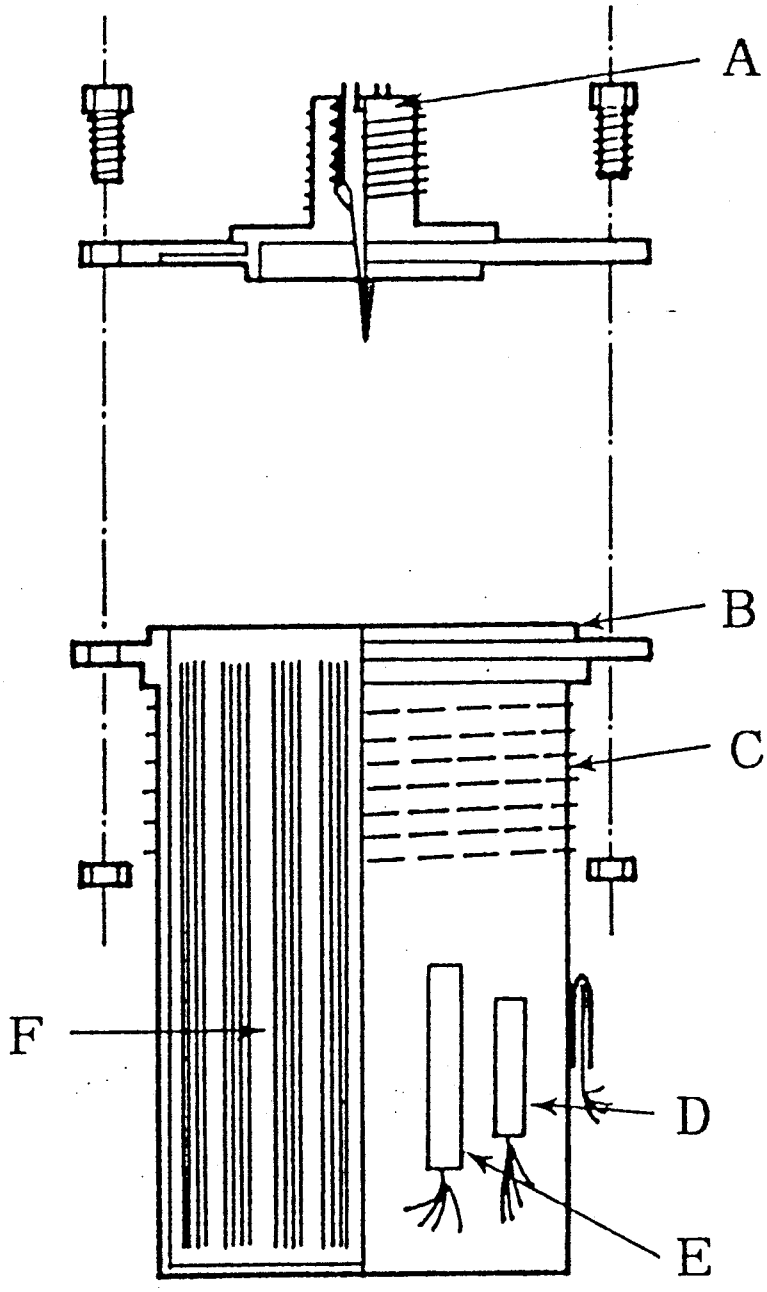

Fig. II-2 The calorimeter vessel. A, needle valve; B, indium seal; C, heater; D, germanium resistance thermometer; E, platinum resistance thermometer; F, graphite.

to the boundary between the commensurate and incommensurate phases.

II-3 Results and Discussion

II-3-1 Heat Capacity

The heat capacity of the adsorbed layers was determined from the difference between that of the calorimeter, substrate and admolecules and that of the calorimeter and substrate only. The molar heat capacities obtained between 3 and 120 K for n_s = 1.42, 1.60, 2.00 and 2.20 mmol are listed in Table II-1, II-2, II-3 and II-4, respectively. They are illustrated in Figs. II-3, II-4, II-5 and II-6, respectively. Since desorption of krypton inside the calorimetric vessel became significant at higher temperatures, the amount adsorbed was corrected for by using additional information.

II-3-2 Phase Diagram

The heat capacity peak due to the melting we obtained was consistent with the phase diagram determined from the previous heat capacity measurement by Butler *et al.* (ref. 5), as shown in Fig. II-7. In addition, two small but sharp anomalies in heat capacity were found at 49.2 K and 80.5 K for n_s = 2.00 mmol (Fig. II-8, ref. 12). Therefore we have two possibilities to correlate these new anomalies with the phase sequence at this coverage; either [incommensurate → re-entrant fluid → commensurate] or [commensurate → incommensurate → commensurate] with increasing temperature. As will be discussed later, the low temperature heat capacity suggested that the former is more probable than the latter, namely that the lowest temperature phase would be incommensurate. Coppersmith *et al.* indicated that any weakly incommensurate solid which is adjacent to the commensurate phase cannot be stabilization due to spontaneous creation of dislocations (ref. 23), and predicted that such phase behaves consequently as "liquid" with exponential decay of

Table II-1 Molar heat capacity of Kr on graphite for n_a = 1.42 mmol.

T / K	C_m / $JK^{-1}mol^{-1}$	T / K	C_m / $JK^{-1}mol^{-1}$	T / K	C_m / $JK^{-1}mol^{-1}$
2.639	0.450	5.452	4.149	72.179	32.49
2.908	0.542	6.154	5.341	73.821	33.85
3.185	0.985	7.037	6.921	75.330	36.11
3.496	1.264	7.980	8.429	76.765	37.93
3.852	1.753	8.887	9.667	78.026	40.37
4.280	2.373	9.852	10.913	79.064	42.58
4.801	3.069	10.863	12.296	79.987	44.21
5.317	3.900	12.712	14.591	80.852	46.63
5.915	4.969	14.101	15.802	81.675	51.88
6.673	6.280			82.436	58.21
7.500	7.732	15.052	16.70	83.149	66.40
8.372	9.014	16.046	16.90	83.744	78.19
9.243	10.063	17.191	17.79	84.211	95.56
10.102	11.334	18.401	18.70	84.668	128.19
11.015	12.619	19.579	19.37	85.089	174.00
12.043	13.666	20.804	20.31	85.481	223.44
13.151	14.868	22.031	20.71	85.876	248.96
14.344	16.016	23.214	20.89	86.271	239.21
		24.364	21.13	86.667	215.71
2.726	0.611	25.538	21.37	87.180	192.86
3.023	0.865	26.724	21.42	87.809	166.96
3.336	1.231	28.013	22.04	88.438	145.13
3.662	1.532	29.385	22.38	89.064	119.70
4.066	1.974	30.894	22.59	89.741	75.80
4.526	2.588	32.672	22.82	90.638	45.94
5.039	3.379	34.486	23.00	91.560	41.14
5.590	4.313	36.321	23.39	92.363	39.02
6.266	5.513	38.224	23.25	93.400	37.52
7.068	6.909	40.119	23.73	94.834	36.88
7.930	8.424	41.976	23.90	96.641	35.53
8.805	9.571	43.905	24.08	98.638	34.26
9.663	10.681	45.933	24.26	100.633	33.39
10.532	11.857	48.005	24.70	102.631	33.40
11.491	13.124	50.037	24.96	104.630	34.35
12.584	14.460	51.984	25.35	106.627	35.86
13.727	15.173	53.942	25.63	108.628	38.51
		55.916	26.06	110.632	40.36
2.645	0.615	57.899	26.43		
2.930	0.559	59.888	26.68		
3.228	1.124	61.991	27.38		
3.530	1.259	64.121	28.12		
3.881	1.790	66.192	29.10		
4.315	2.446	68.226	30.16		
4.861	3.276	70.265	31.44		

Table II-2 Molar heat capacity of Kr on graphite for n_s = 1.60 mmol.

T / K	C_m / $JK^{-1}mol^{-1}$	T / K	C_m / $JK^{-1}mol^{-1}$	T / K	C_m / $JK^{-1}mol^{-1}$
15.035	16.59	87.832	99.35	4.380	2.535
16.117	16.99	88.425	97.69	4.929	3.488
17.362	17.69	89.053	94.34	5.527	4.408
18.514	18.50	89.641	93.82	6.201	5.481
19.657	19.44	90.296	91.47	6.991	6.852
20.826	20.17	91.165	86.79	7.856	8.275
22.004	20.63	92.200	83.49	8.697	9.434
23.199	20.86	93.423	77.41	9.537	10.476
24.400	20.94	94.720	74.47	10.405	11.638
25.609	21.27	96.008	65.77	11.341	12.932
26.843	21.21	97.295	44.86	12.371	14.143
28.188	21.58	98.583	40.62	13.492	15.077
29.573	22.03	100.031	38.39	14.664	16.035
30.982	22.23	101.736	37.57		
32.456	22.10	103.641	39.29	2.787	0.691
34.050	22.38	105.636	40.64	3.128	0.944
35.820	22.91	107.639	43.90	3.525	1.472
37.580	22.59	109.646	46.55	3.956	2.001
39.440	23.01	111.637	49.24	4.464	2.704
41.419	23.01	113.630	50.79	5.036	3.615
43.394	23.62	115.624	53.85	5.652	4.611
45.408	23.72	117.617	59.32	6.343	5.708
47.368	23.60	119.610	61.81	7.141	7.077
49.349	24.23	121.604	67.50	8.006	8.579
51.394	24.68			8.856	9.677
53.441	24.57	3.083	0.931	9.703	10.671
55.508	24.53	3.426	1.275	10.589	11.764
57.573	25.05	3.801	1.846	11.510	12.974
59.615	25.91	4.233	2.481	12.494	14.108
61.642	26.09	4.733	3.141	13.592	15.417
63.658	27.01	5.285	3.963		
65.657	27.44	5.890	5.038	14.585	16.51
67.656	28.18	6.580	6.188	15.499	16.49
69.660	28.71	7.388	7.510	16.625	16.80
71.667	29.91	8.243	8.899	17.832	17.96
73.694	31.40	9.084	9.961	19.045	19.00
75.736	33.29	9.938	11.210	20.269	19.94
77.767	35.02	10.863	12.400	21.462	20.23
79.808	38.63	11.862	13.552	22.640	20.68
81.853	43.77	12.943	14.460	23.819	20.79
83.602	53.53	14.096	15.310	25.033	20.78
84.835	71.77			26.258	21.14
85.611	89.52	2.761	0.757	27.518	21.27
86.147	99.73	3.064	0.978	28.847	21.76
86.700	103.81	3.425	1.367	30.240	21.86
87.261	103.83	3.866	1.768	31.705	22.19

Table II-2 (continued).

T / K	C_m / $JK^{-1}mol^{-1}$	T / K	C_m / $JK^{-1}mol^{-1}$
33.226	22.02	102.710	38.35
34.826	22.61	104.689	39.87
36.473	22.80	106.667	42.06
38.261	22.55	108.648	45.63
40.196	23.21	110.632	47.48
42.281	23.29	112.613	50.04
44.388	23.50	114.594	52.94
46.367	23.43	116.576	55.71
48.337	23.75	118.557	59.25
50.464	24.13		
52.591	24.46		
54.542	24.82		
56.526	25.02		
58.540	25.55		
60.559	26.03		
62.605	26.16		
64.620	26.89		
66.611	27.81		
68.636	28.34		
70.668	29.52		
72.716	30.20		
74.718	32.05		
76.731	33.51		
78.791	36.08		
80.801	40.32		
82.275	44.79		
83.220	49.61		
84.054	57.89		
84.616	66.77		
85.002	74.47		
85.412	84.23		
85.870	95.51		
86.407	101.72		
86.913	101.08		
87.408	102.29		
88.029	97.70		
88.973	95.57		
90.358	90.14		
92.029	84.32		
93.799	76.46		
95.238	71.29		
96.146	63.10		
96.900	45.94		
97.964	40.01		
99.286	38.31		
100.832	37.63		

Table II-3 Molar heat capacity of Kr on graphite for n_a = 2.00 mmol.

T / K	C_m / $JK^{-1}mol^{-1}$	T / K	C_m / $JK^{-1}mol^{-1}$	T / K	C_m / $JK^{-1}mol^{-1}$
15.010	15.43	89.610	32.08	13.496	13.950
16.056	15.87	91.604	33.13	14.648	14.638
17.183	16.62	93.586	34.45		
18.327	17.33	95.568	35.76	3.823	1.322
19.506	18.22	97.454	37.39	4.090	1.797
20.745	19.15	99.223	39.82	4.411	2.397
21.965	19.58	100.823	42.91	4.816	2.735
23.191	19.84	102.426	46.99	5.355	3.510
24.389	19.91	103.837	52.18	5.987	4.390
25.605	20.33	104.927	57.97	6.708	5.487
26.912	20.45	106.045	65.31	7.514	6.708
28.209	20.77	106.954	70.87	8.350	7.937
29.465	21.07	107.652	76.90	9.186	8.889
30.804	21.47	108.338	83.94	10.041	10.168
32.248	21.39	109.000	92.96	10.951	11.088
33.750	21.73	109.632	97.88	11.986	12.515
35.239	22.20	110.217	105.69	12.995	13.662
36.696	22.44	110.792	112.63	14.092	14.649
38.377	22.64	111.387	122.75		
40.300	23.12	111.985	130.87	14.388	15.13
42.311	23.44	112.582	143.12	15.419	15.41
44.350	24.04	113.178	150.14	16.555	15.95
46.304	25.25	113.774	153.83	17.718	16.89
48.247	28.33	114.373	130.37	18.963	17.99
50.193	27.80	114.976	90.55	20.235	18.85
52.059	25.66	115.575	81.97	21.417	19.28
53.822	25.10	116.173	82.31	22.617	19.76
55.525	24.84	116.770	84.16	23.811	19.75
57.430	24.28	117.369	84.76	25.009	20.20
59.458	24.49	118.564	87.03	26.169	20.20
61.415	24.66	119.462	88.58	27.411	20.38
63.451	25.11	122.587	92.65	28.785	20.97
65.555	25.34			30.203	21.23
67.617	25.33	3.916	1.594	31.612	21.44
69.606	25.57	4.231	2.015	33.040	21.55
71.560	26.12	4.606	2.413	34.508	21.93
73.519	26.61	5.068	2.983	36.038	22.32
75.512	27.27	5.632	3.824	37.625	22.41
77.513	29.12	6.311	4.801	39.111	22.68
79.525	32.62	7.111	6.055	40.038	22.78
81.309	33.01	7.968	7.353	40.869	22.91
82.730	30.28	8.808	8.475	41.877	23.14
83.984	30.05	9.650	9.534	42.703	23.32
85.248	29.95	10.526	10.660	43.572	23.33
86.598	30.53	11.431	11.827	44.438	23.89
87.941	31.34	12.408	12.938	45.309	24.33

Table II-3 (continued).

T / K	C_m / $JK^{-1}mol^{-1}$	T / K	C_m / $JK^{-1}mol^{-1}$
46.131	24.69	110.670	111.85
46.902	25.27	111.219	119.57
47.675	26.67	111.718	127.09
48.450	28.37	112.215	134.25
49.226	28.72	112.700	142.72
49.980	27.82	113.177	149.09
50.711	26.15	113.649	153.18
51.442	25.87	114.097	145.11
52.739	25.31	114.527	110.62
54.696	24.85	114.957	90.36
56.686	24.61	115.387	85.90
58.551	24.91	116.206	85.42
60.487	24.43	117.833	86.15
62.506	24.83	119.843	89.24
64.567	25.21	121.817	91.82
66.630	25.60		
68.609	25.67		
70.550	25.75		
72.009	25.95		
72.979	26.38		
73.888	26.59		
74.791	26.94		
75.695	27.30		
76.595	28.31		
77.494	29.02		
78.390	30.00		
79.282	32.01		
80.172	34.93		
81.061	33.74		
81.953	30.98		
83.188	30.08		
84.966	29.84		
86.934	31.00		
88.896	31.69		
90.871	33.13		
92.844	33.88		
94.814	35.46		
96.798	37.05		
98.783	39.88		
100.769	43.86		
102.745	49.60		
104.724	58.55		
106.360	68.28		
107.656	79.56		
108.964	91.81		
109.995	103.32		

Table II-4 Molar heat capacity of Kr on graphite for n_a = 2.20 mmol.

T / K	C_m / $JK^{-1}mol^{-1}$	T / K	C_m / $JK^{-1}mol^{-1}$	T / K	C_m / $JK^{-1}mol^{-1}$
14.325	14.48	72.356	27.84	9.036	7.423
15.370	14.74	73.964	28.53	9.918	8.522
16.536	15.42	75.524	29.26	10.899	9.936
17.716	16.31	77.079	29.40	12.007	11.410
18.895	17.53	78.620	31.58	13.122	12.639
20.100	18.48	87.629	40.43	14.293	13.975
21.291	19.13	88.668	43.18		
22.482	19.70	89.706	45.90	2.617	0.384
23.648	19.93	90.745	48.08	2.856	0.430
24.821	20.02	91.784	51.17	3.099	0.721
14.452	14.47	92.846	54.42	3.353	0.857
15.547	14.98	93.999	58.41	3.664	1.058
16.716	15.37	95.102	62.80	4.060	1.265
17.923	16.62	96.090	67.85	4.578	1.783
19.149	17.77	97.064	71.94	5.202	2.399
20.372	18.77	97.991	77.82	5.910	3.130
21.603	19.29	98.882	83.65	6.671	4.098
22.850	19.86	99.765	88.21	7.556	5.430
24.120	20.12	100.630	87.78	8.518	6.729
25.349	20.40	101.474	81.71	9.423	7.969
26.586	20.58	102.320	75.71	10.408	9.318
27.863	20.91	103.168	73.59	11.469	10.637
29.104	21.38	104.014	70.81	12.558	12.122
30.482	21.79	104.860	67.50	13.712	13.143
31.972	22.01	105.705	64.41	14.866	14.229
33.425	22.23	106.548	61.47		
34.996	22.79	107.393	60.45	2.819	0.476
36.694	22.87	108.264	60.95	3.070	0.593
38.361	23.04	109.288	61.62	3.329	0.756
40.082	23.55	110.436	62.82	3.619	0.916
41.866	23.95	111.578	63.55	3.999	1.209
43.654	24.18	112.704	66.22	4.588	1.801
45.451	24.29	113.815	70.52	5.304	2.532
47.250	24.24	114.925	75.23	6.095	3.614
49.082	24.40	116.037	82.83	6.999	4.638
50.943	24.72			7.904	5.903
52.860	24.68	2.925	0.527	8.778	7.030
54.792	25.14	3.191	0.695	9.709	8.373
56.702	24.84	3.497	0.886	10.786	9.833
58.683	25.78	3.871	1.184	11.969	11.450
60.705	25.03	4.313	1.561	13.179	12.660
62.726	25.56	4.845	1.993	14.378	13.760
64.769	25.81	5.494	2.606		
66.744	26.65	6.253	3.526		
68.702	26.82	7.135	4.814		
70.617	27.21	8.102	6.193		

Table II-4 (continued).

T / K	C_m / $JK^{-1}mol^{-1}$	T / K	C_m / $JK^{-1}mol^{-1}$
23.157	20.03	95.377	63.08
24.237	20.04	96.354	67.09
25.395	20.38	97.328	72.92
26.348	20.47	98.316	79.91
27.339	20.56	99.307	84.75
28.552	21.11	100.301	88.20
29.779	21.53	101.291	82.42
30.957	21.81	102.284	74.79
32.340	21.87	103.277	73.23
33.917	22.29	104.370	69.66
35.635	22.93	105.564	64.10
37.533	22.94	107.211	60.51
39.341	23.49		
41.069	23.61		
42.833	24.19		
44.599	24.28		
46.330	24.42		
48.022	24.40		
49.876	24.42		
51.883	24.72		
53.809	24.80		
55.727	24.61		
57.725	24.81		
59.681	25.55		
61.590	24.95		
63.507	25.83		
65.523	25.76		
67.612	26.43		
69.614	26.44		
71.536	27.26		
73.446	28.10		
75.335	29.22		
77.215	29.86		
78.758	30.55		
79.935	31.91		
81.112	32.45		
82.291	33.60		
83.451	34.53		
84.615	36.45		
85.788	37.47		
86.959	39.45		
88.127	41.49		
89.298	44.48		
90.464	46.50		
93.966	57.94		
94.576	59.97		

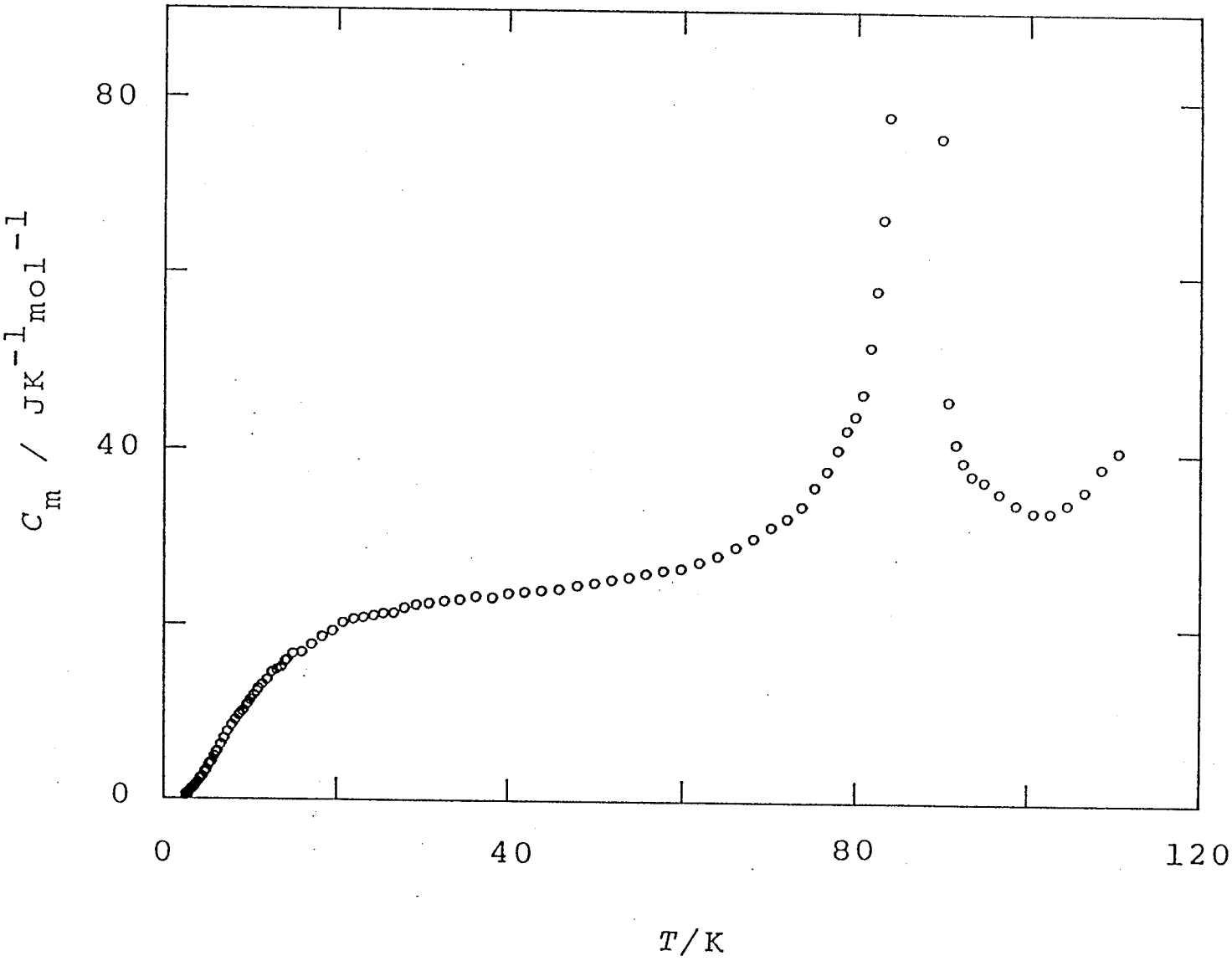

Fig. II-3(a) Molar heat capacity of Kr on graphite for n_a = 1.42 mmol.

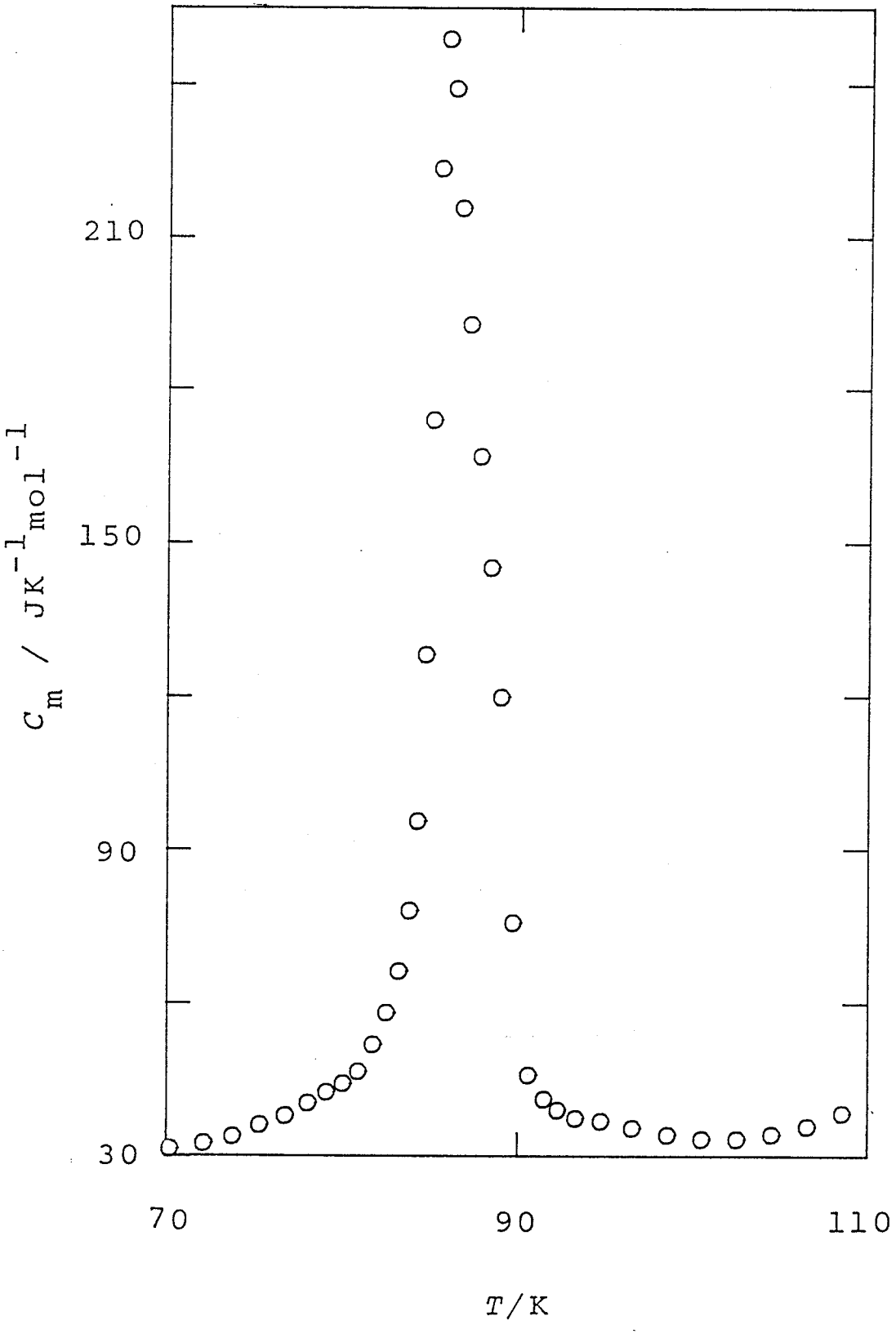

Fig. II-3(b) Molar heat capacity of Kr on graphite for n_s = 1.42 mmol (melting region).

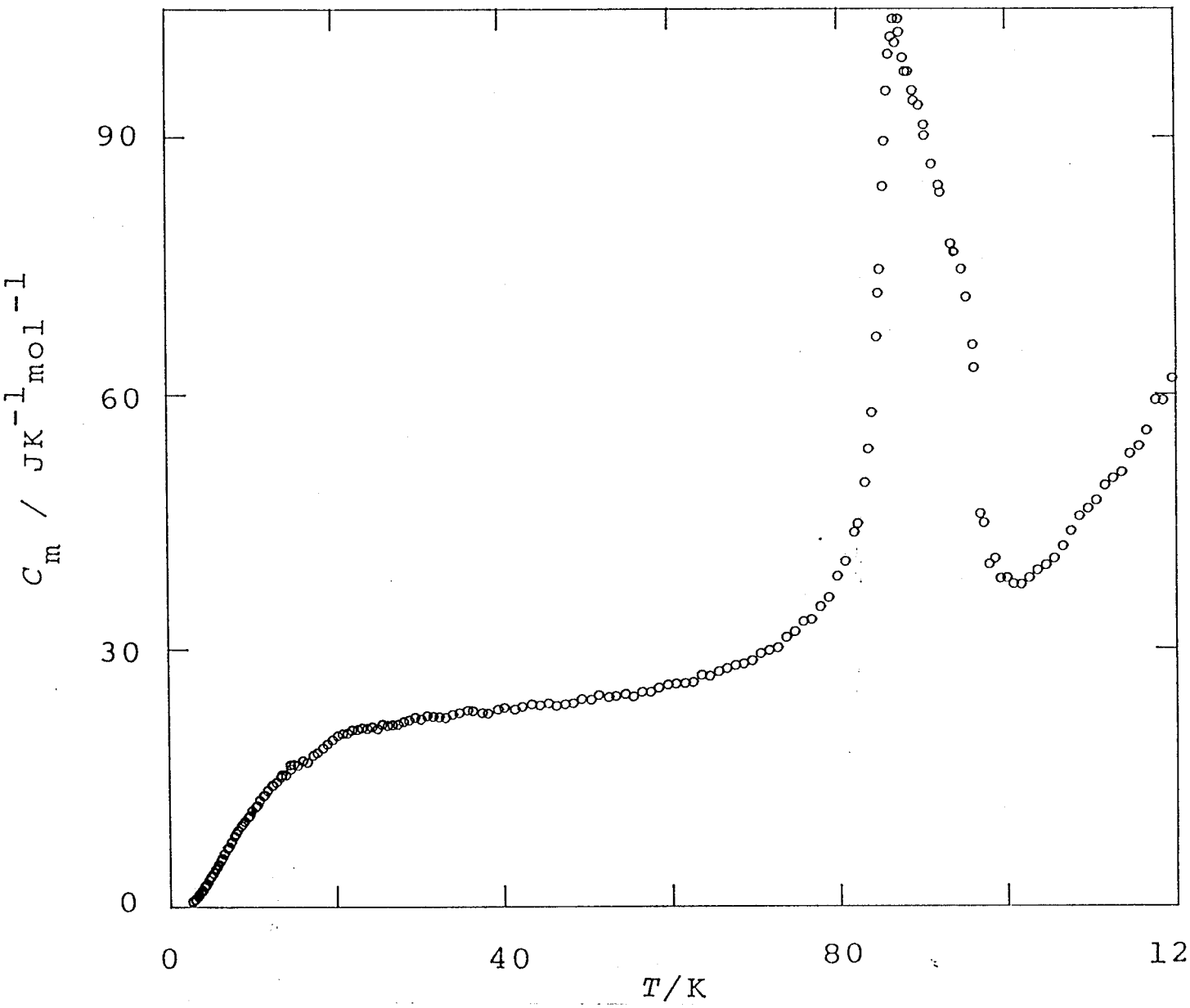

Fig. II-4 Molar heat capacity of Kr on graphite for n_a = 1.60 mmol.

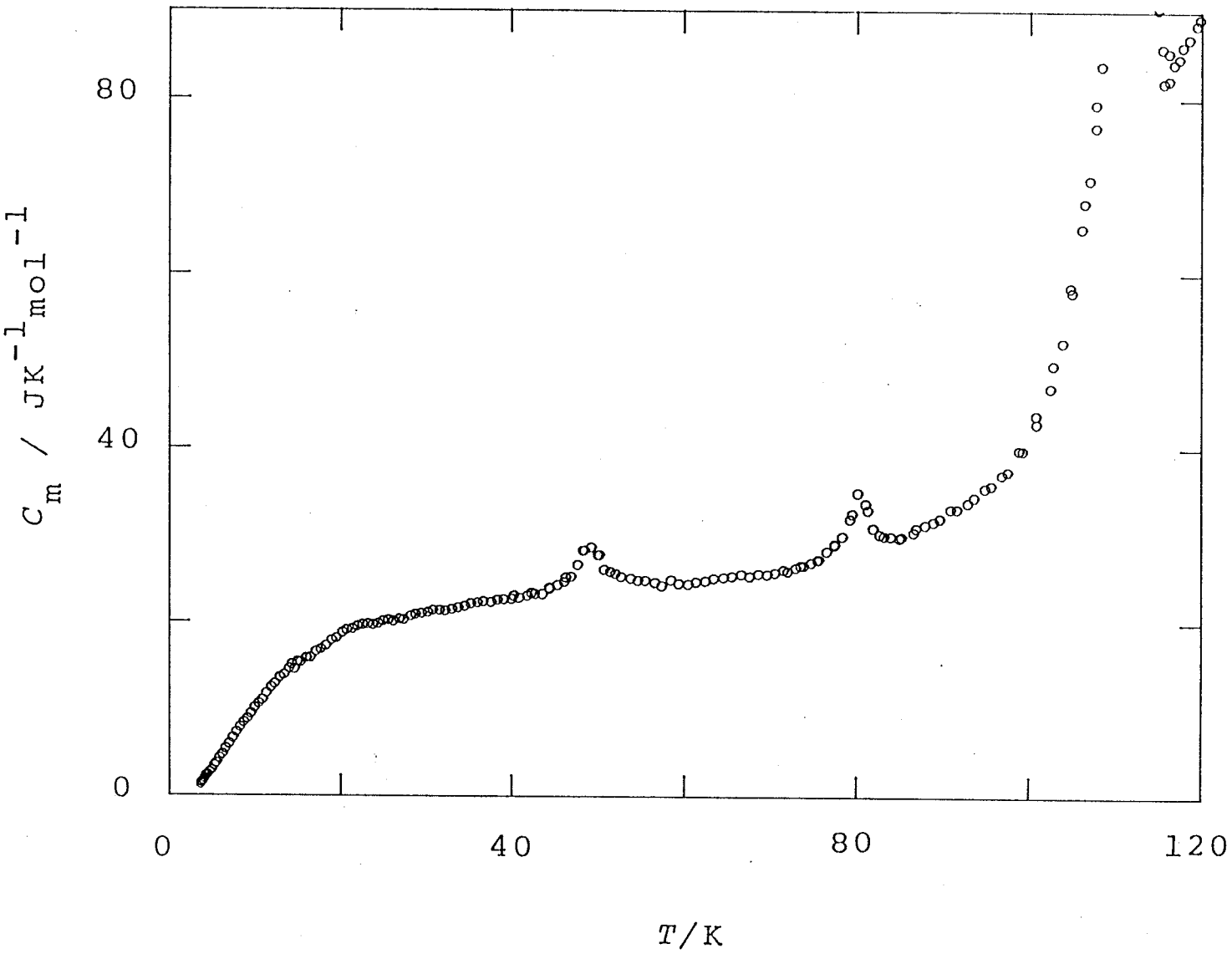

Fig. II-5(a) Molar heat capacity of Kr on graphite for n_a = 2.00 mmol.

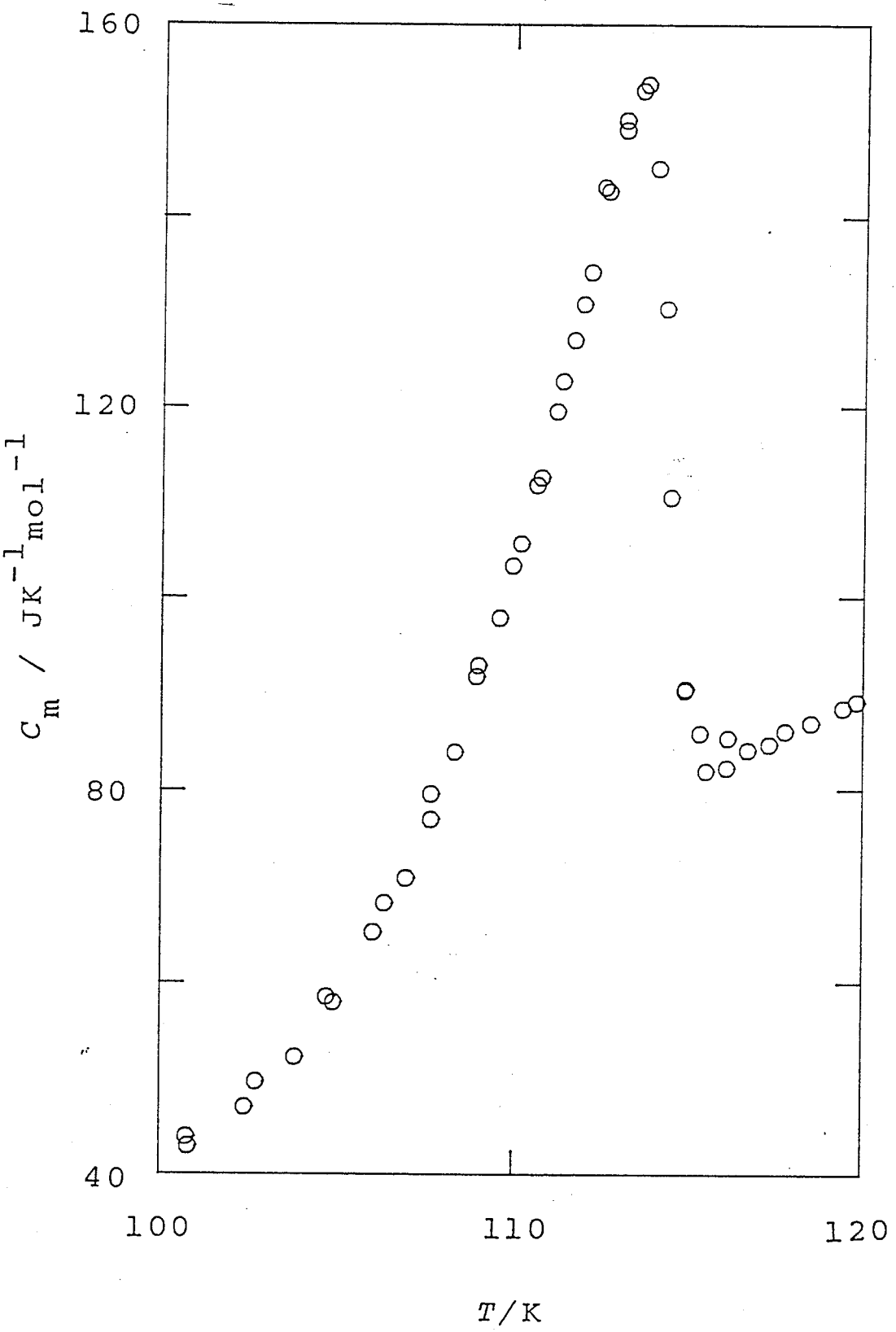

Fig. II-5(b) Molar heat capacity of Kr on graphite for n_s = 2.00 mmol (melting region).

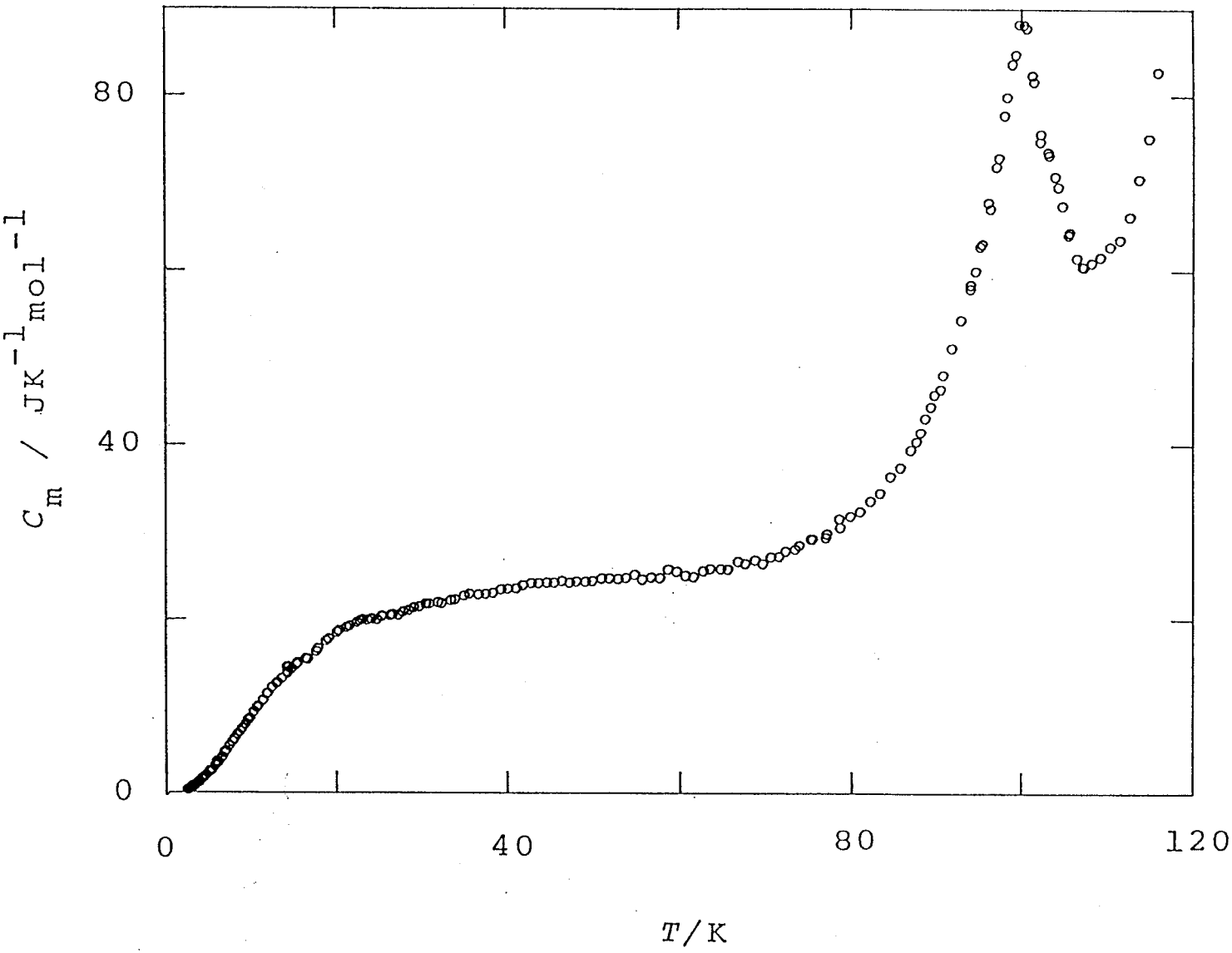

Fig. II-6 Molar heat capacity of Kr on graphite for n_a = 2.20 mmol.

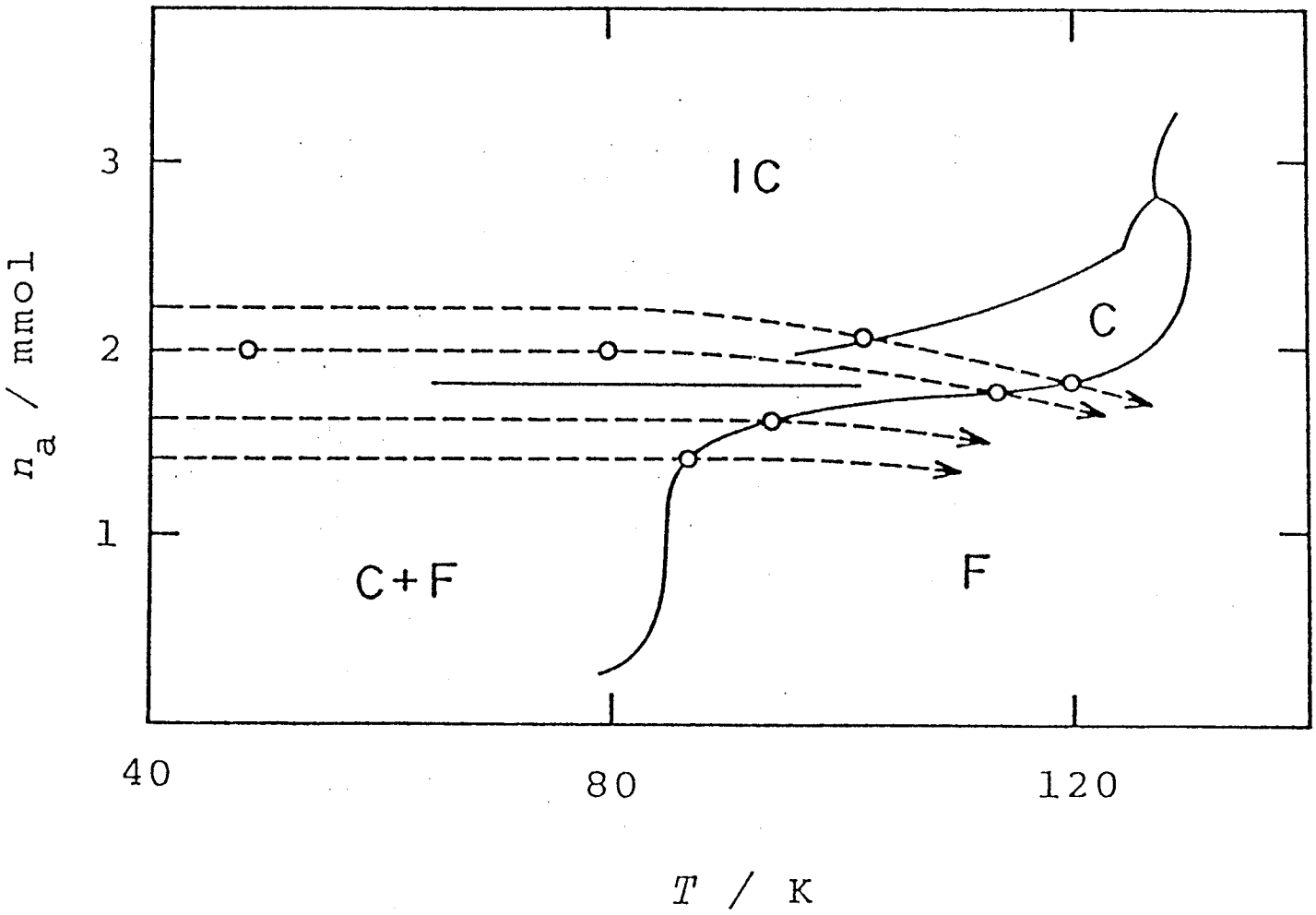

Fig. II-7 The phase diagram of Kr on graphite: C, commensurate solid phase; IC, incommensurate solid phase; F, fluid phase; -----, our measurement path; o, the peak in heat capacity observed by the present work. The coverage is adjusted by the phase boundary at the commensurate coverages determined by Butler *et al.* (ref. II-5) (——).

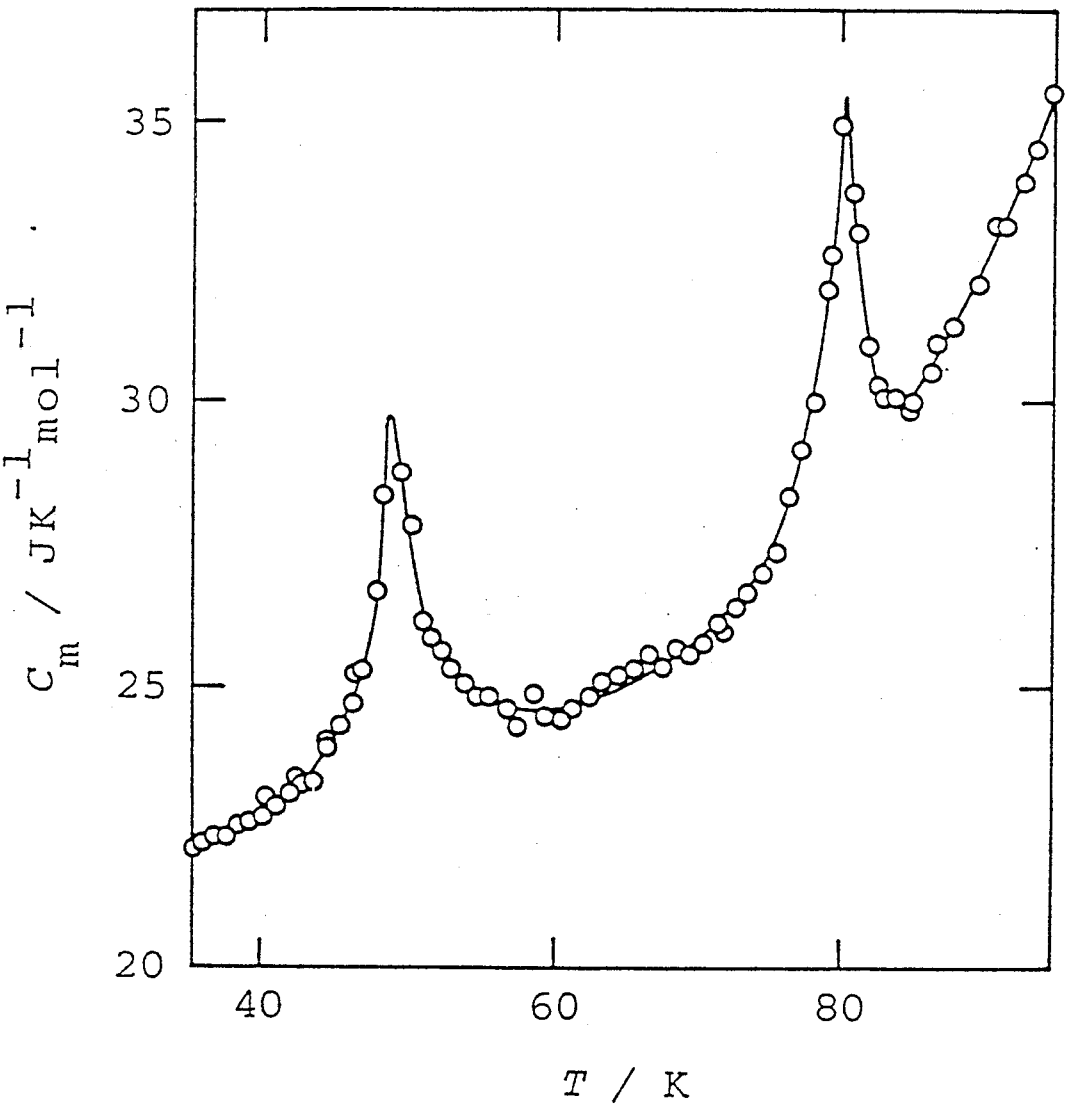

Fig. II-8 Molar heat capacity of Kr on graphite for n_a = 2.00 mmol (ref. 12).

its translational correlation. A synchrotron x-ray diffraction study (refs. 6 and 7) actually found the re-entrant fluid phase between the commensurate and incommensurate phases in Kr/graphite. The former phase sequence, therefore, is not an unusual case.

II-3-3 Lattice Property of Monolayer

With respect to the vibrational motions perpendicular to the surface, we can safely assume that such modes would be localized. This is because the admolecule-substrate interactions are much stronger than the admolecule-admolecule interactions even in the case of physisorbed systems. The admolecules have no periodicity in this direction, which allows us to deal with such motions as an Einstein mode. In order to estimate the corresponding characteristic temperature, we first obtained two-dimensional characteristic Debye temperatures from the experimental heat capacities by neglecting the Einstein mode. In Fig. II-9 the Debye temperatures Θ_D are plotted as a function of temperature for the coverages n_s = 1.60 mmol (commensurate phase) and 2.20 mmol (incommensurate phase), respectively. Here we assume $2N$ degrees of freedom for the krypton monolayer. For both coverages, the Debye temperatures fall off rapidly at high temperatures, indicating that the excitation of the vibrational motions perpendicular to the surface becomes significant. Assuming that the two-dimensional lattice vibrations should be fully excited in this temperature region, the characteristic Einstein temperature Θ_E was determined in such a way that the Debye temperature remains constant with temperature. We thus derived 48 K for the value of Θ_E for both coverages. This fact means that the surface corrugation does not affect significantly the vibrational motions perpendicular to the surface.

We now modify the two-dimensional Debye model to accommodate it to the fact that there is another cut-off frequency, ν_c, at the low-frequency end of the vibrational spectrum for the commensurate solid. To describe this, we assume a model for the phonon density of states (ref. 12), which has two cut-off

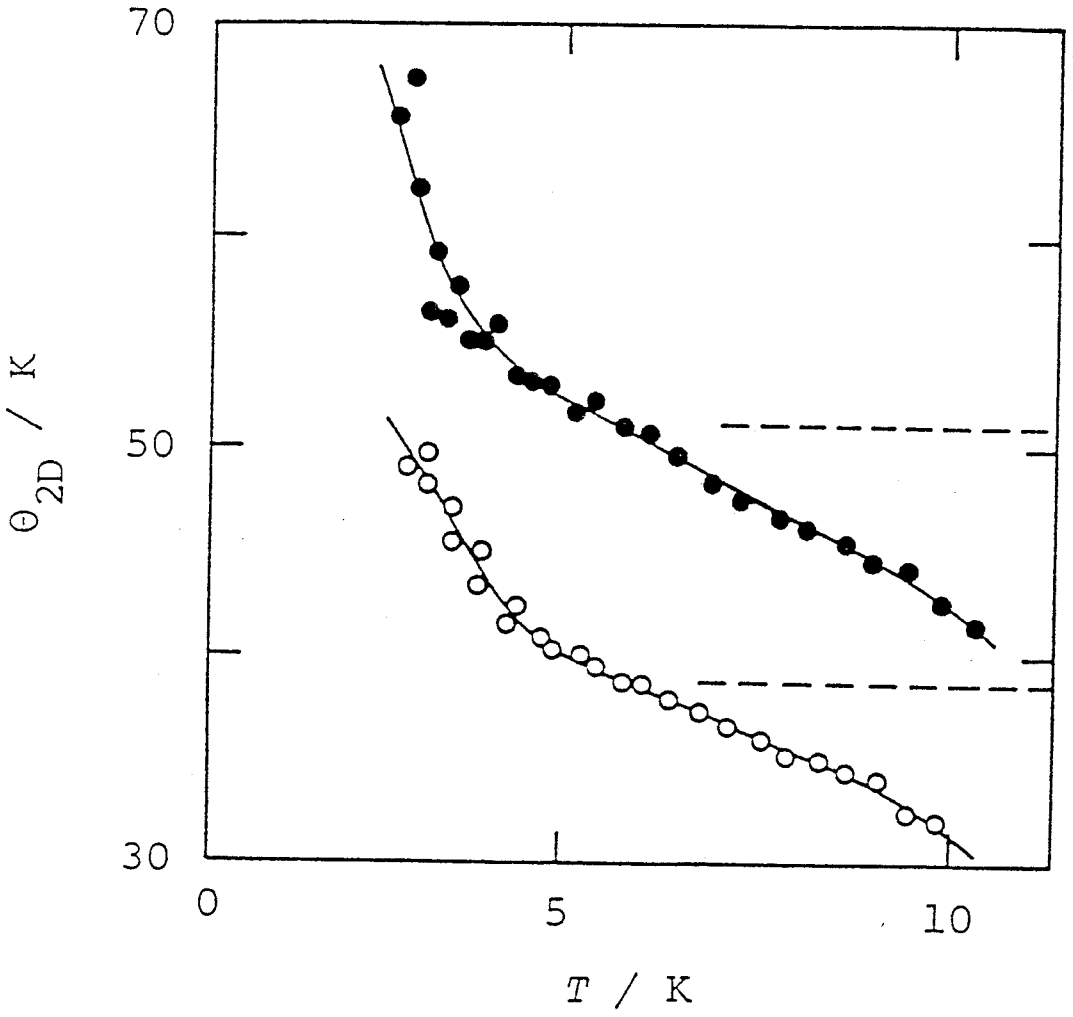

Fig. II-9 Two-dimensional Debye temperatures for n_3 = 1.60 mmol (open circles) and for n_3 = 2.20 mmol (solid circles). -----, supposed behavior for the contribution from lattice vibrations (ref. 12).

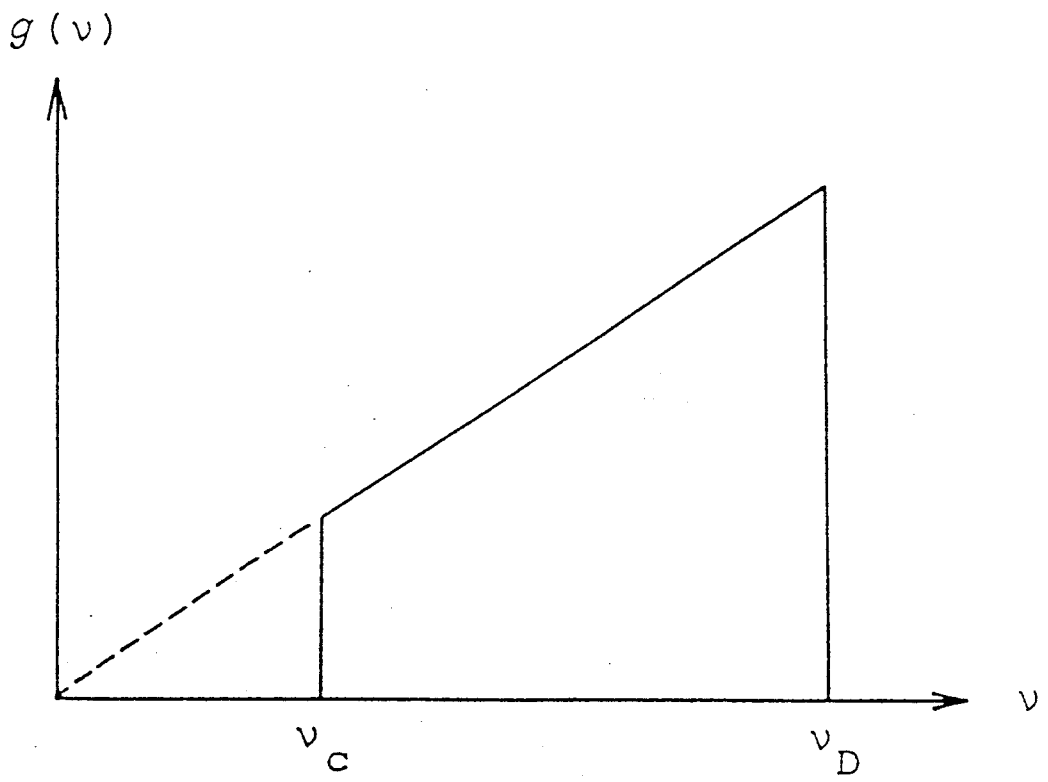

Fig. II-10 Debye-like model for the phonon density of states.

Table II-5 The characteristic temperatures obtained for the Kr monolayers on graphite.

n_a /mmol	Θ_D /K	Θ_c /K	Θ_E /K
1.42	35 ± 1	11 ± 1	52 ± 4
1.60	35 ± 1	11 ± 1	53 ± 4
2.00	40 ± 1	9 ± 2	57 ± 4
2.20	49 ± 1	7 ± 1	51 ± 3

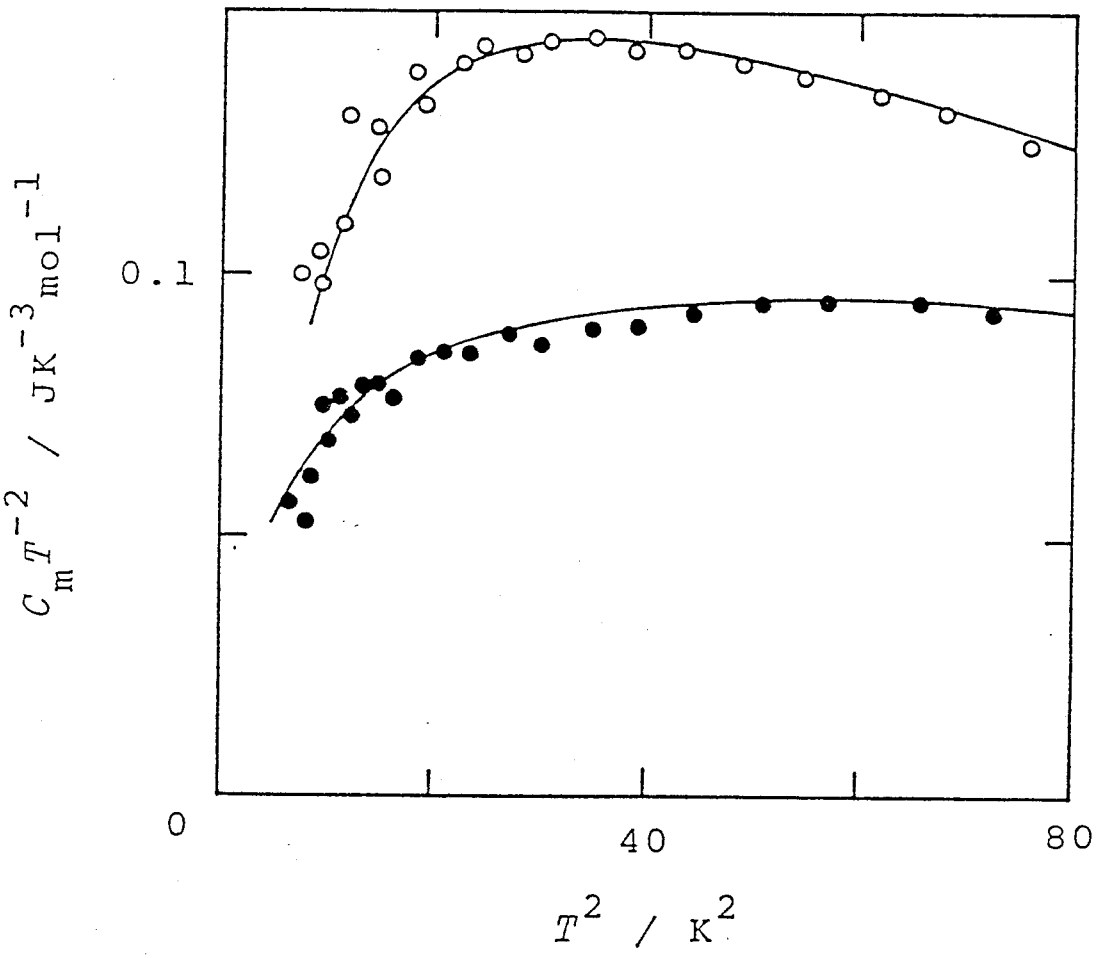

Fig. II-11 A plot of $C_m T^{-2}$ against T^2 for n_s = 1.60 mmol (open circles) and for n_s = 2.20 mmol (solid circles) at low temperatures. Solid lines are the fitted curves for both phases with the model. Contribution from the vibration perpendicular to the surface is subtracted from the observed heat capacities.

frequencies ν_c and ν_D as shown in Fig. II-10. The fitting of the heat capacities obtained for n_s = 1.60 mmol (Fig. II-11), for instance, determined the parameters Θ_c and Θ_D to be 10 K and 36 K, respectively. Here, Θ is equal to $h\nu/k_B$. The vibrational states of the krypton monolayer can thus be described phenomenologically with one Debye mode possessing two cut-off frequencies and one Einstein mode. All the fitting parameters including those for the incommensurate coverages are tabulated in table II-5. One of the cut-off temperature for the commensurate solid, Θ_c = 11 ± 1 K for both n_s = 1.60 and 1.42 mmol, is very close to that measured directly by inelastic neutron scattering (8.7 K, ref. 14). The reasonable agreement indicates that the heat capacity measurement is useful to estimate the zone-center gap in addition to the determination of the other cut-off frequency.

II-3-4 Amplitude of Surface Corrugation

In the case of monatomic-molecule monolayers, such as krypton on graphite, the amplitude of surface corrugation V_0 can be estimated by eq. I-4, or

$$V_0 = - m(a_0 \nu_c)^2/12 = - m(a_0 k_B \Theta_c/h)^2/12. \qquad \text{(II-1)}$$

By inserting Θ_c value to this equation, we obtain V_0/k_B = - 8.0 ± 1.2 K for the commensurate coverages. The magnitude is larger than that calculated (-4.6 K) by the use of the isotropic atom-atom potential and the Steele's parameters (ref. 15). Vidali and Cole pointed out (ref. 16) that the dielectric anisotropy of graphite (ref. 17) may explain this discrepancy.

According to Eq. I-3, the difference in energy between the hexagon center site (C site) and the saddle point site (bridge site: B site) is -8 × (-8.0 K) (corresponding to 0.53 kJ mol^{-1}). The large value means that the graphite surface is not flat at all on an atomic scale. The static calculation (ref. 18) demonstrates that even more strongly modulated potential ($V_0/k_B \leq$ - 11 K) would be necessary to stabilize the $\sqrt{3} \times \sqrt{3}$ commensurate structure. On the other hand, a molecular dynamics

simulation (ref. 19) showed that the commensurate solid was stable at finite temperatures even though the Steele's parameters were used. Recently, Shrimpton and Steele calculated the dynamic structure factor from molecular dynamics (ref. 20) using the modified Steele's potential

$$V(\vec{r},z) = V(z) + s \sum V_g(z)\exp(i\vec{g}\cdot\vec{r}), \qquad \text{(II-2)}$$

where they introduced a new parameter s into Eq. I-3. The zone-center gap calculated with s = 1.5 agreed reasonably with that obtained by neutron scattering.

II-3-5 Size Effect on Phonons in Incommensurate Solid

The apparent cut-off temperature Θ_c obtained for the incommensurate solid (n_s = 2.20 mmol) is also nonzero value: 7 ± 1 K. One of the reasons we might consider is that the effect of surface corrugation cannot be completely smeared out (ref. 12). Here we discuss another possible reason, which is the quantum size effect (ref. 21). As is discussed in very small particle system, the maximum wave-length λ_m we meet should be the twice of the size of the particle. Then the smallest wave vector q_s and the apparent cut-off temperature Θ_s are calculated by

$$q_s = 2\pi/\lambda_m = \pi/d, \qquad \text{(II-3)}$$

$$\Theta_s = hq_s v/2\pi k_B = hv/2dk_B, \qquad \text{(II-4)}$$

where d is the size of the particle and v is the sound velocity. The coherent length of the substrate graphite we used is of the order of 10 nm (ref. 22), and the sound velocity can be assumed to be somewhere around 1-2 km s^{-1}. With these values, Θ_s is estimated to be 2 - 5 K, which is similar to the cut-off temperature obtained for n_s = 2.20 mmol.

According to a LEED experiment (ref. 3), the value Θ_c for n_s = 2.00 mmol is situated between those for the commensurate and incommensurate phases. However, both the Θ_c (9 K) and the Θ_0

(40 K) are between those for n_s = 2.20 and 1.60 mmol, indicating that the lattice properties change gradually with coverage in the incommensurate phase. The fact suggests that the phase at the coverage n_s = 2.00 mmol seems to be weekly incommensurate. Therefore, the phase sequence at the coverage is probably [incommensurate → re-entrant fluid → commensurate] with increasing temperature.

References to Chapter II

1. A. Thomy and X. Duval, *J. Chim. Phys.* 67, 1101 (1970).
2. M.D. Chinn and S.C. Fain, Jr., *Phys. Rev. Lett.* 39, 146 (1977).
3. P.M. Horn, R.J. Birgeneau, P.A. Heiney and E.M. Hammonds, *Phys. Rev. Lett.* 41, 961 (1978).
4. D.M. Butler, J.A. Litzinger, G.A. Sttewart and R.B. Griffiths, *Phys. Rev. Lett.* 42, 1289 (1979).
5. D.M. Butler, J.A. Litzinger and G.A. Sttewart, *Phys. Rev. Lett.* 44, 466 (1980).
6. D.E.Moncton, P.W. Stephens, R.J. Birgeneau, P.M. Horn and G.S. Brown, *Phys. Rev. Lett.* 46, 1533 (1981).
7. E.D. Specht, M.Sutton, R.J. Birgeneau, D.E.Moncton and P.M. Horn, *Phys. Rev.* B30, 1589 (1984).
8. C. Bouldin and E.A. Stern, *Phys. Rev.* B25, 3462 (1982).
9. K. Saito, T. Atake and H. Chihara, *J. Chem. Thermodyn.* 19, 633 (1987).
10. A. Inaba, T. Shirakami and H. Chihara, *J. Chem. Thermodyn.* 23, 461 (1991).
11. A. Inaba, Y. Koga and J.A. Morrison, *J. Chem. Soc., Faraday Trans. II* 82, 1635 (1986).
12. T. Shirakami, A. Inaba and H. Chihara, *Thermochim. Acta* 163, 233 (1990).
13. M.I. Bagatoskii, V.A. Kucheryavy, V.G. Manzhelii and V.A. Popov, *Phys. Stat. Sol.* 26, 453 (1968).
14. H.J. Lauter, V.L.P. Frank, H. Taub and P. Leiderer, *Physica* B 165&166, 611 (1990).
15. W.A. Steele, *Surf. Sci.*, 36, 317 (1973).

16. G. Vidali and M.W. Cole, *Phys. Rev.* B29, 6736 (1984).
17. W.E. Carlos and M.W. Cole, *Surf. Sci.* 91, 339 (1980).
18. R.J. Gooding, B. Joos and D.L. Bergersen, *Phys. Rev.* B27, 7669 (1983).
19. F.F. Abraham, *Proccedings of the Inetrnational School of Physics "Enrico Fermi"*; 97, 130 (1985).
20. N.D. Shrimpton and W.A. Steele, *Phys. Rev.* B44, 3297 (1991).
21. V. Novotny and P.P.M. Meincke, *Phys. Rev.* B8, 9186 (1973).
22. H. Taub, K. Carneiro, J.K. Kjems, L. Passell and J.P. McTgue, *Phys. Rev.* B16, 4551 (1977).
23. S.N. Coppersmith, D.S. Fisher, B.I. Halperin, P.A. Lee and W.F. brinkman, *Phys. Rev.* B25, 349 (1982).

Chapter III Nitrogen on Graphite

III-1 Introduction

Among various physisorbed systems, the N_2 monolayer on graphite has been most widely studied. In contrast to the krypton monolayer, quadrupolar and anisotropic intermolecular interactions are both important in the N_2 monolayer. The solid overlayer is known to exhibit an orientational order-disorder phase transition. The surface corrugation of graphite plays again an important role in determining the structure of the monolayer, as in the case of krypton/graphite. Namely, N_2/graphite has a commensurate phase. The phase diagram therefore turns out to be rather complicated. The structure of the orientationally ordered phase has been investigated both theoretically (ref. 1) and experimentally (refs. 2-7). According to the diffraction experiments, there are three kinds of ordered solid phases depending upon the coverage as shown in Fig. III-1: the C-phase with a $\sqrt{3}\times\sqrt{3}$ commensurate in-plane herringbone structure in which the molecular axes are parallel to the surface (refs. 2-4); the UI-phase with a uniaxially compressed incommensurate herringbone structure (refs. 3 and 5); and the TI-phase with a fully compressed incommensurate structure in which the molecular axes are tilted out of the surface (refs. 3, 4, 6 and 7). The commensurate-incommensurate phase transition thus occurs by two steps. The C-phase is compressed along the direction perpendicular to the glide line A (corresponding to the glide plane in three-dimensional lattice, see Fig. III-1) to produce a partly-commensurate phase (UI-phase). It is then compressed further along the glide line to bring a completely incommensurate phase (TI-phase).

We first investigate the effect of surface corrugation on the vibrational properties of the N_2 monolayer on graphite. While an inelastic neutron scattering experiment (refs. 9 and 10) determined the zone-center gap for the C-phase, the low temperature heat capacity can also deduce the size of the gap as discussed in the previous chapter. The vibrational state of the

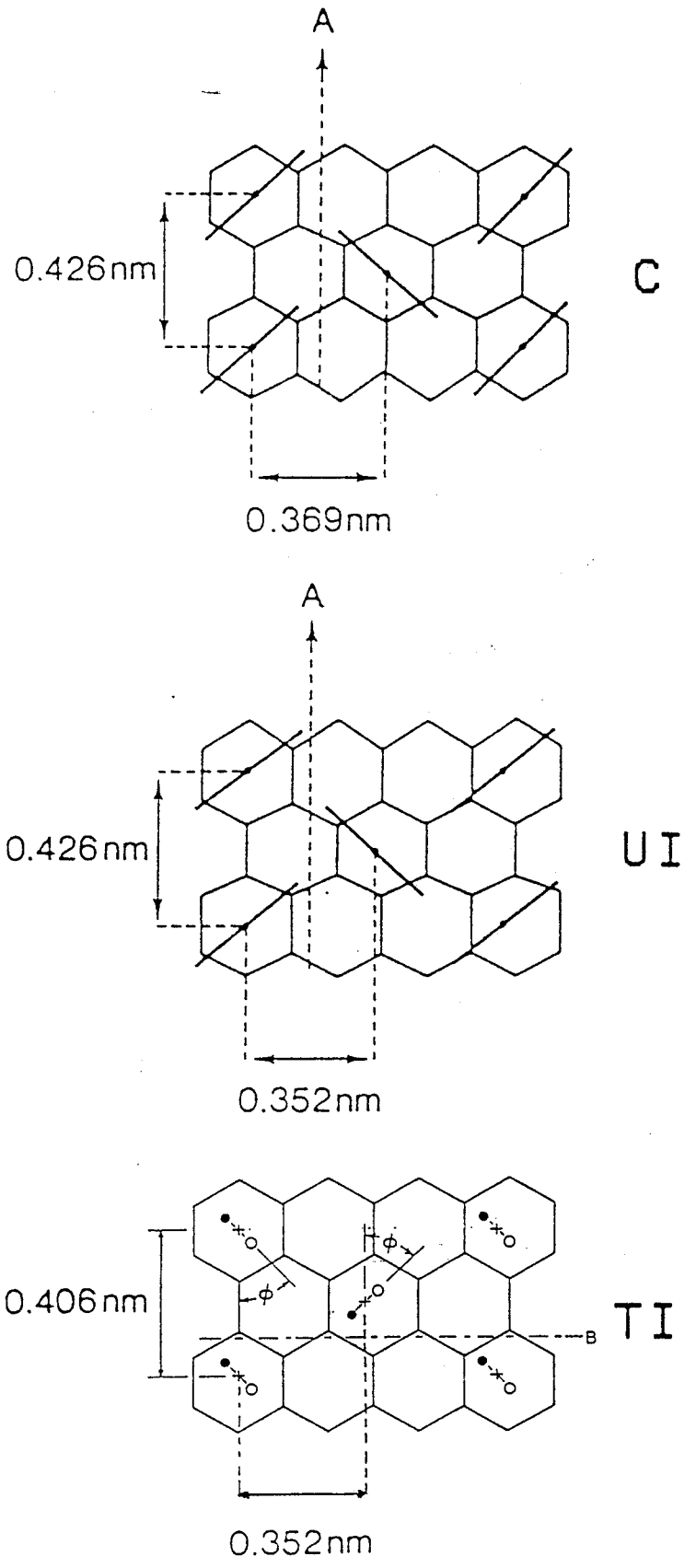

Fig. III-1 Schematic drawings of the structures of N_2 monolayers on graphite. C, commensurate phase; UI, uniaxially incommensurate phase; TI, triangular incommensurate phase (refs. 6 and 8).

UI-phase cannot be determined by the model function without correcting for the incommensurate structure. This problem is also interesting in order to understand the commensurability of the monolayer structure.

Another object here is the investigation of the orientational order-disorder phase transition. According to an a.c. calorimetric study (refs. 11-13), the transition accompanied a sharp anomaly in heat capacity for both the C- and UI-phases, whereas the anomaly for the TI-phase was much broader than that. We investigate the transition with an adiabatic calorimeter. A new phase transition was incidentally found for the C-phase.

III-2 Experimental Details

Two calorimeter assemblies were employed for the heat capacity measurement; an adiabatic calorimeter installed in a helium-4 cryostat and an isoperibol calorimeter installed in a helium-3 cryostat. The adiabatic calorimeter and the measuring system were the same as those described in Chap. II, except that a new digital multimeter (model 195A, H. Tinsley & Co., Ltd.) was used.

A sectional view of the helium-3 cryostat equipped with an adsorption pump is shown in Fig. III-2. It has a mechanical heat-switch to cool the calorimeter vessel by thermal conduction or to keep it in a quasi-adiabatic condition. The calorimeter vessel contained 4.75 g of Grafoil MAT and carried a calibrated germanium thermometer (Lake Shore Cryotronics, Inc.) and a manganin heater. The temperature scale used for this thermometer is based on the EPT-76. All the lead wires are of manganin in order to minimize the heat leak to and from the surroundings.

N_2 gas of special grade (99.9999 %), purchased from Takachiho Kagaku, was used without further purification. The actual amounts of the gas introduced were 0.972 and 1.43 mmol for the isoperibol calorimeter and 2.31 mmol for the adiabatic calorimeter. The coverages correspond to those for the C-, UI- and TI-phases, respectively.

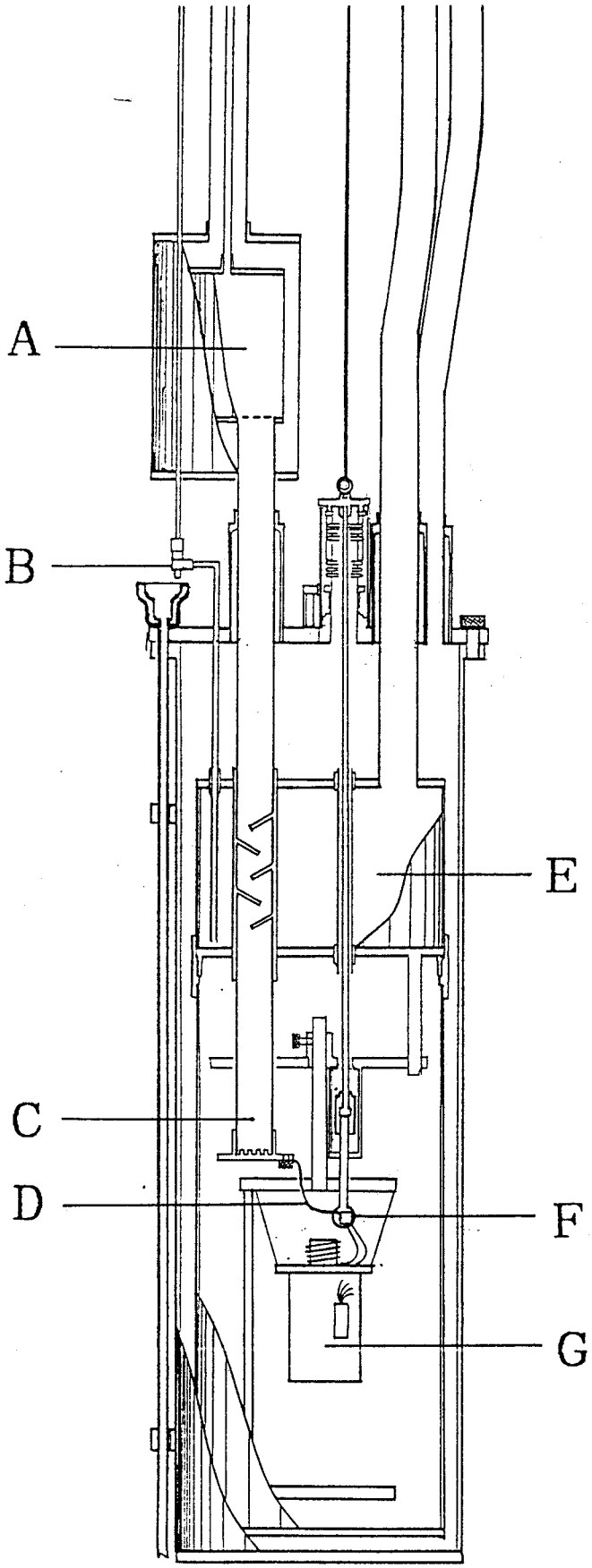

Fig. III-2 Sectional view of the helium-3 cryostat. A, adsorption pump; B, needle valve; C, helium-3 pot; D, copper braid; E, coolant container; F, mechanical heat switch; G, calorimeter vessel.

III-3 Results and Discussion

III-3-1 Heat Capacity

The molar heat capacities obtained for n_s = 0.972, 1.43 and 2.31 mmol are tabulated in Tables III-1, III-2 and III-3, respectively and are plotted in Figs. III-3, III-4 and III-5, respectively.

III-3-2 The Vibrational States

The plot of $C_m T^{-2}$ against T^2 at the lowest temperatures (Fig. III-6) clearly shows the existence of a cut-off in the phonon density of states for all the phases. The different behavior among the three samples, however, reflects the dissimilar structures or the size effect. Assuming a Debye model with two cut-off frequencies, ν_c and ν_D, similar analysis as described in Chapter II was applied. The characteristic temperatures obtained are summarized in Table III-4. The Θ_c for the C-phase (15 K) can be comparable in magnitude with that obtained from a neutron scattering study (19 K, ref. 9). A lattice dynamical calculation from the first principles (ref. 14), however, gave a rather small value (7 K). The deviation of the experimental heat capacity above 5 K from that obtained by the Debye model allowed us to estimate an Einstein temperature ($3N$ degrees of freedom), which may characterize the vibrational motions perpendicular to the surface (N degrees of freedom) and the librational motions ($2N$ degrees of freedom) together. The Θ_E seems to be independent of the coverage (Table III-4).

The modified Debye model, however, is insufficient to describe what happens in the UI-phase, because the physical meaning of the cut-off temperature is not clear in this case. Indeed, the in-plane translational motions of the molecules are considered in a lattice dynamics calculation only. The out-of-plane translational motions and the rotational motions are ignored because the Einstein modes cannot be significantly excited at sufficiently low temperatures For all the phases, it

Table III-1 Molar heat capacity of N_2 C-phase for n_a = 0.972 mmol.

T / K	C_m / $JK^{-1}mol^{-1}$	T / K	C_m / $JK^{-1}mol^{-1}$	T / K	C_m / $JK^{-1}mol^{-1}$
2.227	0.010	5.119	0.919	3.352	0.149
2.368	0.033	5.441	1.126	3.534	0.234
2.516	0.090	5.788	1.310	3.723	0.273
2.704	0.089	6.167	1.605	3.932	0.307
2.882	0.124	6.576	1.931	4.166	0.382
3.058	0.174	6.985	2.200	4.411	0.566
3.237	0.165			4.674	0.624
3.424	0.186	2.070	0.021	4.983	0.771
3.614	0.205	2.227	0.025	5.315	1.042
3.814	0.263	2.401	0.040	5.642	1.162
4.026	0.333	2.614	0.098	5.974	1.391
4.264	0.481	2.812	0.090	6.341	1.679
4.525	0.598	2.992	0.141	6.747	2.081
4.812	0.695	3.169	0.164	7.145	2.309

Table III-2 Molar heat capacity of N_2 UI-phase for n_a = 1.43 mmol.

T / K	C_m / $JK^{-1}mol^{-1}$	T / K	C_m / $JK^{-1}mol^{-1}$	T / K	C_m / $JK^{-1}mol^{-1}$
1.337	0.014	4.428	0.763	2.431	0.125
1.427	0.013	4.745	0.882	2.577	0.153
1.526	0.027	5.088	1.140	2.733	0.186
1.632	0.021	5.459	1.389	2.911	0.214
1.757	0.034	5.843	1.670	3.119	0.261
1.898	0.042	6.232	1.966	3.357	0.299
2.038	0.060	6.624	2.321	3.604	0.391
2.178	0.086	7.011	2.745	3.843	0.503
2.319	0.108			4.074	0.562
2.489	0.142	1.287	0.010	4.304	0.733
2.656	0.177	1.381	0.010	4.561	0.832
2.834	0.201	1.478	0.017	4.877	0.965
3.021	0.244	1.584	0.026	5.263	1.254
3.217	0.277	1.712	0.032	5.686	1.515
3.423	0.327	1.856	0.037	6.100	1.867
3.643	0.395	1.994	0.056	6.491	2.139
3.882	0.489	2.152	0.074	6.866	2.557
4.142	0.552	2.292	0.100	7.229	3.133

Table III-3 Molar heat capacity of N_2 TI-phase for n_s = 2.31 mmol.

T / K	C_m / $JK^{-1}mol^{-1}$	T / K	C_m / $JK^{-1}mol^{-1}$	T / K	C_m / $JK^{-1}mol^{-1}$
14.190	14.39	72.060	68.74	9.101	6.492
15.160	16.49	73.430	66.83	9.803	7.697
16.421	18.31	74.801	64.86	10.539	8.919
17.693	20.85	76.173	65.10	11.307	10.201
18.888	23.63	77.591	67.78	12.099	11.399
20.004	26.75	78.990	71.48	12.912	12.731
21.114	29.08	80.345	79.24	13.705	14.000
22.295	31.17	81.677	96.25	14.453	14.971
23.473	32.40	82.907	211.25		
24.656	32.74	84.039	308.70	2.118	0.242
25.848	33.36	85.171	109.14	2.324	0.287
27.050	33.90	86.227	102.85	2.576	0.320
28.232	34.35	87.192	101.38	2.858	0.439
29.396	34.73	88.314	99.29	3.160	0.559
30.611	35.07	89.533	100.70	3.459	0.772
31.876	35.75	90.808	101.64	3.813	0.877
33.166	36.18	92.235	102.29	4.235	1.153
34.447	36.55	93.720	102.20	4.670	1.474
35.704	36.81	95.198	104.56	5.102	1.741
36.940	37.38	96.677	106.44	5.535	2.102
38.191	37.88	98.158	108.64	5.992	2.625
39.524	38.55	99.646	109.54	6.493	3.123
40.868	39.25	101.123	111.92	7.024	3.700
42.219	39.48	102.606	112.58	7.584	4.426
43.591	41.42	104.090	113.88	8.166	5.165
44.947	41.82	105.573	115.59	8.787	6.010
46.308	43.49	107.056	117.06	9.466	7.112
47.671	44.79	108.541	119.54	10.189	8.340
49.023	46.34			10.934	9.534
50.375	47.75	2.133	0.234	11.699	10.693
51.730	49.73	2.355	0.304	12.537	12.232
53.072	52.42	2.625	0.351	13.365	13.379
54.410	55.81	2.911	0.486	14.174	14.647
55.753	57.91	3.223	0.554		
57.102	60.82	3.541	0.784	14.817	15.72
58.451	64.13	3.919	0.933	15.915	17.50
59.801	69.20	4.376	1.266	17.392	20.36
61.154	72.90	4.830	1.600	18.598	22.87
62.508	77.98	5.269	1.911	19.629	25.58
63.864	83.91	5.719	2.354	20.729	28.49
65.221	91.17	6.208	2.819	21.820	30.45
66.578	104.62	6.735	3.415	22.980	32.14
67.939	111.70	7.301	4.058	24.102	32.62
69.312	82.42	7.880	4.765	25.241	33.05
70.689	73.17	8.467	5.636	26.363	33.47

Table III-3 (continued).

T / K	C_m / $JK^{-1}mol^{-1}$	T / K	C_m / $JK^{-1}mol^{-1}$
27.490	34.16	83.706	630.16
28.941	34.60	83.862	391.59
30.660	35.33	84.019	188.75
32.308	35.76	84.175	128.77
33.914	36.51	84.326	119.36
35.538	37.02	84.475	111.74
37.252	37.60	85.084	109.18
39.096	38.45	86.112	102.91
40.947	39.42	87.345	101.11
42.879	40.59	88.892	100.99
44.820	42.93	90.437	101.62
46.660	43.62	91.913	102.67
48.515	45.91	93.414	103.58
50.448	48.07	95.186	105.24
52.387	51.15		
54.336	55.15		
56.291	59.58		
58.181	64.76		
60.079	70.53		
61.688	76.46		
63.014	80.78		
64.312	86.59		
65.511	93.49		
66.479	104.18		
67.236	112.92		
67.936	111.72		
68.630	96.35		
69.717	79.97		
71.187	72.75		
72.654	68.59		
74.119	66.25		
75.583	65.44		
77.049	66.80		
78.518	70.07		
79.744	74.64		
80.431	77.61		
80.828	79.94		
81.229	88.39		
81.629	94.29		
81.964	103.87		
82.251	115.31		
82.776	152.72		
83.023	195.05		
83.244	288.05		
83.415	446.45		
83.559	604.55		

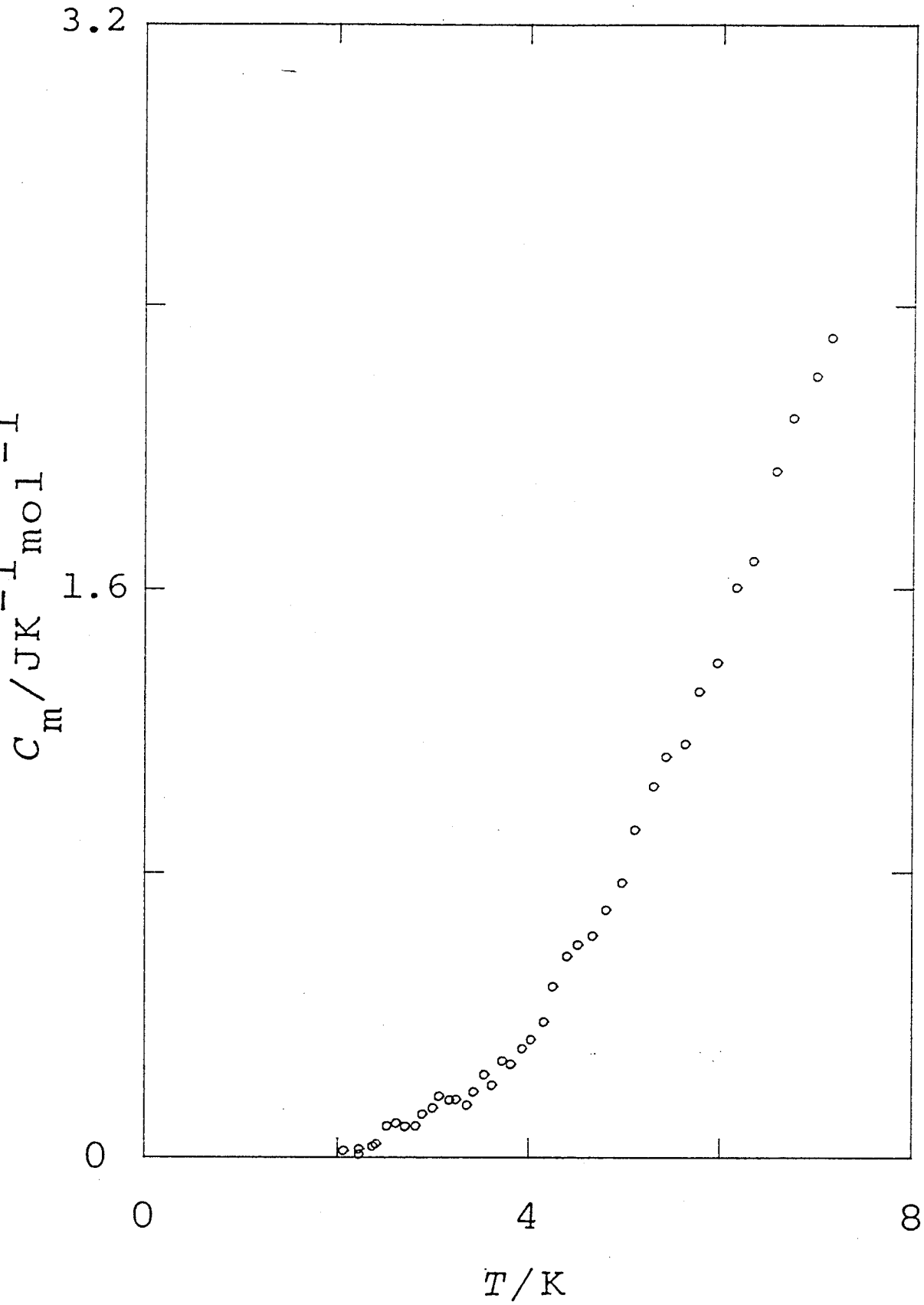

Fig. III-3 Molar heat capacity of N_2 C-phase for n_a = 0.972 mmol.

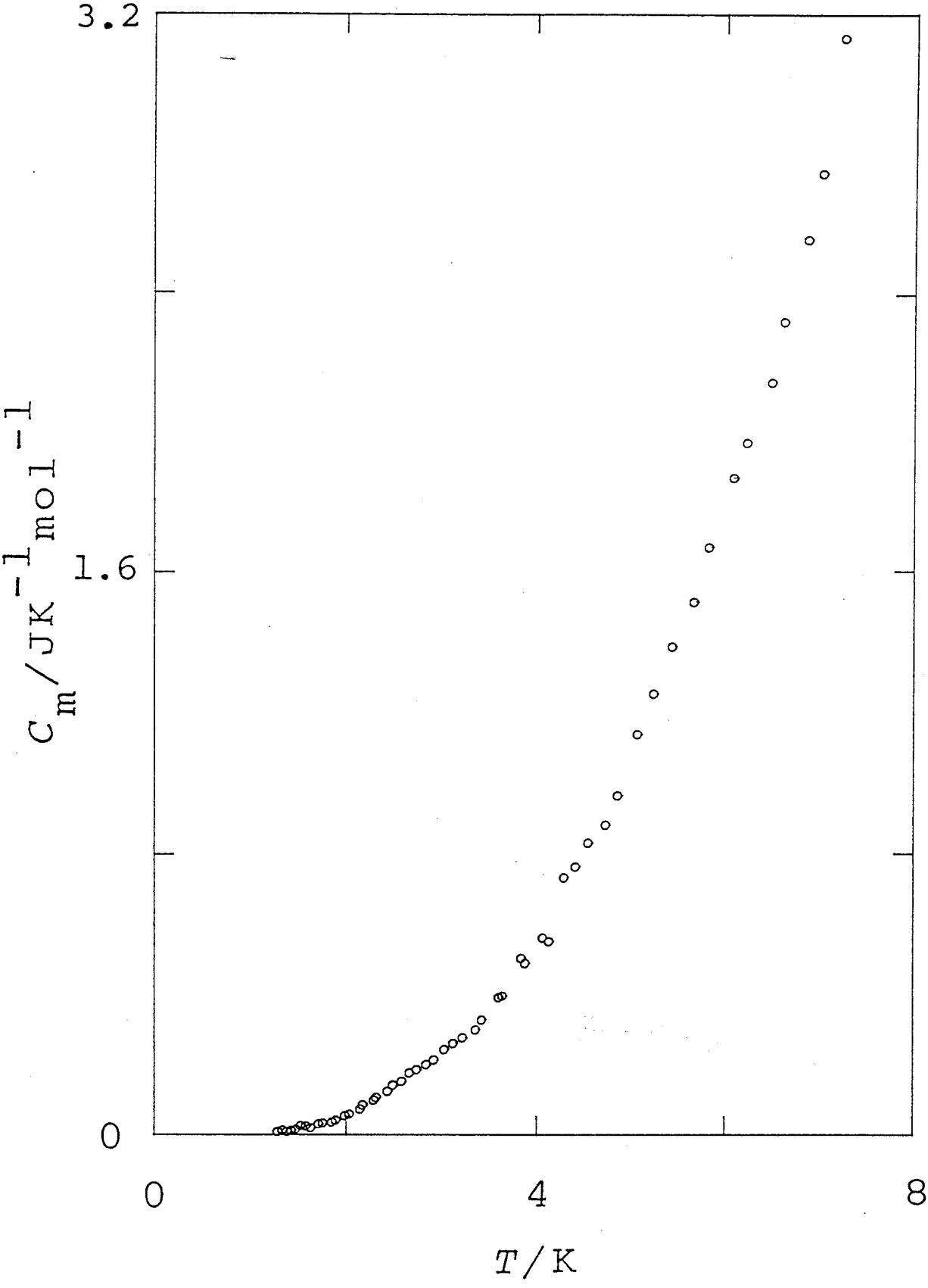

Fig. III-4 Molar heat capacity of N_2 UI-phase for n_s = 1.43 mmol.

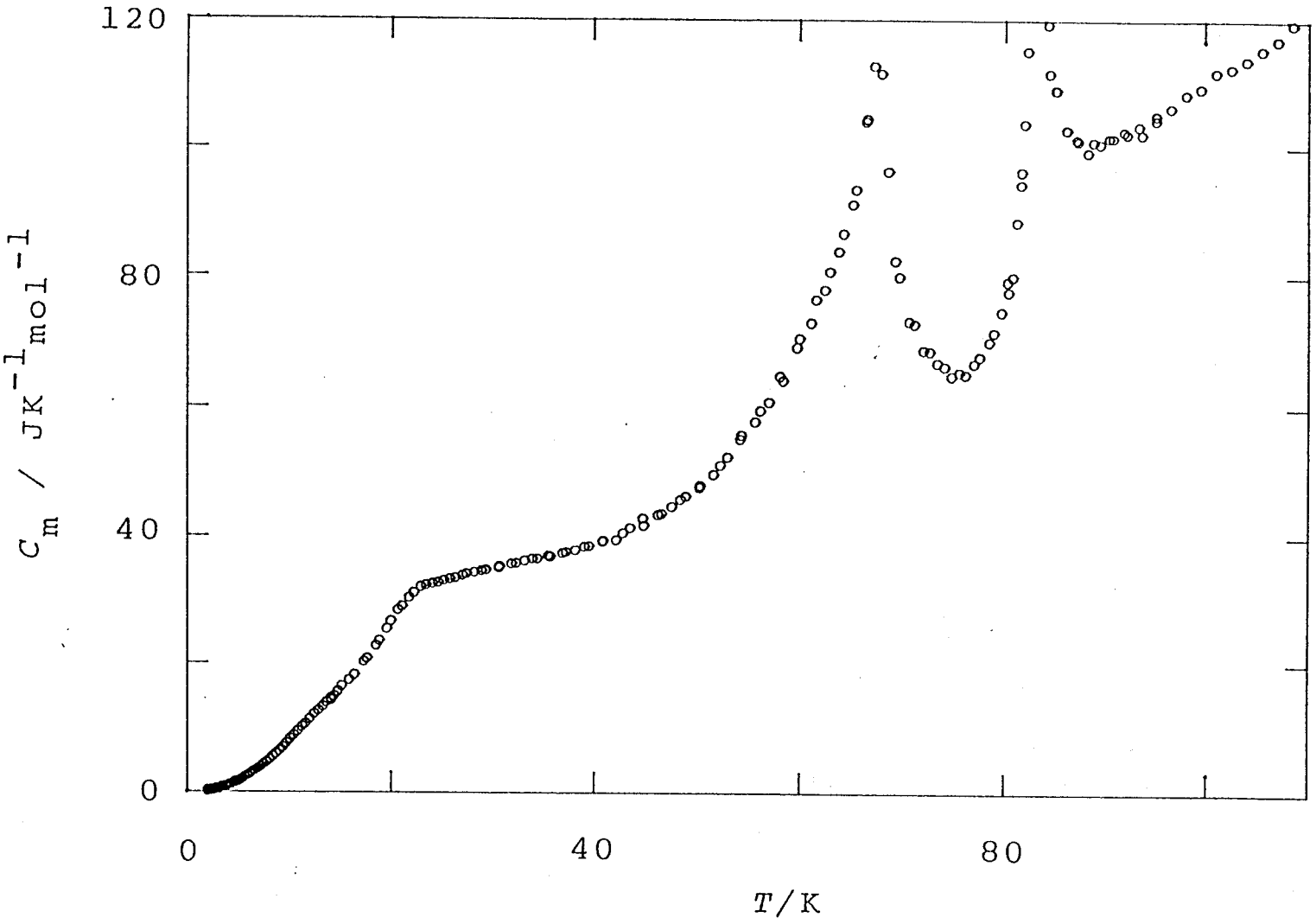

Fig. III-5(a) Molar heat capacity of N_2 TI-phase for n_a = 2.31 mmol.

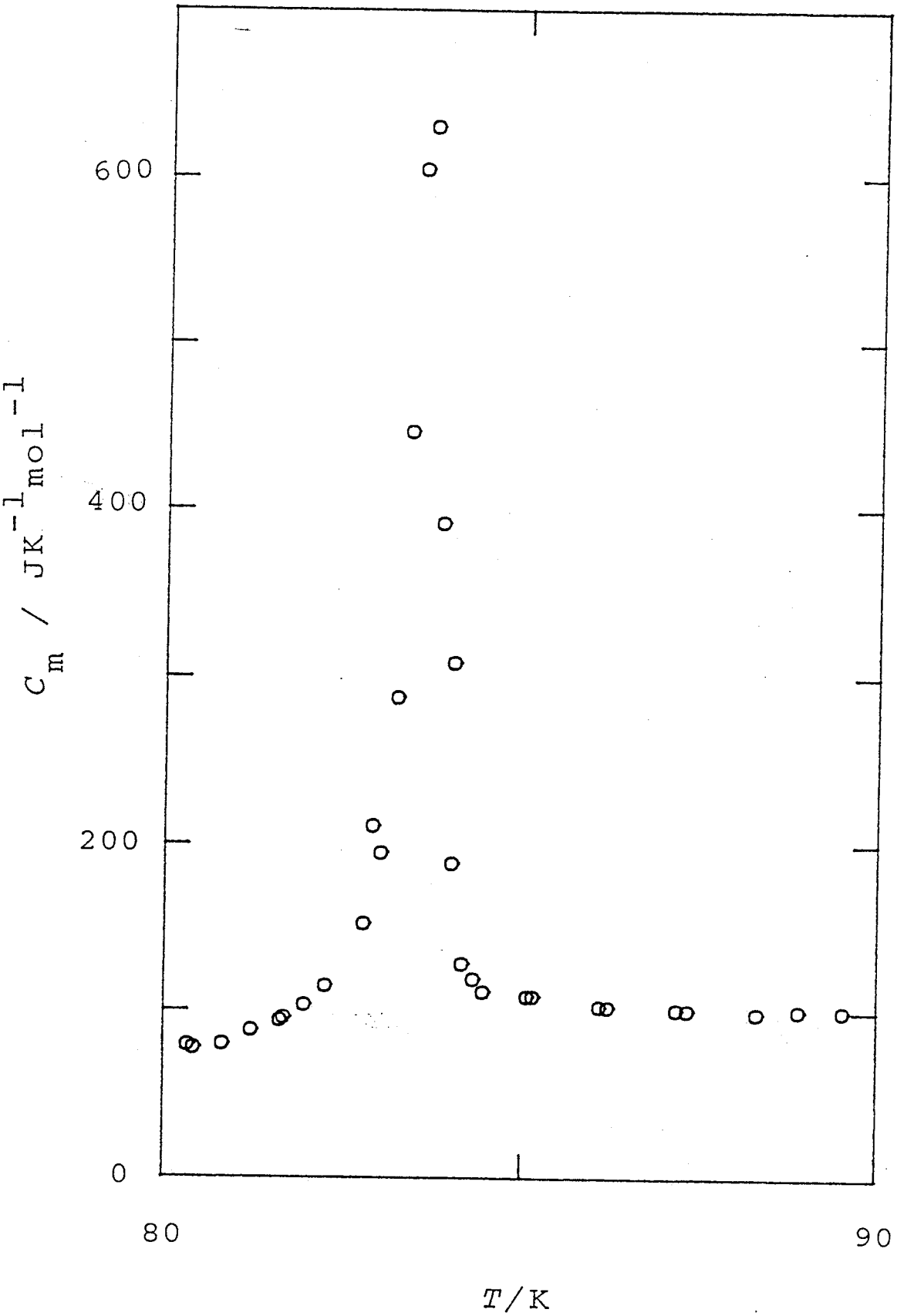

Fig. III-5(b) Molar heat capacity of N_2 TI-phase for n_a = 2.31 mmol (melting region).

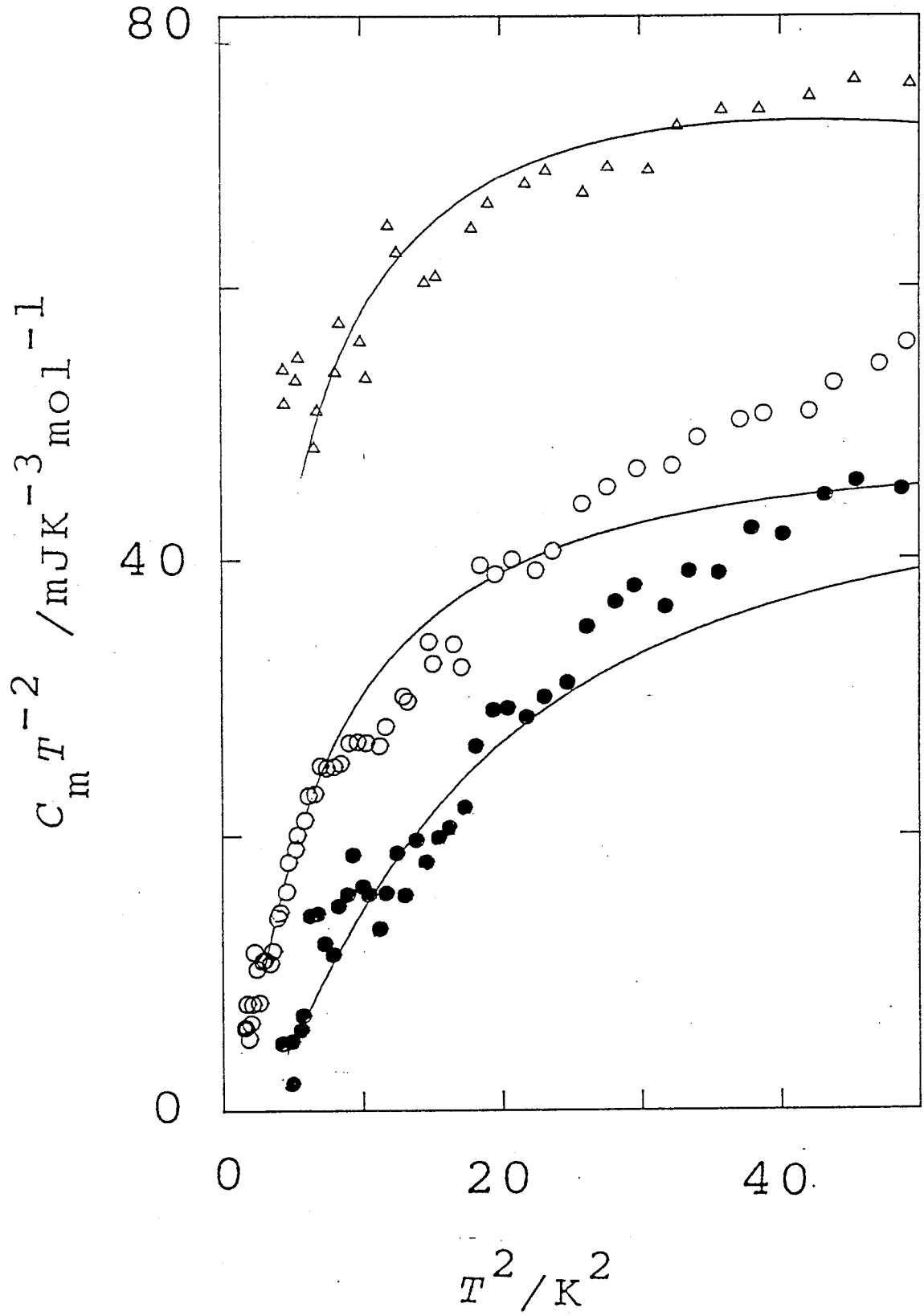

Fig. III-6 A plot of $C_m T^{-2}$ against T^2 for C- (solid circles); UI- (open circles) and TI-phases (triangles) at low temperatures. Solid lines are the fitted curves with a Debye-like model.

is assumed that the nearest-neighbor molecules of N_2 (the distance a_0 is 0.426 nm) are connected by a spring (whose force constant is α) on a triangular grid. Each molecule is also connected to the substrate in its original position by other two kinds of spring (whose force constants are k_x and k_y), where the x-axis is defined perpendicular to the glide line A as shown in Fig. III-1. It should be noted that $k_x = k_y \equiv 2\beta$ for the C-phase and $k_x = k_y = 0$ for the TI-phase. The dispersion relation for the C-phase is then given by

$$\omega^2 = [3 - (a+b+c) \pm (a^2+b^2+c^2-ab-bc-ca)^{1/2}]\alpha/m + 2\beta/m, \qquad \text{(III-1)}$$

where m is the mass of N_2 molecule, $a = \cos[q_x a_0]$, $b = \cos[(q_x + q_y\sqrt{3})a_0/2]$, $c = \cos[(-q_x + q_y\sqrt{3})a_0/2]$, and q_x, q_y are the components of momentum of the phonons along the Cartesian coordinates. The calculation of the dispersion relation is straightforward, with two constants (α and β), as adjustable parameters. The equation tells us the presence of a frequency gap, $(2\beta/m)^{1/2}$, at the Γ-point ($q_x = q_y = 0$, or $a = b = c = 1$). For the TI-phase ($\beta \to 0$), it has no gap.

In order to describe the UI-phase, it is assumed that $k_x = 2\beta$ and $k_y = 0$, which means that the molecule is restricted only in the x-direction by the substrate with the same strength as in the C-phase. It is also assumed that α and a_0 have common values irrespectively of uniaxial compression. In other words the UI-phase is regarded as an equilateral triangular lattice. The dispersion relation for the UI-phase is now given by

$$\omega^2 = \{3 - (a+b+c) \pm [a^2+b^2+c^2-(ab+bc+ca)+(\beta/\alpha)^2+(b+c-2a)\beta/\alpha]^{1/2}\}\alpha/m + \beta/m. \qquad \text{(III-2)}$$

The equation shows that one of the branches (+ part) has the same gap as in the C-phase and the other (- part) has no gap at the Γ-point.

The phonon density of states was then calculated at certain momentum transfer Q for the irreducible 1/12 sector of the Brillouin zone. The results are schematically shown in Fig.

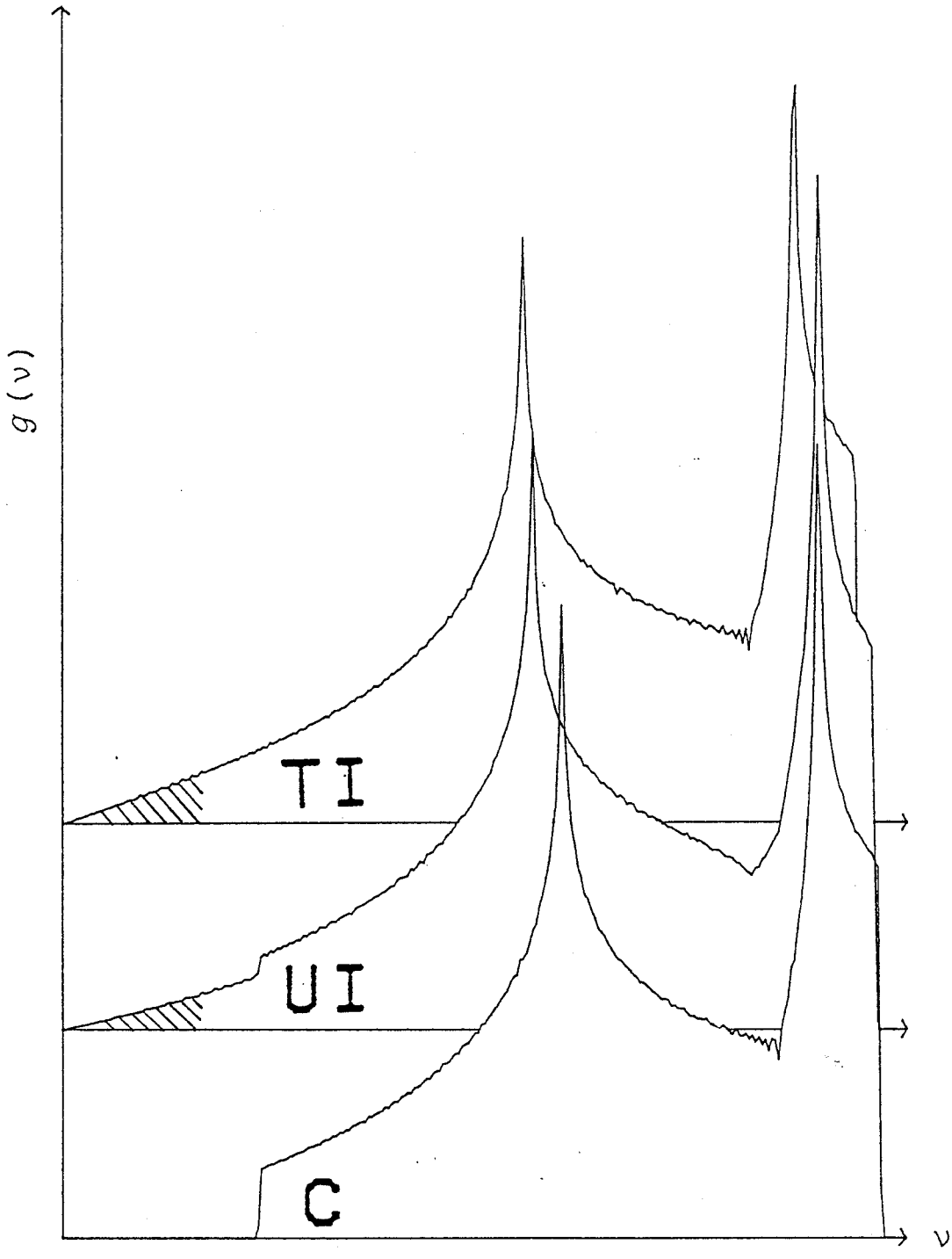

Fig. III-7 Schematic drawings of the phonon density of states $g(\nu)$. C, commensurate phase; UI, uniaxially incommensurate phase; TI, triangular incommensurate phase.

Table III-4 The characteristic temperatures obtained for the N_2 monolayers on graphite for the Debye model with cut-off and size effects.

	Θ_D /K	Θ_c or Θ_s * /K	Θ_E ** /K
C-phase	67 ± 1	15 ± 1	65 ± 1
UI-phase	65 ± 1	9 ± 1	66 ± 1
TI-phase	55 ± 1	7 ± 1	66 ± 1

* Θ_s means the size effect temperature.

** Θ_E ($3N$ degrees of freedom) was obtained from the heat capacity at higher temperatures (ref. 15).

Table III-5 The fitting parameters obtained for the N_2 monolayers on graphite determined by the lattice dynamics.

	α/Nm^{-1}	β/Nm^{-1}
C-phase	0.48	0.09
UI-phase	0.48	0.09
TI-phase	0.39	——

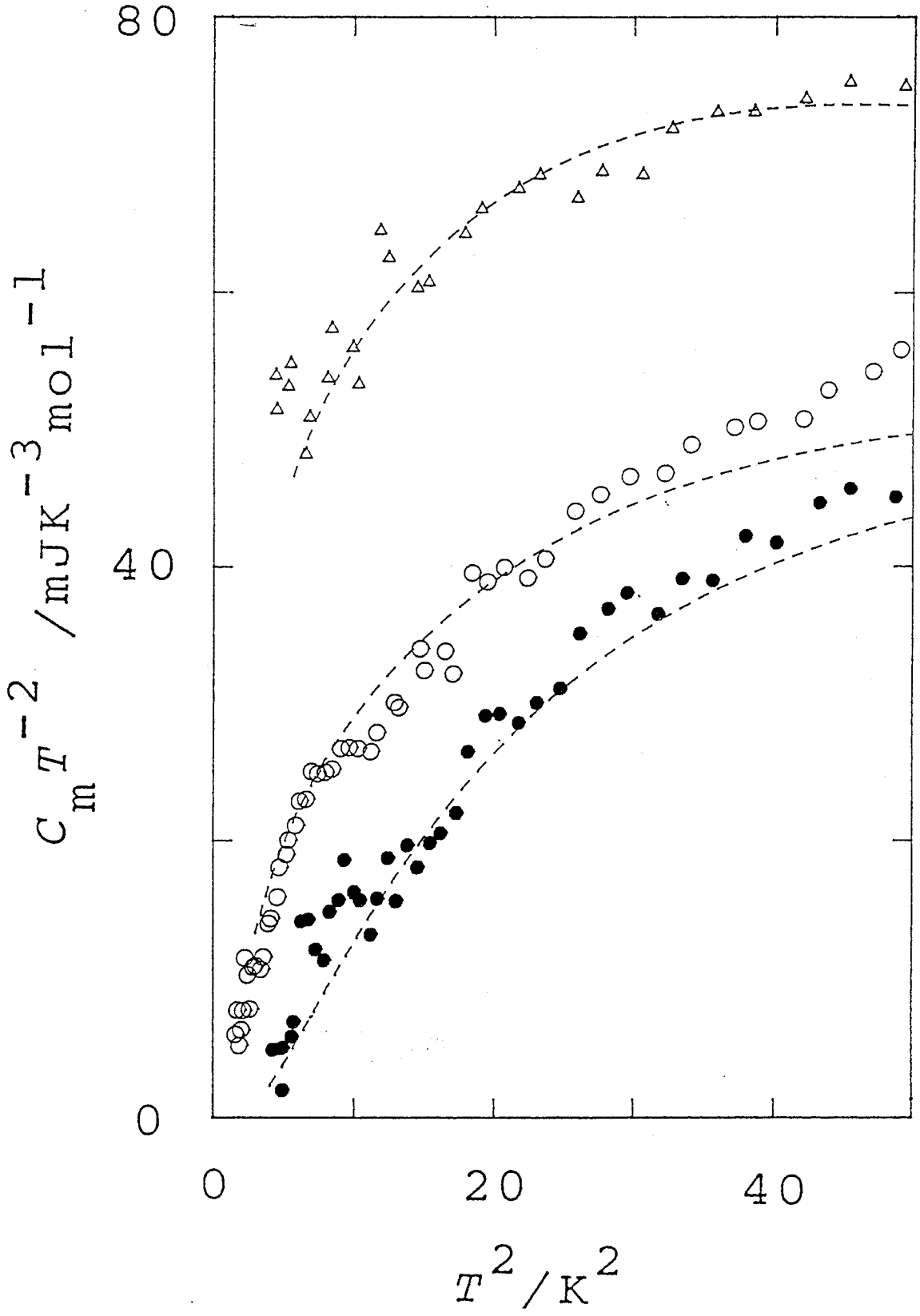

Fig. III-8 A plot of $C_m T^{-2}$ against T^2 for C- (solid circles); UI- (open circles) and TI-phases (triangles) at low temperatures. Broken lines are the fitted curves based on the phonon density of states.

III-7, indicating that the C-phase has a cut-off at low-frequency end and the TI-phase does not. It should be noted that the UI-phase has no intrinsic cut-off, but has a small and clear jump at the same frequency as in the C-phase.

The experimental heat capacities were fitted to the density of states with α and β as adjustable parameters. The actual fittings are shown in Fig. III-8, where the force constants obtained for each phase are tabulated in Table III-5. For the TI- and UI-phases, the size effect discussed in Chapter II was also considered and the characteristic temperature Θ_s was obtained from the fitting; 6.0 K for the TI-phase and 6.3 K for the UI-phase. The fact may indicate that the vibrational states of the incommensurate solids are specified by the substrate size.

III-3-3 Order-Disorder Phase Transition

A phase transition was found in the TI-phase. The heat capacity anomaly is shown in Fig. III-9. While the transition temperature, 24 K, is significantly lower than that for the C-phase (27.5 K) and for the UI-phase (28.7 K) (ref. 15), the nature would be similar; orientational order-disorder. An x-ray diffraction study (ref. 4) claimed the gradual decrease in the superlattice intensity. Zhang, *et al.* could not locate this transition and suggested a gradual disordering without exhibiting any distinct phase transition (ref. 13). Assuming an appropriate normal portion of the heat capacity, the entropy of the transition $\Delta_{trs}S$ was determined to be about 3.3 $JK^{-1}mol^{-1}$. The amount is considerably smaller than those for the C- and UI-phases (5.9 $JK^{-1}mol^{-1}$ and 5.0 $JK^{-1}mol^{-1}$, respectively, ref. 15), even if somewhat arbitrary nature of the base line especially at the high temperature side is taken into account.

III-3-4 New Phase Transition in TI-Phase

An additional but large anomaly was found newly at 67.6 K below the melting temperature of the TI-phase (83.5 K), as shown in Fig. III-10. Little can be said about the nature because the

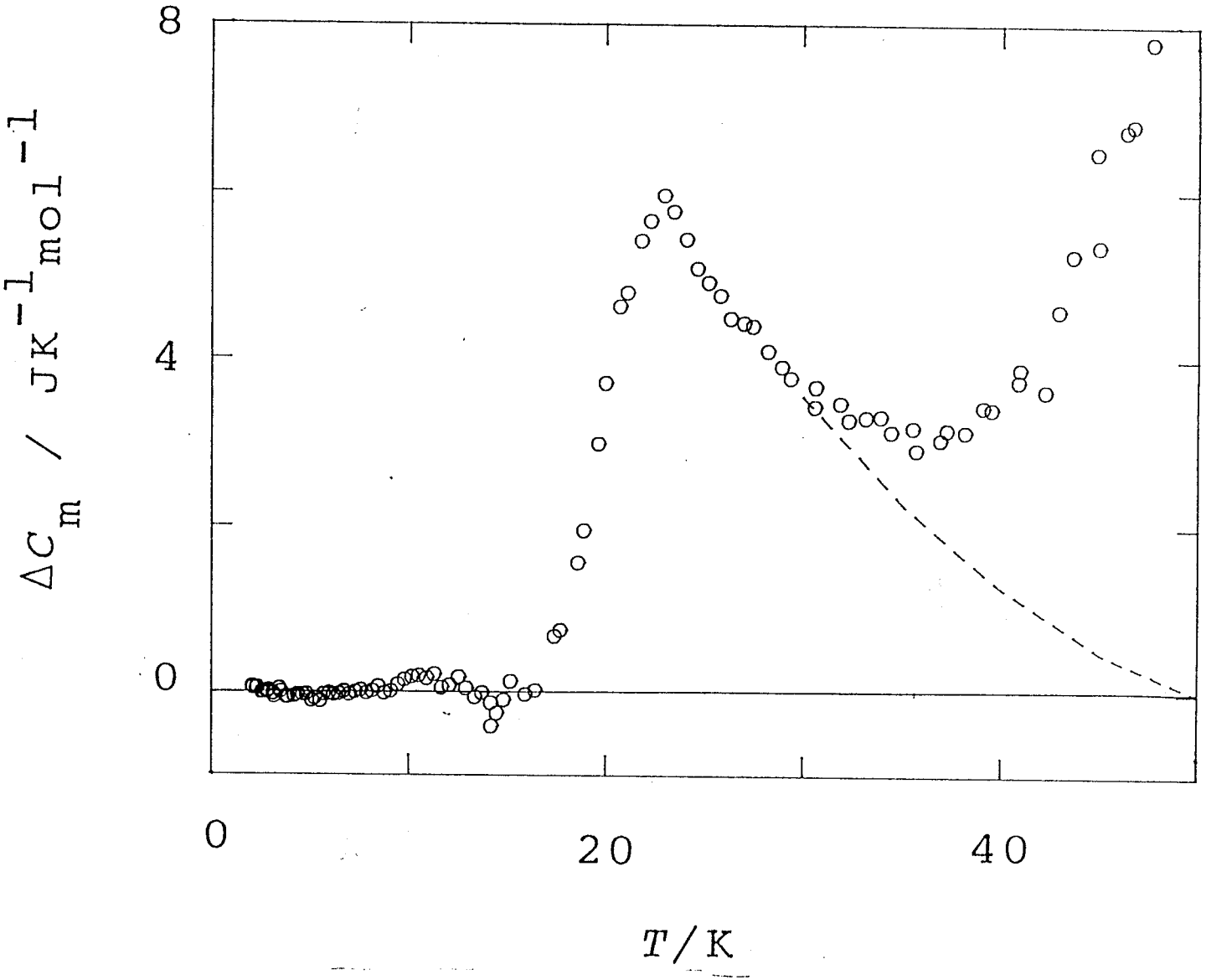

Fig. III-9 Excess heat capacity for the TI-phase of N2/graphite, which is probably due to the order-disorder transition.

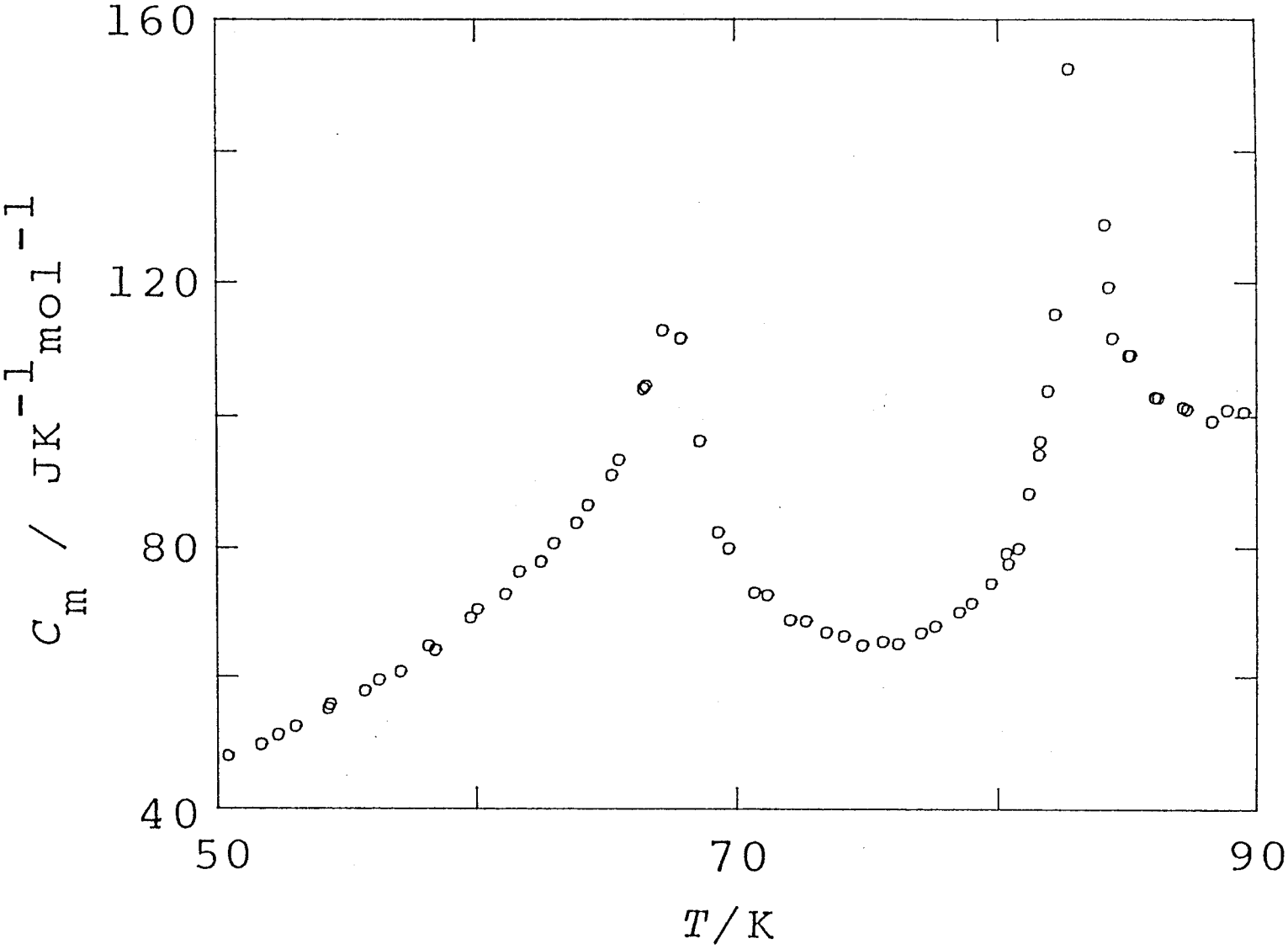

Fig. III-10 Molar heat capacity of N_2 for TI-phase.

phase diagram is expected to be rather complicated at such high coverages and high temperatures. However, the existence of a re-entrant fluid (RF) phase between the C- and UI-phases is highly probable (ref. 15), as in the case of CO on graphite (ref. 16). Alternatively, three transitions (TI → UI, UI → RF and RF → C) may come together to show the large and wide anomaly.

References to Chapter III

1. A.B. Harris and A.J. Berlinsky, *Can. J. Phys.* 57, 1852 (1979).
2. R.D. Diehl, M.F. Toney and S.C. Fain, Jr., *Phys. Rev. Lett.* 48, 177 (1982).
3. R.D. Diehl and S.C. Fain, Jr., *Surf. Sci.* 125, 116 (1983).
4. K. Morishige, C. Mowforth and R.K. Thomas, *Surf. Sci.* 151, 289 (1985).
5. R.D. Diehl and S.C. Fain, Jr., *Phys. Rev.* B26, 4785 (1982).
6. H. You and S.C. Fain, Jr., *Faraday Discuss. Chem. Soc.* 80, 159 (1985).
7. R. Wang, S.-K. Wang, H. Taub, J.C. Newton and H. Shechter, *Phys. Rev.* B35, 5841 (1987).
8. J. Talbot D.J. Tildesley and W.A. Steele, *Surf. Sci.* 169, 71 (1986).
9. F.Y. Hansen, V.L.P. Frank, H. Taub, L.W. Bruch, H.J. Lauter and J.R. Dennison, *Phys. Rev. Lett.* 64, 764 (1990).
10. H.J. Lauter, V.L.P. Frank, H. Taub and P. Leiderer, *Physica* B 165&166, 611 (1990).
11. A.D. Migone,H.K. Kim, M.H.W. Chan, J. Talbot, D.J. Tildesley and W.A. Steele, *Phys. Rev. Lett.* 51, 192 (1983).
12. M.H.W. Chan, A.D. Migone, K.D. Miner and Z.R. Li, *Phys. Rev.* B30, 2681 (1984).
13. Q.M. Zhang, H.K. Kim and M.H.W. Chan, *Phys. Rev.* B32, 1820 (1985).
14. G. Cardini and F. O'shea, *Surf. Sci.* 154, 231 (1985).
15. A. Inaba, T. Shirakami and H. Chihara, *J. Chem. Thermodyn.* 23, 461 (1991).
16. Y.P. Feng and M.H.W. Chan, *Phys. Rev. Lett.* 64, 2148 (1990).

Chapter IV Mixture of CO and N_2 on Graphite

IV-1 Introduction

There are several diffraction studies for binary mixtures composed of simple molecules adsorbed on graphite: CO and Ar (refs. 1 and 2), N_2 and Ar (ref. 2), *etc.* For the bulk system, CO and Ar are partly miscible (ref. 3), whereas N_2 and Ar are completely miscible (ref. 4) in their condensed states. In contrast to the adsorbed monolayer, both systems form a molecular compound. We investigate here the mixture of CO and N_2.

While the chemical properties of CO and N_2 are fairly different, the molecules CO and N_2 are similar in size, mass, and electronic configurations except in polarity. They form the same crystal structure in the bulk (both in α- and β-phases). In general, such similar molecules readily form a substitutional solid solution. In fact, they form an ideal solid solution at all concentrations in both α- and β-phases (refs. 5 and 6).

The structure of the monolayer on graphite is also similar. The CO monolayer has a $\sqrt{3}\times\sqrt{3}$ commensurate in-plane herringbone structure (refs. 7 and 8). Because of the polarity of CO molecule, the commensurate phase of CO monolayer transforms further into a completely ordered phase below 5.4 K (ref. 9). The corresponding transition does not occur in the bulk CO. Indeed, the CO crystal forms an orientational glass (ref. 10) due to prolongation of relaxation time for the reorientational process.

A diffraction study may provide some information on what happens in the mixture if some molecular compound is formed. The thermodynamic study would be better to approach the problem and obtain the whole picture.

IV-2 Experimental Details

The adiabatic calorimeter assembly, the calorimeter vessel and the measuring system were the same as those described in

the previous chapters. The gases were purchased from Takachiho Kagaku. The stated purity was 99.95 % for CO and 99.9999 % for N_2. Three mixtures were examined. The actual amounts of the gases introduced into the vessel are summarized in Table IV-1. The ratio of the amount of CO and that of N_2 was varied, keeping the total amount almost constant so as to correspond to the commensurate coverage in each experiment. Hereafter we call those mixtures [2:1], [1:1] and [1:2].

IV-3 Results and Discussion

IV-3-1 Heat Capacity

The molar heat capacities obtained between 2 and 84 K are listed in Tables IV-2, IV-3 and IV-4, respectively and are reproduced in Figs. IV-1, IV-2, and IV-3, respectively.

IV-3-2 Phase Relation

In order to obtain the excess heat capacity for each sample, the normal portion of the heat capacity was eliminated as follows. For the pure N_2, we used the same parameters as those obtained in the previous chapter; 69 K for Θ_D, 15 K for Θ_c and 65 K for Θ_E. For the pure CO, however, the same procedure could not be applied because of the anomaly at the lowest temperature region. Indeed, the Θ_D for the pure CO was assumed to be 85 K by using the ratio of the Debye temperatures for the bulk solids CO and N_2 (103/83.5, ref. 12). The Θ_c and Θ_E for the pure CO were assumed to be the same as those for the pure N_2. For the mixtures, the normal heat capacity was obtained from the Neumann-Kopp's law. The resultant excess heat capacities are illustrated in Figs. IV-4 and IV-5.

For the pure CO, there are two anomalies in its two-dimensional solid phase; one at 5.4 K and the other around 19 K. The former is associated with the head-to-tail order-disorder transition (refs. 9 and 11). As the system is diluted with N_2, the transition becomes diffuse, suggesting that CO and N_2 are

Table IV-1 The actual amount of the gases used for the mixtures.

sample mame	amount of CO / mmol	amount of N_2 / mmol	total / mmol
2:1	1.046	0.523	1.569
1:1	0.783	0.782	1.565
1:2	0.530	1.048	1.578

Table IV-2 Molar heat capacity of CO and N_2 2:1 mixture on graphite.

T / K	C_m / $JK^{-1}mol^{-1}$	T / K	C_m / $JK^{-1}mol^{-1}$	T / K	C_m / $JK^{-1}mol^{-1}$
14.305	14.58	68.082	46.88	2.274	0.443
15.591	17.15	69.258	47.63	2.513	0.522
16.859	19.34	70.435	46.61	2.828	1.040
17.944	21.08	71.612	44.88	3.274	1.184
19.052	23.76	72.788	45.05	3.804	2.051
20.270	25.83	73.968	42.81	4.384	2.206
21.413	27.78	75.148	44.36	4.956	3.088
22.478	29.11	76.327	43.31	5.489	3.256
23.589	31.23	77.508	44.96	5.999	3.855
24.706	32.86	78.690	45.96	6.513	4.244
25.837	33.68	79.873	47.95	7.081	5.049
26.970	33.75	81.057	48.78	7.725	5.636
28.061	34.53	82.241	50.47	8.436	6.615
29.156	34.75	83.426	52.78	9.190	7.662
30.302	35.63	84.612	55.18	9.980	8.831
31.502	36.45			10.810	10.081
32.654	37.16	2.159	0.251	11.668	11.382
33.761	37.92	2.369	0.543	12.548	12.708
34.917	38.60	2.646	0.863	13.408	14.023
36.242	39.52	2.962	1.140		
37.670	40.33	3.301	1.377	14.429	15.40
39.083	41.24	3.724	1.901	15.609	17.13
40.442	42.22	4.234	2.189	16.959	19.50
41.797	43.77	4.722	2.617	18.351	22.09
43.156	45.70	5.193	2.949	19.600	24.47
44.470	48.05	5.664	3.450	20.768	27.26
45.741	52.39	6.178	4.016	21.941	28.28
46.924	59.86	6.750	4.629	23.102	30.46
48.065	82.03	7.388	5.332	24.198	32.30
49.206	112.35	8.066	6.242	25.276	33.48
50.403	98.09	8.782	7.044	26.394	33.52
51.617	88.27	9.559	8.205	27.513	34.25
52.789	80.71	10.388	9.371	28.602	34.66
53.981	74.88	11.237	10.654	29.699	35.29
55.188	68.33	12.116	12.195	30.843	36.26
56.362	63.44	13.017	13.407	31.988	36.93
57.524	59.65	13.922	14.790	33.086	37.64
58.709	55.77			34.195	38.43
59.891	53.03	2.250	0.314	35.313	38.91
61.055	50.32	2.470	0.734	36.430	39.35
62.224	48.38	2.808	0.875	37.587	40.24
63.395	47.20	3.260	1.420	38.930	41.41
64.565	46.88	3.802	1.757	40.847	42.84
65.734	46.31	4.306	2.507	42.596	44.96
66.906	46.41	4.808	3.177	43.771	46.65

Table IV-2 (continued).

T / K	C_m / $JK^{-1}mol^{-1}$	T / K	C_m / $JK^{-1}mol^{-1}$	T / K	C_m / $JK^{-1}mol^{-1}$
44.938	49.04	49.391	114.03	61.577	49.16
45.804	52.54	49.809	107.45	62.748	47.27
46.392	56.22	50.222	100.45	63.925	47.14
46.879	59.39	51.028	92.34	65.412	46.46
47.221	63.10	52.214	84.02	67.176	45.81
47.505	67.76	53.415	78.13	68.915	47.17
47.791	73.36	54.599	71.71	70.660	45.70
48.087	80.90	55.757	65.68	72.405	45.07
48.364	91.48	56.917	60.95	74.164	43.38
48.618	105.60	58.079	57.72	75.936	43.53
48.865	111.99	59.242	56.17	77.696	46.53
49.081	117.46	60.409	52.26	79.449	48.46

Table IV-3 Molar heat capacity of CO and N_2 1:1 mixture on graphite.

T / K	C_m / $JK^{-1}mol^{-1}$	T / K	C_m / $JK^{-1}mol^{-1}$	T / K	C_m / $JK^{-1}mol^{-1}$
14.435	14.03	55.666	59.75	2.169	0.336
15.598	16.08	57.252	49.50	2.406	0.682
16.850	17.94	58.717	45.97	2.717	0.985
18.049	20.49	60.161	43.98	3.168	1.071
19.138	22.70	61.604	42.04	3.681	1.438
20.289	25.10	63.047	41.41	4.225	1.717
21.484	26.95	64.465	40.60	4.793	2.069
22.590	29.11	65.888	40.31	5.377	2.534
23.527	30.94	67.344	41.11	6.000	3.011
24.291	32.36	68.778	40.82	6.652	3.702
25.049	34.12	70.213	41.13	7.369	4.390
25.800	36.49	71.677	40.59	8.145	5.075
26.544	36.02	73.141	41.52	8.976	6.139
27.294	35.10	74.606	41.48	9.900	7.485
28.054	34.91	76.072	43.01	10.878	8.780
28.837	34.90	77.539	43.12	11.897	10.452
29.736	35.41	79.009	43.79	12.851	11.875
30.783	35.90	80.481	46.16	13.666	13.161
31.919	36.81	81.955	46.96		
33.398	37.68	83.429	47.69	14.295	13.56
35.020	38.51	84.903	53.10	15.301	15.73
36.510	38.85			16.412	17.29
38.040	39.88	2.090	0.410	17.630	19.56
39.494	40.98	2.264	0.392	18.850	22.19
40.884	42.12	2.573	0.516	20.023	24.72
41.954	43.27	2.943	0.839	21.028	26.63
42.752	44.86	3.404	1.303	21.924	27.93
43.664	46.09	3.959	1.608	22.768	29.38
44.472	47.71	4.524	1.920	23.547	30.91
45.165	49.93	5.092	2.346	24.332	32.49
45.889	54.13	5.696	2.764	24.934	34.13
46.614	60.04	6.343	3.412	25.466	35.52
47.338	69.60	7.037	3.930	26.028	36.48
47.895	86.03	7.763	4.728	26.586	36.03
48.225	103.78	8.539	5.590	27.386	35.24
48.467	118.39	9.422	6.644	28.285	34.95
48.672	132.61	10.403	8.225	29.119	34.91
48.871	153.55	11.389	9.551	29.963	35.38
49.072	149.83	12.393	11.223	31.168	36.35
49.272	142.79	13.357	12.580	32.662	37.09
49.499	135.63	14.227	13.977	34.071	37.83
49.914	124.28			35.508	38.44
50.646	107.28			37.014	39.19
51.593	96.13			38.605	40.60
52.726	88.38			40.039	41.30
54.090	75.43			41.341	42.74
				42.741	44.58

Table IV-3 (continued).

T / K	C_m / $JK^{-1}mol^{-1}$	T / K	C_m / $JK^{-1}mol^{-1}$	T / K	C_m / $JK^{-1}mol^{-1}$
44.027	46.72	50.122	113.80	63.846	40.35
45.090	49.80	50.542	105.13	65.300	41.05
45.947	54.34	51.006	98.46	66.642	40.72
46.869	63.16	51.523	94.01	67.990	40.30
47.179	65.94	52.092	88.87	69.456	40.58
47.499	73.49	52.722	85.06	70.929	42.01
47.836	82.55	53.410	80.27	72.404	41.63
48.173	99.57	54.108	73.25	73.877	42.09
48.434	119.11	54.793	64.59	75.350	43.27
48.624	135.64	55.481	57.98	76.827	43.78
48.813	143.15	56.208	52.26	78.305	44.47
49.002	146.18	56.955	47.88	79.783	44.97
49.192	143.80	58.046	45.59	81.264	46.62
49.382	137.97	59.497	44.27	82.745	49.19
49.576	130.12	60.947	42.21		
49.799	124.13	62.395	40.83		

Table IV-4 Molar heat capacity of CO and N_2 1:2 mixture on graphite.

T / K	C_m / $JK^{-1}mol^{-1}$	T / K	C_m / $JK^{-1}mol^{-1}$	T / K	C_m / $JK^{-1}mol^{-1}$
14.395	13.67	64.460	47.30	2.595	0.613
15.601	16.07	65.912	46.86	2.871	0.714
16.824	18.21	67.367	46.64	3.168	0.778
18.009	20.76	68.829	45.86	3.535	0.918
19.200	23.64	70.291	45.98	4.002	1.086
20.307	26.55	71.752	44.75	4.513	1.361
21.347	28.13	73.214	43.92	5.036	1.706
22.412	30.35	74.679	43.64	5.559	1.981
23.586	33.05	76.148	45.51	6.105	2.450
24.838	36.15	77.618	47.69	6.664	2.936
26.056	41.11	79.088	48.18	7.260	3.517
27.203	42.13	80.558	49.55	7.908	4.326
28.326	39.10	82.030	52.60	8.615	5.036
29.491	38.53	83.503	54.77	9.367	6.029
30.670	38.80	84.975	60.86	10.154	7.228
31.819	39.33			12.716	11.339
32.924	39.59	2.145	0.213	13.512	12.544
34.033	40.08	2.351	0.470		
35.146	40.46	2.617	0.550	14.606	14.81
36.265	41.11	2.914	0.712	16.079	16.97
37.423	41.82	3.631	1.044	17.337	19.21
38.622	42.11	4.162	1.258	18.516	22.15
39.786	43.58	4.701	1.476	19.746	24.97
40.917	43.75	5.246	1.666	20.926	27.78
42.053	44.96	5.798	2.244	21.957	29.29
43.215	46.37	6.341	2.636	22.812	31.22
44.418	48.84	6.913	3.186	23.718	33.39
45.529	52.52	7.550	3.858	24.403	34.69
46.447	57.36	8.227	4.602	24.849	35.89
47.216	63.27	8.939	5.466	25.359	37.52
47.901	75.50	9.712	6.570	25.809	39.25
48.580	94.39	10.534	7.861	26.228	41.34
49.264	105.80	11.374	9.102	26.575	44.16
49.949	101.25	12.201	10.335	26.933	43.43
50.636	94.17	13.043	11.799	27.404	41.12
51.495	87.92	13.855	13.107	28.002	39.44
52.498	82.47			28.943	38.95
53.631	77.34	2.128	0.234	30.191	38.58
54.900	72.22	2.327	0.337	31.394	39.26
56.152	66.84	2.576	0.409	32.895	39.93
57.412	62.61	2.872	0.589	34.552	40.41
58.687	58.68	3.193	0.819	36.080	41.09
60.082	54.14	3.574	0.873	37.624	41.59
61.557	50.04	2.130	0.153	39.173	42.80
63.007	48.65	2.341	0.364	40.733	43.61

Table IV-4 (continued).

T / K	C_m / $JK^{-1}mol^{-1}$
42.356	45.53
43.756	47.55
44.845	49.90
45.894	53.92
46.784	59.73
47.601	69.98
48.157	81.56
48.386	89.70
48.593	97.32
48.762	97.76
48.931	103.27
49.109	105.95
49.354	107.50
49.654	105.72
49.950	102.09
50.247	98.74
50.560	95.63
51.085	91.25
51.973	86.40
53.096	80.65
54.303	74.87
55.540	69.71
56.794	65.51
58.100	59.86
59.450	57.75
60.804	52.09
62.161	49.21
63.520	48.24
64.880	47.12
66.239	46.90
67.602	45.51
68.969	45.10
70.335	45.03
71.701	45.31
73.518	43.41
75.398	45.79
76.879	46.35
78.346	47.34
79.816	48.30
81.286	50.17

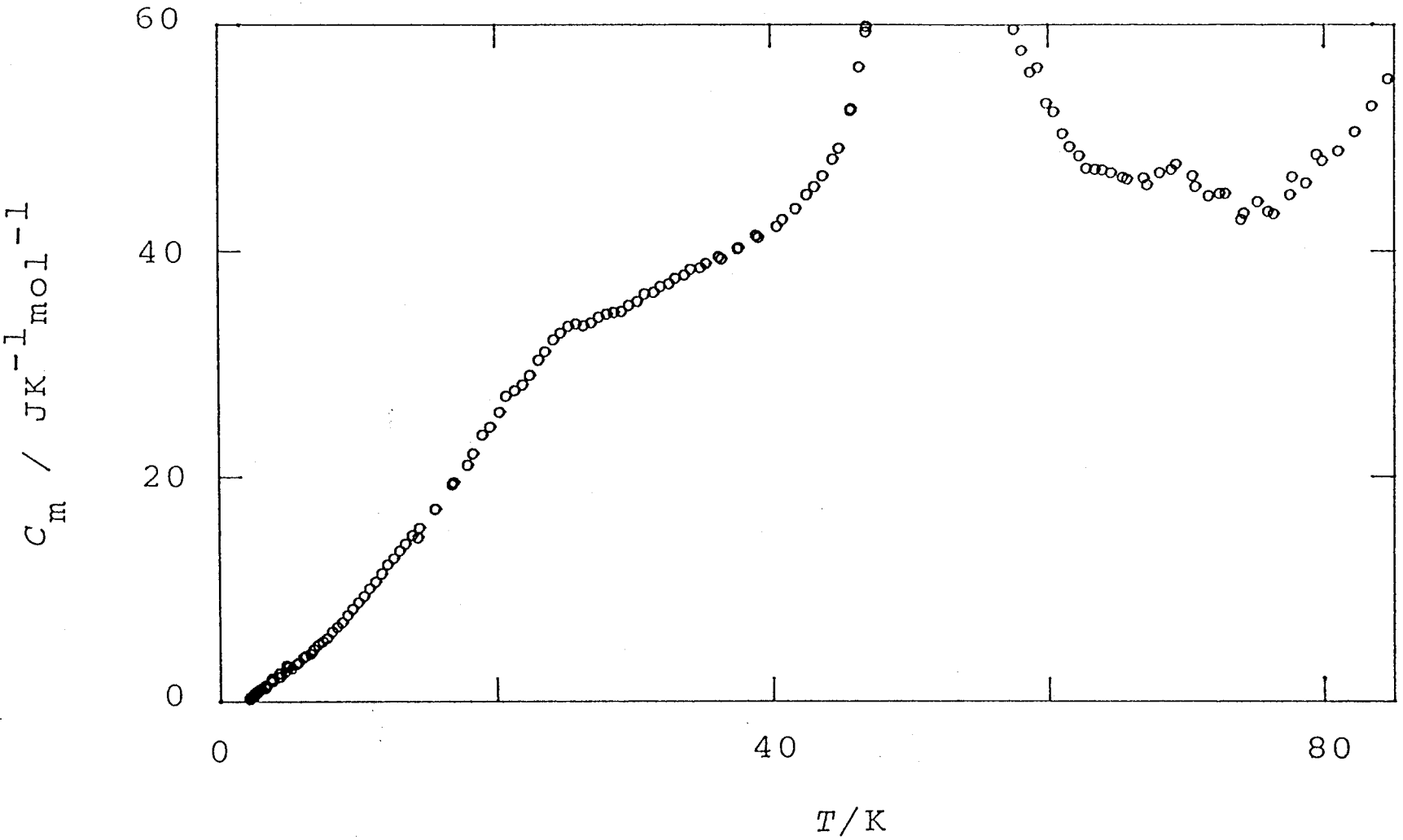

Fig. IV-1(a) Molar heat capacity of CO and N_2 2:1 mixture on graphite.

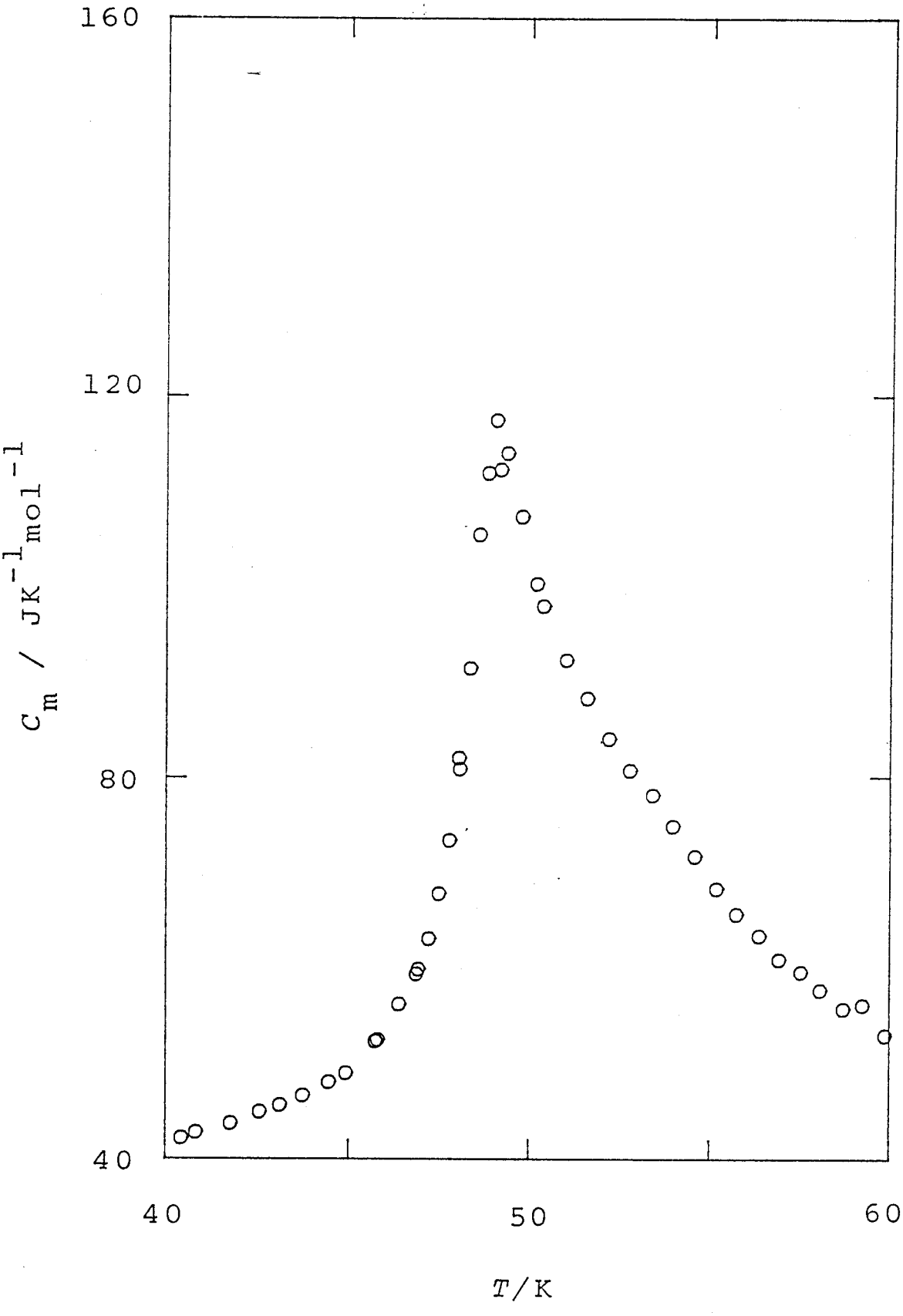

Fig. IV-1(b) Molar heat capacity of CO and N_2 2:1 mixture on graphite (melting region).

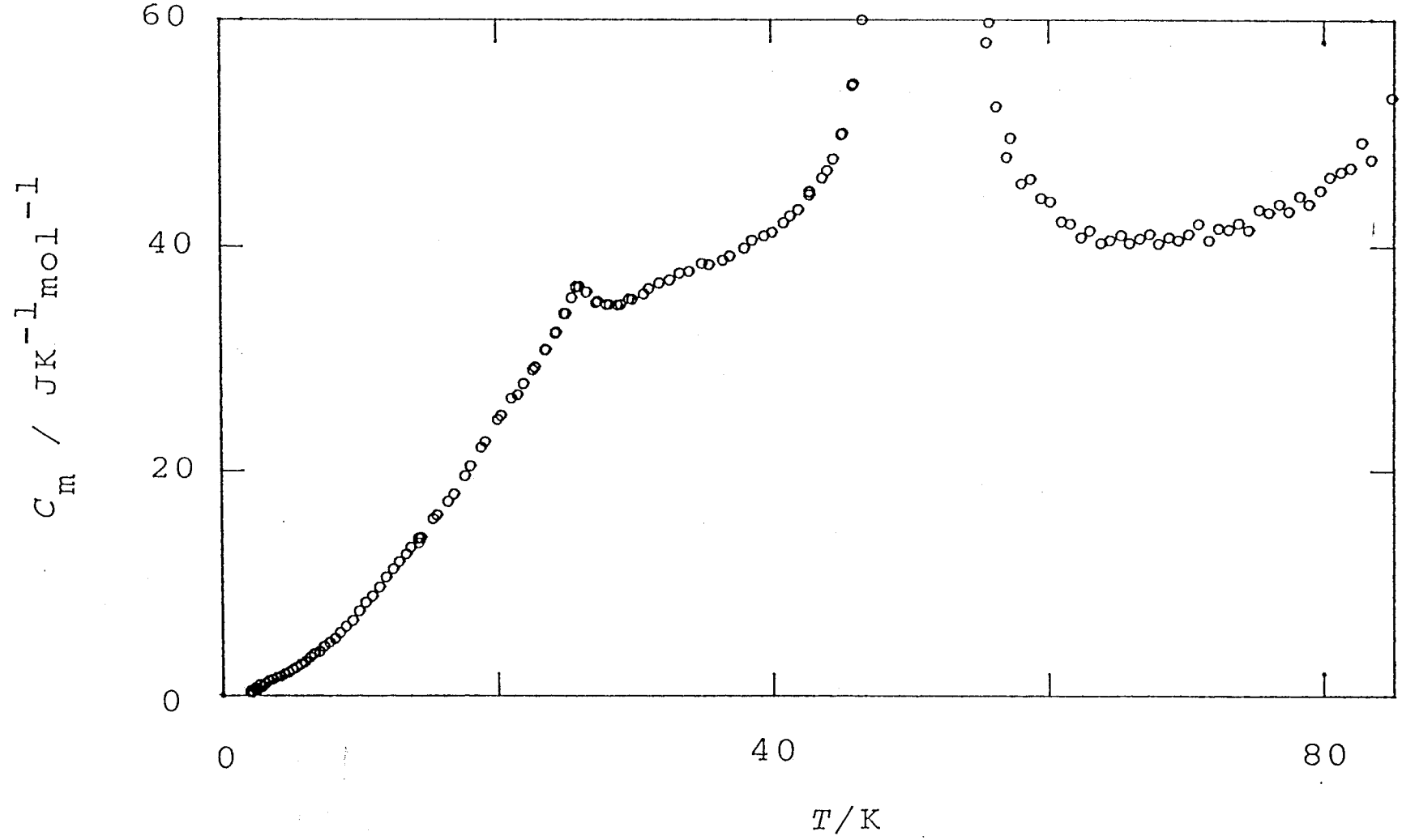

Fig. IV-2(a) Molar heat capacity of CO and N_2 1:1 mixture on graphite.

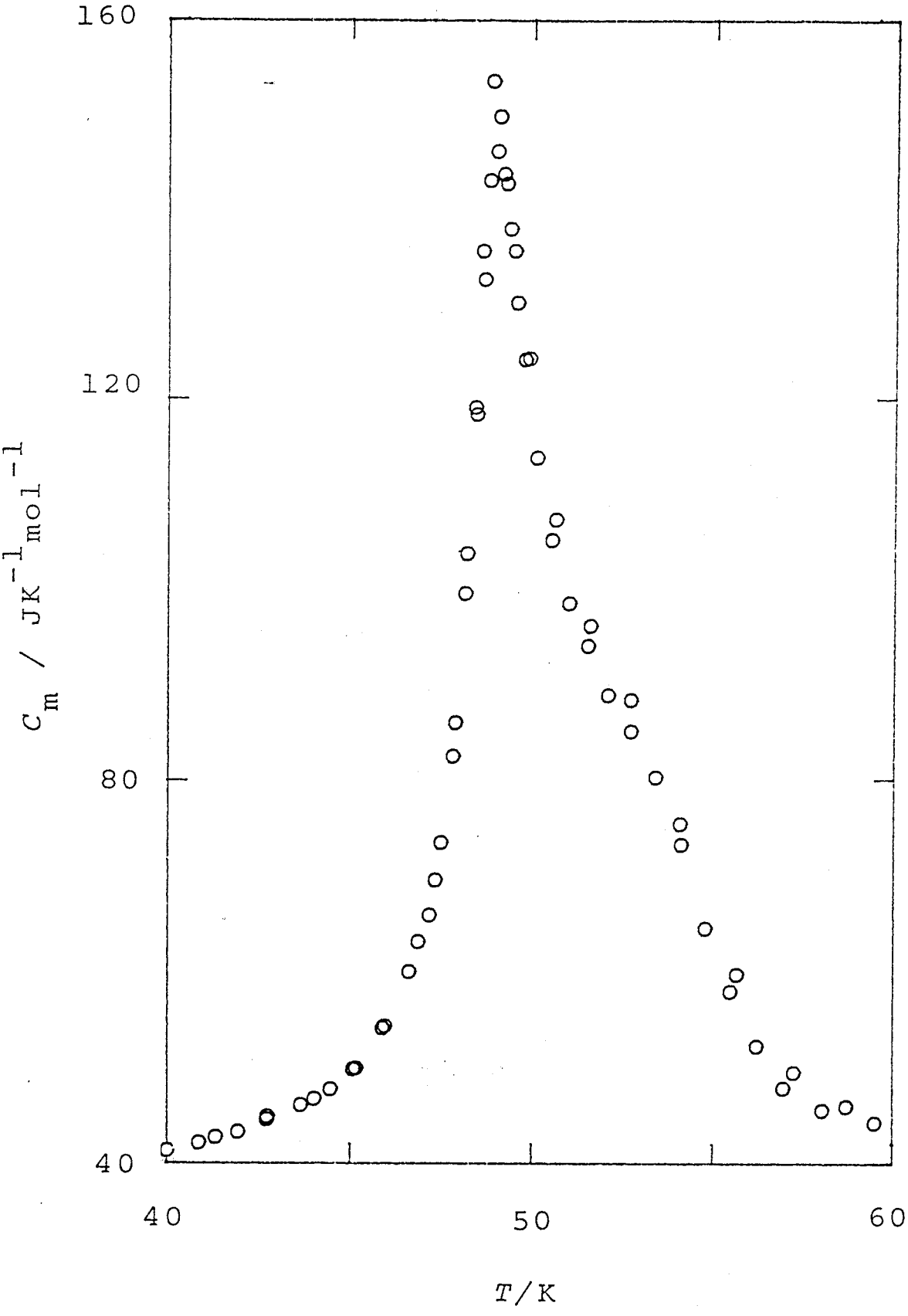

Fig. IV-2(b) Molar heat capacity of CO and N_2 1:1 mixture on graphite (melting region).

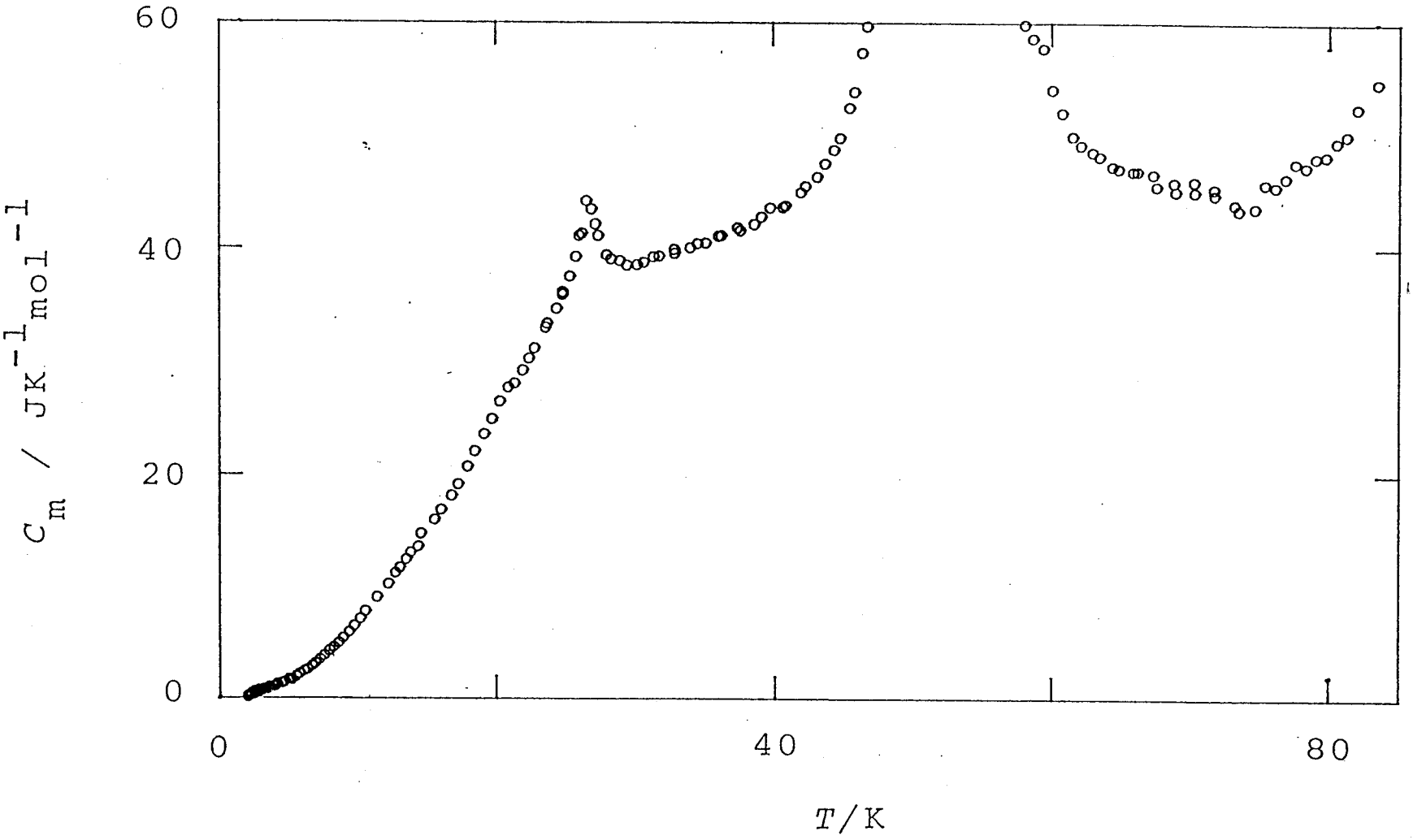

Fig. IV-3(a) Molar heat capacity of CO and N_2 1:2 mixture on graphite.

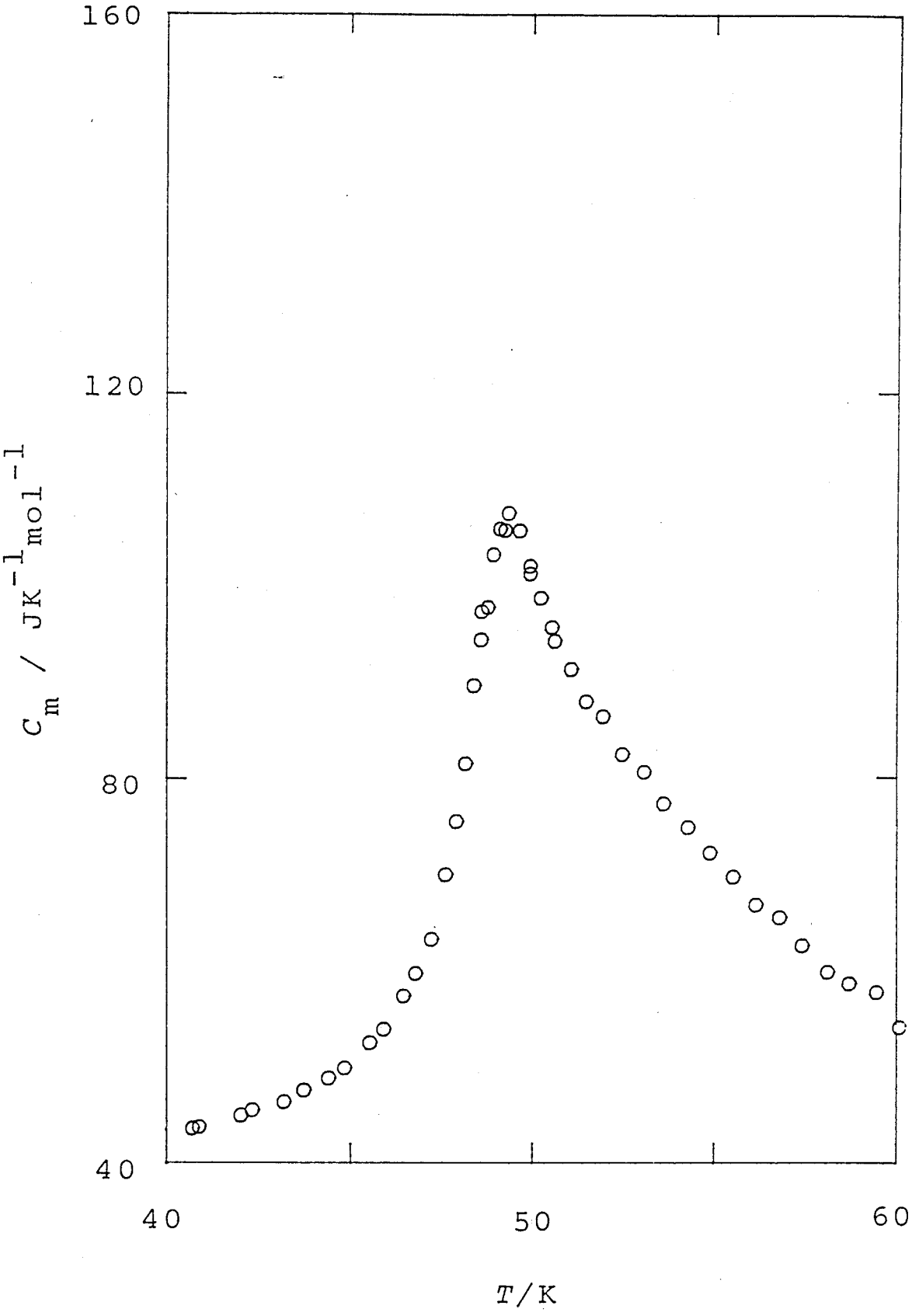

Fig. IV-3(b) Molar heat capacity of CO and N_2 1:2 mixture on graphite (melting region).

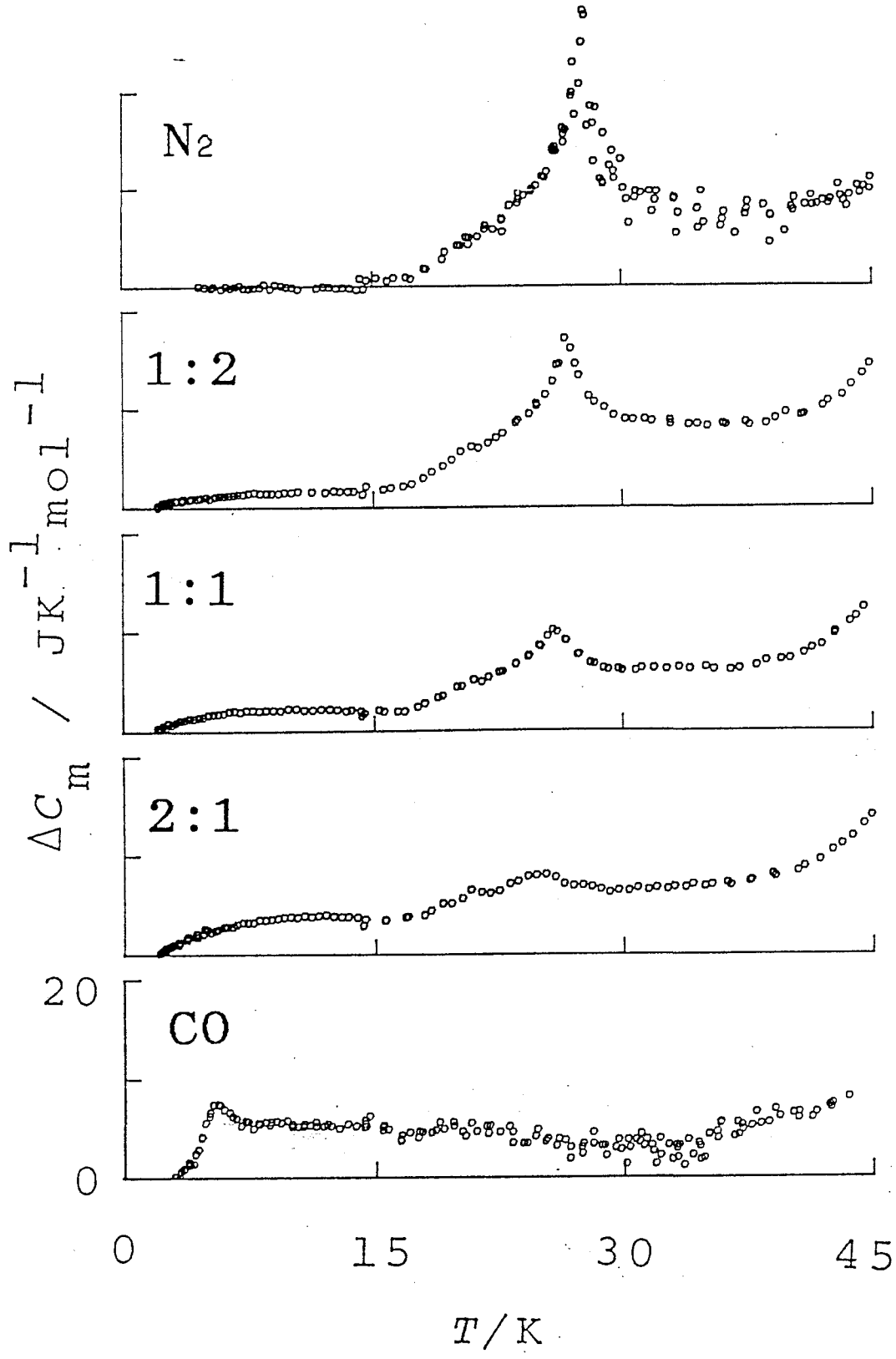

Fig. IV-4 Excess heat capacities of the pure CO, pure N_2 and the mixtures on graphite around the transition region.

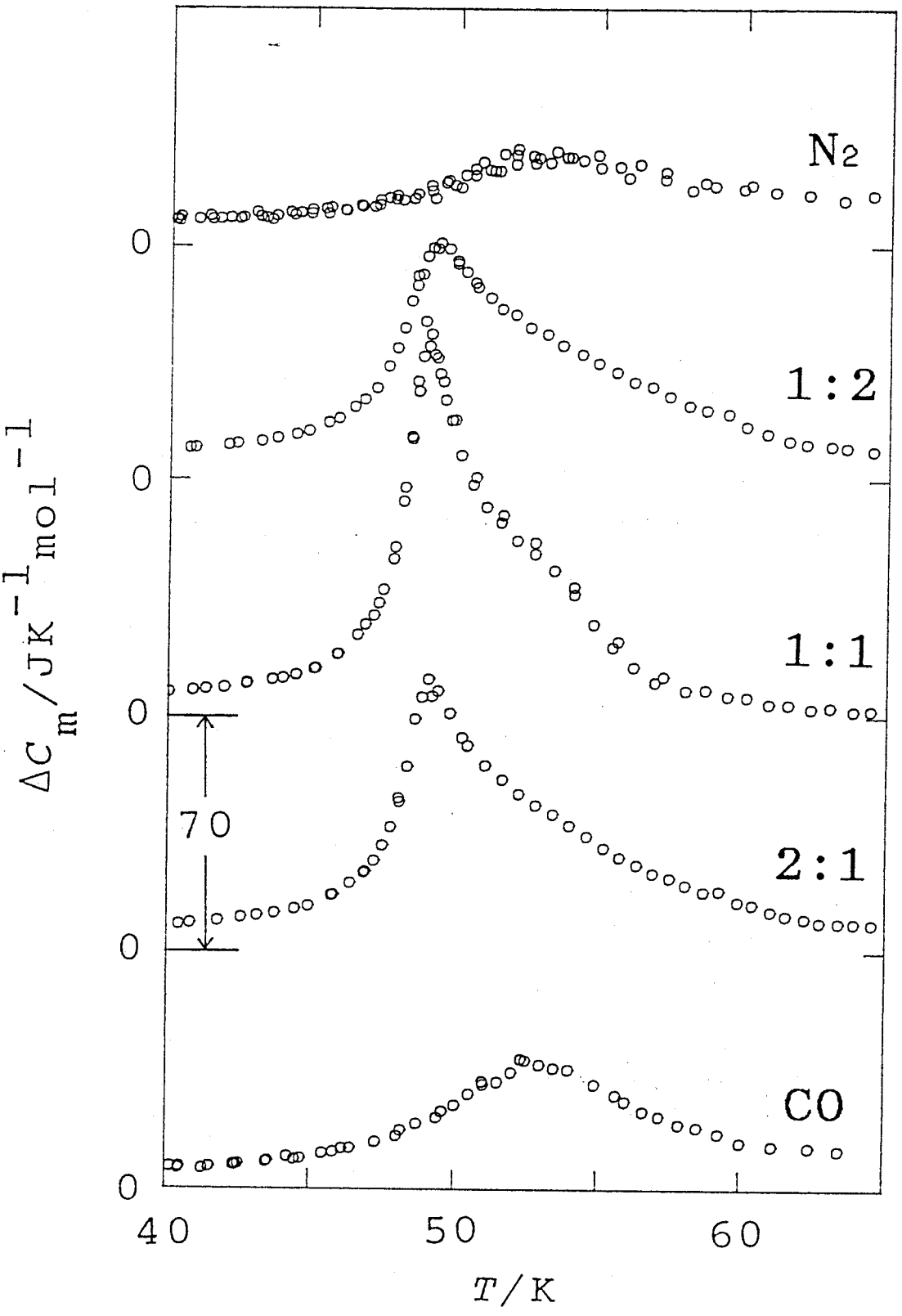

Fig. IV-5 Excess heat capacities of the pure CO, pure N_2 and the mixtures on graphite around the melting region.

miscible at least partly. The broad anomaly around 19 K for the pure CO is associated with the orientational order-disorder transition with respect to the molecular-axis (refs. 7 and 11). As the system is diluted with N_2, the transition becomes sharp and the transition temperature approaches to that for the pure N_2. The fact again indicates that CO and N_2 are miscible on the surface of graphite.

In the melting region (Fig. IV-5), there is a rather broad anomaly both for the pure CO and N_2 around 53 K. For the mixtures, on the other hand, it was found that there is a large anomaly at 49 K followed by a shoulder at the high temperature side. This behavior cannot be interpreted by the existence of a eutectic halt, but may be explained by the "incipient triple point" model (refs. 13 and 14).

For most of the adsorbed systems, the critical point is situated below the triple point as illustrated in Fig. IV-6(a), which is easy to understand. The melting is accompanied by a thermal anomaly. Some of the systems, however, show a peculiar phase diagram (Fig. IV-6(b)). The triple point is never realized. Instead, we have an "incipient triple point", where only a broad thermal anomaly may be seen under the requirement of the lever rule. This is the case of N_2, CO and Kr on graphite. A brief explanation of this phenomenon in terms of the Gibbs energy is given in Fig. IV-7. As a consequence, the prominent peak observed at 49 K for the mixtures should not be due to the melting.

IV-3-3 Third-Law Entropy

The molar entropies calculated at 80 K for all the samples including their pure components are plotted in Fig. IV-8. The solid line indicates the presumed molar entropy for the ideal solution. Since both the pure CO and N_2 have no residual entropy (refs. 11 and 15), if the mixture has a configurational long-range-order at 0 K, whatever it is, the system may have no residual entropy. While the mixtures [2:1] and [1:2] seem to follow the third law of thermodynamics, the mixture [1:1] may have some residual entropy. In order to explain such situation

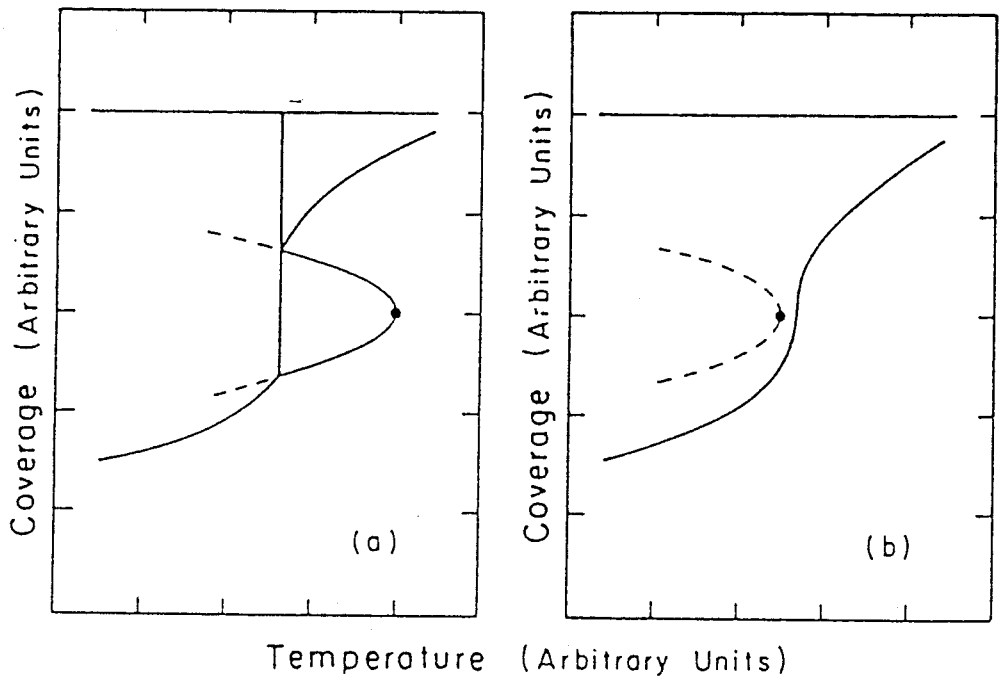

Fig. IV-6 Schematic phase diagrams indicating (a) triple point and (b) incipient triple point. The broken curves show the metastable boundary separating the liquid and vapor phases (ref. 13).

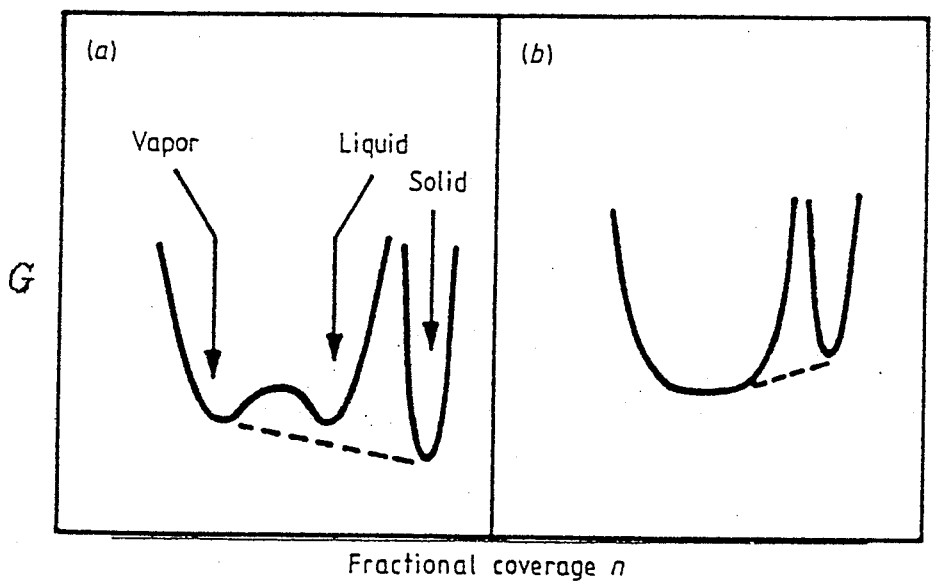

Fig. IV-7 Schematic Gibbs energy G as a function of coverage for the incipient triple point mechanism. At low temperatures (a), the liquid cannot exist as a stable phase because the vapor-solid double tangent always lies beneath the Gibbs energy of the liquid. At temperatures above the vapor-liquid critical point (b), a fluid phase can coexist with the solid (ref. 14).

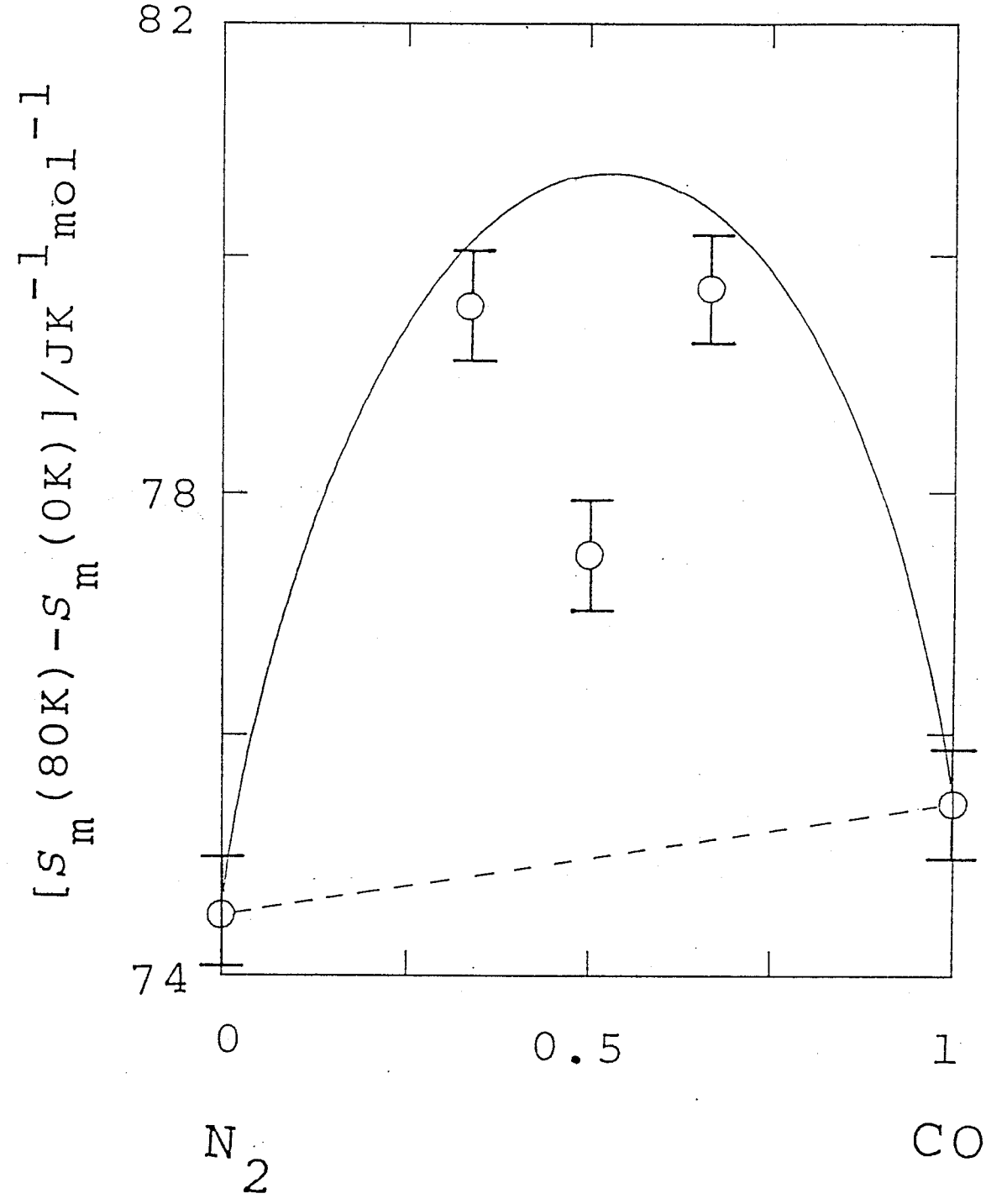

Fig. IV-8 Molar entropy of binary system CO/N_2 determined at 80 K: The dashed line expresses the mean value of those for pure components, and the solid curve is the sum of the mean value and the mixing entropy.

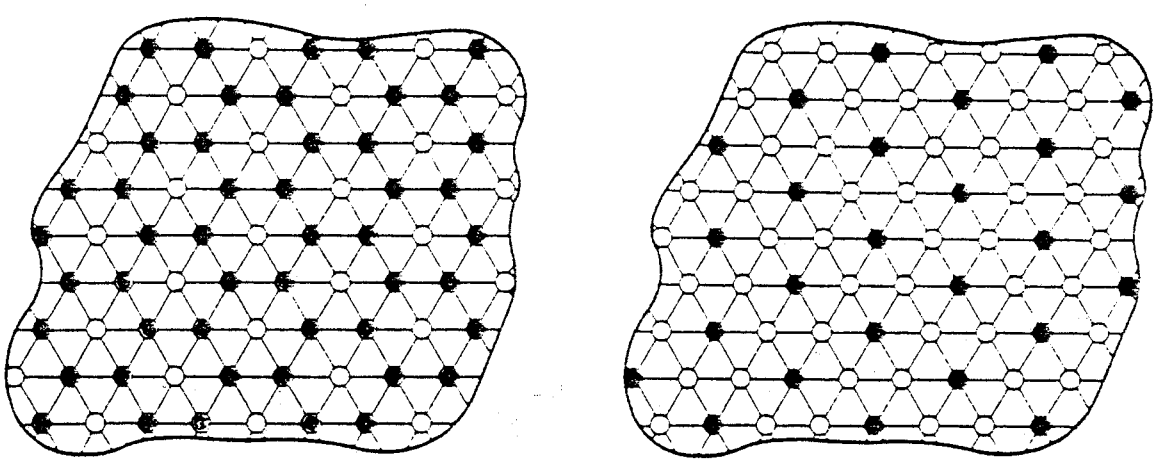

Fig. IV-9 Supposed structures for the mixtures [1:2] and [2:1]. Mark o represents CO and ● N_2 molecules, respectively.

from a structual point of view, the triangular Ising model was applied.

A coupling constant J in this model is defined as

$$2J = 2E[CO\text{-}N_2] - E[CO\text{-}CO] - E[N_2\text{-}N_2], \qquad (IV\text{-}1)$$

where $E[CO\text{-}N_2]$, $E[CO\text{-}CO]$ and $E[N_2\text{-}N_2]$ represent the $CO\text{-}N_2$, CO-CO and $N_2\text{-}N_2$ pair interaction energies, respectively. If $J > 0$, the mixture is forced to a phase separation. Therefore, $J < 0$ is necessary for the present system. This means that the system forms a triangular antiferromagnetic Ising lattice named Wannier lattice (ref. 16), in which frustration plays an essential role in determining the ground state structure. The model tells us that the mixtures [2:1] and [1:2] are completely long-range-ordered and form a ferrimagnetic phases, as illustrated in Fig. IV-9. In contrast, the mixture [1:1] has the residual entropy of $0.3383R$ (= 2.81 $JK^{-1}mol^{-1}$), which is close to the experimental value (3.2 $JK^{-1}mol^{-1}$). Some diffraction experiment may prove this argument.

References to Chapter IV

1. H. You, S.C. Fain, Jr., S. Satija and L. passell, *Phys. Rev. Lett.* 56, 244 (1986).
2. H. You and S.C. Fain, Jr., *Phys. Rev.* B34, 2840 (1986).
3. C.S. Barrett and L. Meyer, *J. Chem. Phys.* 43, 3502 (1965).
4. C.S. Barrett and L. Meyer, *J. Chem. Phys.* 42, 107 (1965).
5. M.J. Angwin and J. Wasserman, *J. Chem. Phys.* 44, 417 (1966).
6. J.A. Morrison, D.M.T. Newsham and R.D. Weir, *Trans. Faraday. Soc.* 64, 1461 (1968).
7. K. Morishige, C. Mowforth and R.K. Thomas, *Surf. Sci.* 151, 289 (1985).
8. H. You and S.C. Fain, Jr., *Surf. Sci.* 151, 361 (1985).
9. A. Inaba, T. Shirakami and H. Chihara, *Chem. Phys. Lett.* 146, 63 (1988).
10. T. Atake, H. Suga and H. Chihara, *Chem. Lett.* 567 (1976).
11. A. Inaba, T. Shirakami and H. Chihara, *J. Chem. Thermodyn.*

23, 461 (1991).
12. J.C. Burford and G.M. Graham, *Can. J. Phys.* 47, 23 (1969).
13. D.M. Butler, J.A. Litzinger, G.A. Stewart and R.B. Griffiths, *Phys. Rev. Lett.* 42, 1289 (1979).
14. A.D. Migome, M.H.W. Chan, K.J. Niskanen and R.B. Griffiths, *J. Phys.* C: *Solid State Phys.* 16, L1115 (1983).
15. A. Inaba and H. Chihara, *Can. J. Phys.* 66, 703 (1988).
16. G.H. Wannier, *Phys. Rev.* 79, 357 (1950).

Chapter V Methanes on Graphite Part I
Phase Transition and Rotational Tunneling

V-1 Introduction

Solid methane (CH_4) and isotopic methanes ($CH_{4-n}D_n$, n = 1-4) have attracted much interest in many aspects (ref. 1). The rotational state has long been investigated as one of the issues to be solved, which is so-called "methane problem". CH_4 has two solid phases, whereas the other isotopic methanes have three phases. The structure of the phase II of solid CD_4 was originally predicted by James and Keenan through the calculation of the molecular octopole-octopole interactions (ref. 2). Later, it was verified by a neutron diffraction study (ref. 3). The sublattice structure is illustrated in Fig. V-1. It has 6 ordered molecules located at the site with a point symmetry of D_{2d} and 2 disordered molecules at the site of O_h. Because of the tunneling motion, the rotational ground state is split into three, named A, T and E states (refs. 4 and 5) for the ordered molecules.

Methane adsorbed on graphite forms a $\sqrt{3}\times\sqrt{3}$ commensurate structure at low coverages (refs. 6 and 7). The molecules sit on the surface in a tripod configuration (ref. 8, Fig. V-2). As the coverage approaches to the monolayer completion, a compressed incommensurate phase with a triangular structure appears. Above 48 K, this phase transforms surprisingly into another incommensurate phase which has an expanded structure (refs. 9 and 10). In the commensurate phase, all the methane molecules sit on a site of C_{3v} symmetry (ref. 11). In this case, the rotational ground state is split into four (A, T_1, $T_{2,3}$ and E, respectively, as given in Fig. V-3). Namely the T-state is split further into two because of the low symmetry.

We first investigate the phase transitions. According to an NMR study, CH_4 molecules rotate almost isotropically just below the melting point (ref. 10). On the other hand, the observation of the tunneling tells us that the molecules are orientationally ordered at sufficiently low temperatures. However, an a.c.

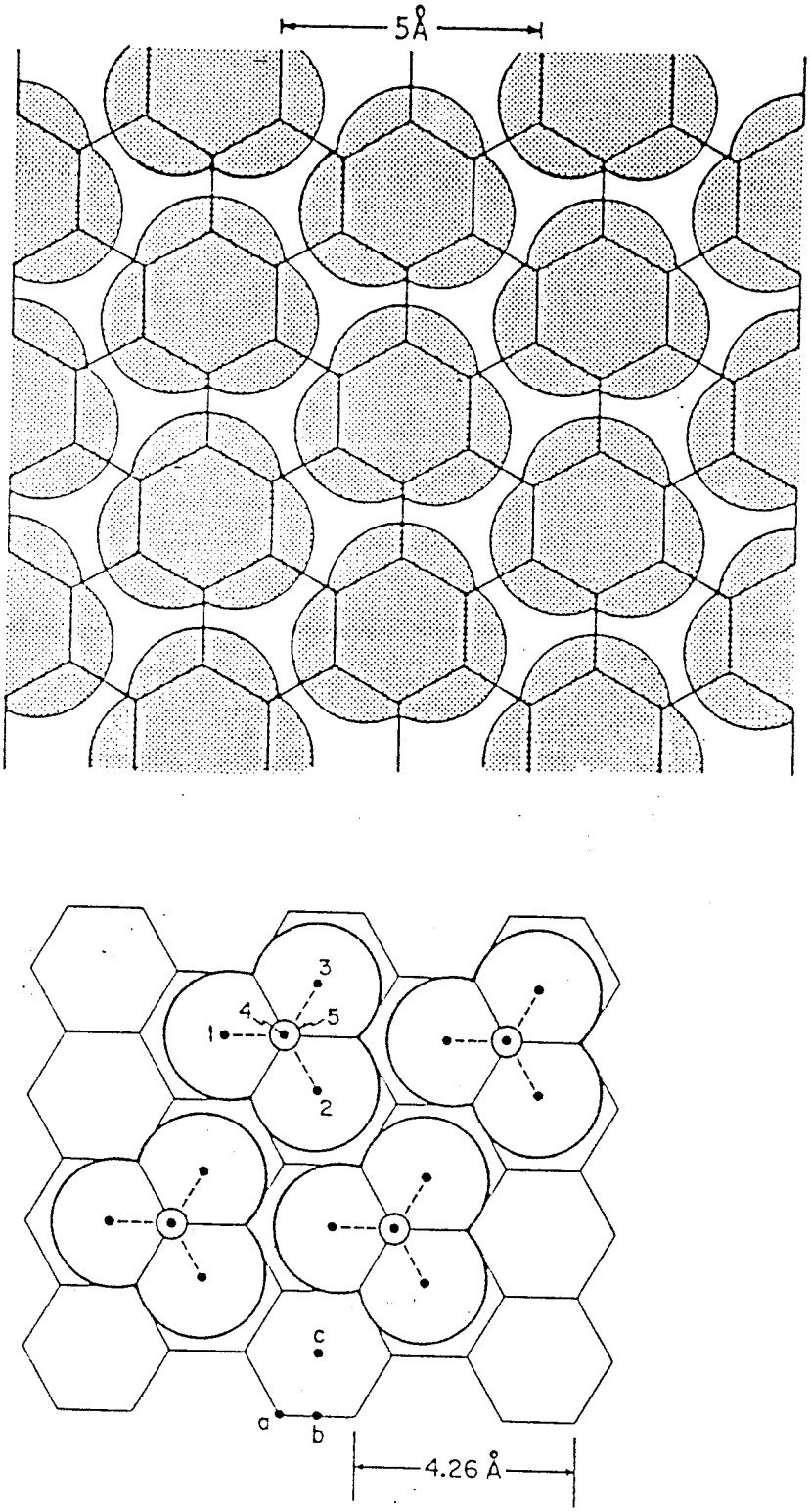

Fig. V-2 Structure of CH_4 commensurate monolayer on graphite. The structure which has site symmetry C_{3v} is either a graphite hexagon center site structure (above) or a carbon atom atop site structure (below). The remaining hydrogen atom is pointing upward in both structures.

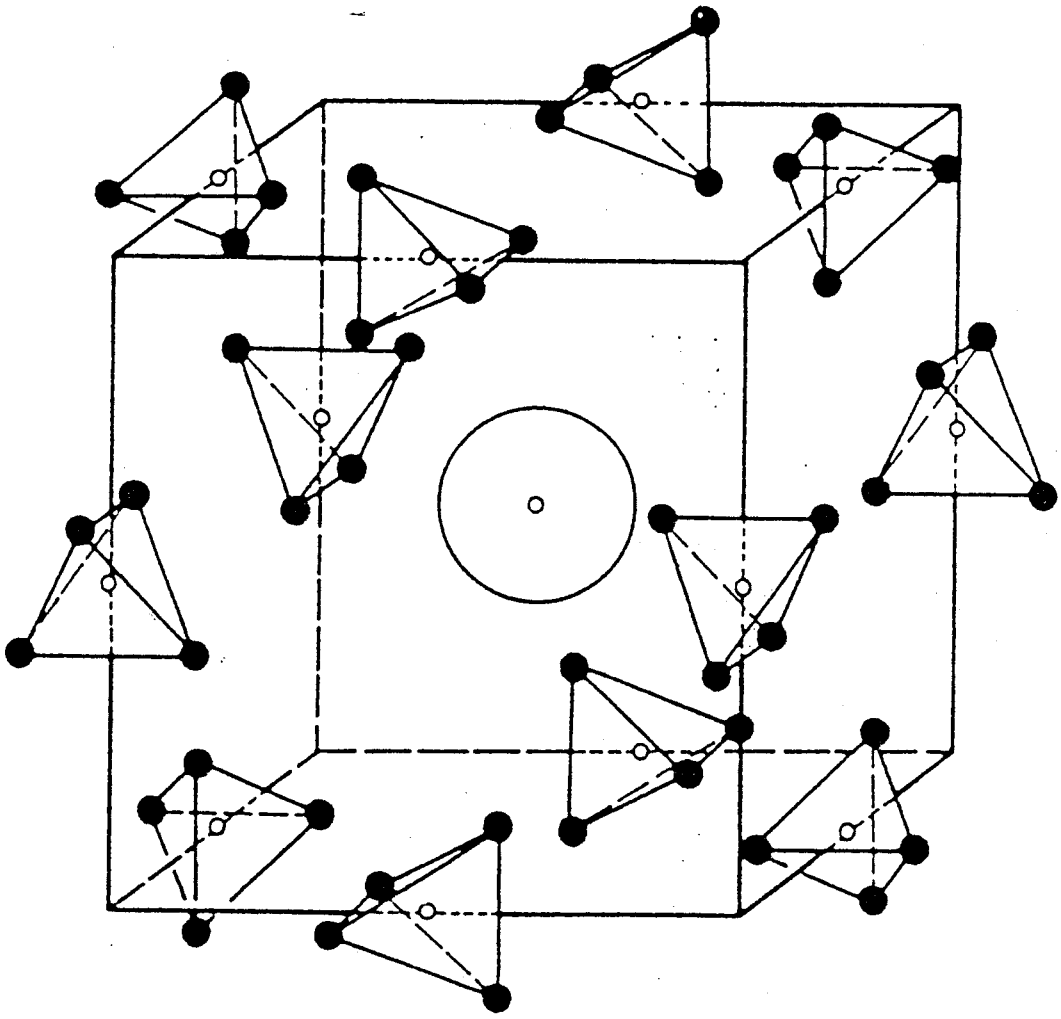

Fig. V-1 Structure of the lowest phase of CH_4 (space group Fm3c). There are 6 sublattices with orientationally ordered molecules (site symmetry D_{2d}) and orientationally disordered molecules (site symmetry O_h) (ref. 3).

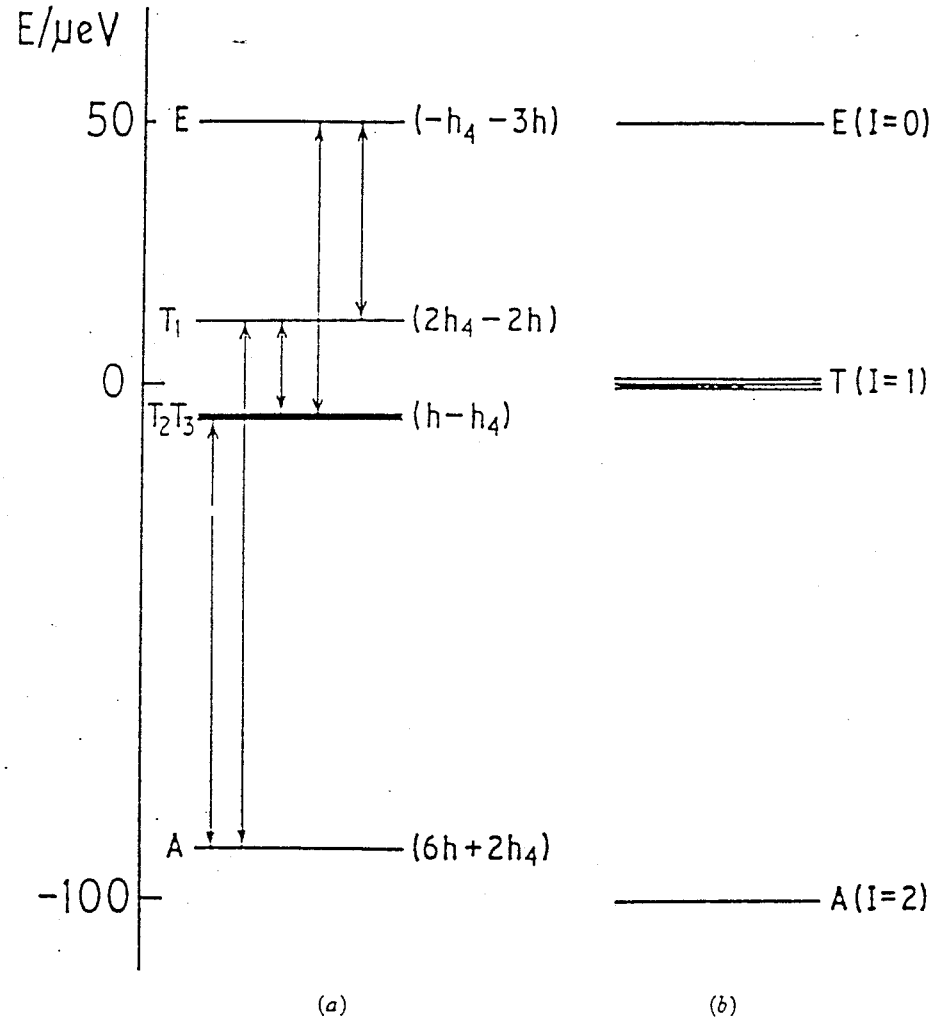

Fig. V-3 Rotational tunneling levels for CH_4, (a) on the graphite surface, and (b) in a tetrahedral symmetry (ref. 8).

Table V-1 Energies of tunneling transitions of methane adsorbed on graphite (ref. 8).

Assignment	Observed energy/μeV	Calculated energy
$T_1 \leftrightarrow (T_2+T_3)$	17 ± 1	18
$T_1 \leftrightarrow E$	39 ± 2	38
$(T_2+T_3) \leftrightarrow E$	56 ± 2	56
$A \leftrightarrow (T_2+T_3)$	94 ± 2	94
$A \leftrightarrow T_1$	112 ± 2	112

calorimetric study for both of CH_4 and CD_4 (ref. 12) could not find any anomaly associated with the rotational transition. The anomaly might be very small or broad, if any.

The second objective here is the investigation of the tunnel splitting. Neutron inelastic scattering studies (refs. 13 and 14) worked out the rotational tunneling transitions for the CH_4 commensurate phase (Fig. V-3, Table V-1). It is interesting to see how it can be confirmed by calorimetry. In the compressed incommensurate phase, the tunneling spectrum became weaker and broader (ref. 15). The heat capacity may determine the averaged effect.

The last objective is the investigation of the lattice property of CD_4 monolayer. The zone-center gap of the CD_4 commensurate phase has been determined by a neutron scattering study (ref. 16). Since the tunnel splitting in the CD_4 monolayer is expected to be very small, the heat capacity at low temperatures may determine the cut-off at the low-frequency end of the phonon density of states.

V-2 Experimental Details

Two calorimeter assemblies were employed for the heat capacity measurement; an adiabatic calorimeter installed in a helium-4 cryostat and an isoperibol calorimeter installed in a helium-3 cryostat, both of which have been described in the previous chapters.

CH_4 gas of research grade (99.99 %) was purchased from Takachiho Kagaku, and CD_4 gas of research grade (99.9 atom % D) was obtained from MSD ISOTOPES. Both gases were used after fractional distillation. The actual amount of CH_4 introduced was 1.57 mmol for the adiabatic calorimeter and 0.886, 0.969, 1.05 and 1.14 mmol for the isoperibol calorimeter, respectively. The former three correspond to the commensurate coverage and the last to the incommensurate coverage. For CD_4, the amount introduced, was 1.57 mmol for the adiabatic calorimeter and 0.968 and 1.15 mmol for the isoperibol calorimeter, respectively. The former two correspond to the commensurate coverage and the last to the incommensurate coverage.

V-3 Results and Discussion

V-3-1 Heat Capacity

The molar heat capacities of CH_4 obtained between 2 and 100 K for n_s = 1.57 mmol and those between 0.7 and 7 K for n_s = 0.886, 0.969, 1.05 and 1.14 mmol are tabulated in Tables V-2, V-3, V-4, V-5 and V-6, respectively. They are also drawn in Figs. V-4, V-5, V-6, V-7 and V-8, respectively. The molar heat capacities of CD_4 obtained for n_s = 1.57 mmol between 2 and 100 K and those for n_s = 0.968 and 1.15 mmol between 0.7 and 7 K and are tabulated in Tables V-7, V-8 and V-9, respectively. They are plotted in Figs. V-9, V-10 and V-11, respectively.

V-3-2 Melting and Commensurate-Incommensurate Transition

The melting point of the CH_4 monolayer (57.5 K) was found to be higher than that for the CD_4 (55.0 K). There is another prominent peak below the melting point for both CH_4 and CD_4 (Fig. V-4 and V-9), which corresponds to the commensurate-incommensurate phase transition (refs. 7, 9 and 12). The transition temperature was 43.4 K for CH_4 and 47.8 K for CD_4. Such isotope effect has already been reported by Kim, *et al.* (ref. 12), but in different temperatures; 47.0 K for CH_4 and 48.5 K for CD_4 (ref. 12).

V-3-3 Rotational Phase Transition and Rotational States

As already described in the previous chapters, the lattice heat capacity of the adsorbed monolayer solid is expressed with three characteristic temperatures, *i.e.* Θ_C, Θ_D and Θ_E. The Θ_C and Θ_D, which were obtained from the fitting the model function to the heat capacities for the samples of the coverage 1.57 mmol, are 8 K and 110 K for CH_4 and 8 K and 83 K for CD_4, respectively. The Θ_E for the vibrational motions perpendicular to the surface was estimated to be 138 K for CH_4 from an inelastic neutron scattering study (ref. 14). The Θ_E for CD_4

Table V-2 Molar heat capacity of CH_4 commensurate monolayer on graphite for n_s = 1.57 mmol.

T / K	C_m / $JK^{-1}mol^{-1}$	T / K	C_m / $JK^{-1}mol^{-1}$	T / K	C_m / $JK^{-1}mol^{-1}$
14.323	5.61	3.493	0.153	23.343	19.21
15.475	7.83	3.983	0.231	24.520	21.35
16.769	9.49	4.460	0.320	25.708	22.66
18.058	11.27	4.928	0.403	26.873	25.15
19.223	12.97	5.390	0.514	28.045	26.78
20.384	14.96	5.864	0.609	29.216	28.39
21.579	16.56	6.365	0.844	30.358	30.11
22.771	18.40	6.904	0.987	31.415	32.17
23.951	20.32	7.476	1.190	32.394	33.20
25.107	21.97	8.083	1.540	33.324	34.32
26.255	23.70	8.720	1.789	34.343	35.60
27.390	25.58	9.388	2.241	35.358	36.79
28.560	27.23	10.082	2.758	36.294	37.17
29.742	29.19	10.818	3.398	37.192	38.39
30.847	30.77	11.575	3.985	37.989	38.94
31.887	32.37	12.350	4.693	38.723	39.41
32.962	33.86	13.126	5.360	39.622	39.92
33.986	35.29	13.868	6.138	40.577	40.36
34.951	35.97	14.571	6.666	41.415	42.04
35.948	37.05			41.973	43.29
36.837	37.75	2.519	0.088	42.250	45.26
37.621	38.48	2.852	0.110	42.488	47.50
38.446	39.12	3.227	0.125	42.689	55.25
39.329	39.51	3.674	0.172	42.877	62.52
40.290	40.31	4.203	0.278	43.051	73.47
41.220	41.35	5.633	0.583	43.212	78.87
42.084	44.69	6.099	0.757	43.370	76.38
42.953	70.53	6.609	0.891	43.530	67.16
43.607	66.35	7.168	1.086	43.691	61.26
43.973	55.70	8.385	1.630	43.853	57.27
44.266	52.91	9.719	2.489	44.067	54.62
44.567	51.67	10.427	2.974	44.542	51.46
44.864	49.55	11.179	3.705	45.336	48.25
45.162	49.17	11.947	4.394	46.378	45.10
45.516	47.94	12.723	4.984	47.541	44.01
45.960	46.34	13.483	5.611	48.686	43.35
46.444	44.89	14.217	6.553	49.834	43.09
46.988	44.55			50.985	43.69
47.623	44.41	14.955	7.15	52.138	44.14
48.469	43.71	16.132	8.32	52.998	45.80
		17.343	10.23	53.507	46.17
2.141	0.087	18.580	11.76	53.881	47.47
2.356	0.088	19.825	14.88	54.180	47.68
2.678	0.104	21.047	15.75	54.450	48.16
3.051	0.134	22.224	17.26	54.689	49.15

Table V-2 (continued).

T / K	C_m / $JK^{-1}mol^{-1}$	T / K	C_m / $JK^{-1}mol^{-1}$	T / K	C_m / $JK^{-1}mol^{-1}$
54.929	49.80	95.233	46.95	48.181	43.92
55.170	51.55	97.003	49.07	49.285	42.99
55.410	52.24	98.773	51.70	50.398	43.06
55.650	55.99	100.544	50.94	51.548	44.51
55.877	54.94			52.700	45.02
56.083	57.21			53.806	47.75
56.282	60.55			54.655	49.51
56.482	65.64			55.294	51.67
56.678	75.13			55.818	55.56
56.865	91.04			56.131	57.35
57.035	119.78			56.339	61.60
57.174	170.21			56.531	68.82
57.294	220.70			56.698	73.82
57.403	243.01			56.836	86.99
57.503	242.48			56.951	102.66
57.605	224.62			57.054	129.20
57.705	206.22			57.155	164.35
57.805	188.79			57.254	208.35
57.926	176.47			57.353	241.56
58.104	149.77			57.453	242.93
58.385	123.27			57.554	229.12
58.810	78.90			57.671	208.03
59.520	60.74			57.832	185.88
60.564	55.73			58.040	158.98
61.976	50.86			58.326	124.87
63.668	47.80			58.728	81.81
65.401	45.17			59.273	61.70
67.137	43.80			60.084	55.70
68.872	42.33			61.259	52.95
70.615	40.38			62.876	48.93
72.358	39.60			64.684	46.06
74.104	38.77			66.397	44.92
75.855	39.54			68.087	42.60
77.606	39.57			69.780	40.99
79.362	39.90			71.497	40.01
81.120	39.80			73.272	39.13
82.876	41.13			75.051	39.11
84.634	42.22			76.799	38.95
86.396	42.60			78.552	39.73
88.160	42.90			80.309	40.02
89.926	44.35			82.034	41.02
91.696	44.86			83.764	40.83
93.464	46.62			85.526	42.26

Table V-3 Molar heat capacity of CH_4 commensurate monolayer on graphite for n_a = 0.886 mmol.

T / K	C_m / $JK^{-1}mol^{-1}$	T / K	C_m / $JK^{-1}mol^{-1}$	T / K	C_m / $JK^{-1}mol^{-1}$
0.747	0.264	1.427	0.094	1.747	0.081
0.781	0.257	1.622	0.080	1.814	0.074
0.820	0.229	1.810	0.090	1.904	0.075
0.864	0.174	2.007	0.073	2.031	0.059
0.916	0.172	2.216	0.074	2.177	0.069
0.981	0.189	2.432	0.070	2.330	0.098
1.076	0.147	2.669	0.104	2.488	0.078
1.155	0.152	2.939	0.135	2.650	0.110
1.257	0.123	3.205	0.157	2.838	0.103
1.377	0.117	3.479	0.198	3.020	0.121
1.505	0.087	3.765	0.212	3.212	0.133
1.667	0.091	4.059	0.257	3.416	0.148
1.859	0.078	4.358	0.305	3.636	0.163
		4.672	0.378	3.878	0.198
0.725	0.336	5.008	0.428	4.140	0.246
0.760	0.310	5.372	0.526	4.423	0.331
0.801	0.248	5.772	0.645	4.728	0.402
0.849	0.187	6.191	0.804	5.056	0.434
0.903	0.191	6.603	1.062	5.416	0.485
0.974	0.174	7.027	1.149	5.812	0.668
1.066	0.153			6.256	0.864
1.149	0.131			6.769	1.175
1.262	0.099				

Table V-4 Molar heat capacity of CH_4 commensurate monolayer on graphite for n_a = 0.969 mmol.

T / K	C_m / $JK^{-1}mol^{-1}$	T / K	C_m / $JK^{-1}mol^{-1}$	T / K	C_m / $JK^{-1}mol^{-1}$
3.906	0.215	0.751	0.251	0.668	0.273
4.327	0.328	0.781	0.227	0.702	0.246
4.697	0.383	0.812	0.208	0.734	0.233
5.070	0.445	0.846	0.200	0.767	0.251
5.464	0.588	0.732	0.299	0.845	0.197
5.885	0.739	0.763	0.233	0.922	0.125
6.295	0.988	0.794	0.226	1.004	0.147
6.731	1.128	0.827	0.185	1.096	0.107
7.177	1.348	0.884	0.176	1.212	0.095
		0.955	0.146	1.393	0.073
4.467	0.364	1.032	0.146	1.611	0.088
4.803	0.424	1.116	0.128	1.825	0.068
5.195	0.524	1.227	0.067	2.046	0.076
5.614	0.562	1.415	0.080	2.280	0.082
6.131	0.772	1.657	0.075	2.527	0.123
6.644	1.018	1.908	0.085	2.782	0.140
7.057	1.277			3.079	0.165
				3.295	0.147
1.492	0.096			3.677	0.215
1.598	0.101			4.061	0.288
1.752	0.104			4.465	0.402
1.955	0.094			4.904	0.463
2.184	0.106			5.367	0.529
2.445	0.099			5.817	0.693
2.737	0.106			6.233	0.948
3.047	0.128			6.620	1.100
3.364	0.148			7.007	1.128
3.693	0.231				
4.054	0.254				
4.417	0.365				

Table V-5 Molar heat capacity of CH_4 incommensurate monolayer on graphite for n_a = 1.05 mmol.

T / K	C_m / $JK^{-1}mol^{-1}$	T / K	C_m / $JK^{-1}mol^{-1}$	T / K	C_m / $JK^{-1}mol^{-1}$
0.801	0.227	0.779	0.241	1.828	0.143
0.841	0.199	0.815	0.216	1.908	0.126
0.885	0.209	0.855	0.224	2.004	0.139
0.934	0.207	0.902	0.174	2.122	0.153
1.018	0.185	0.959	0.199	2.262	0.148
1.077	0.184	1.050	0.164	2.408	0.162
1.152	0.163	1.118	0.152	2.587	0.163
1.253	0.128	1.200	0.137	2.753	0.185
1.369	0.129	1.300	0.143	2.926	0.186
1.492	0.131	1.411	0.141	3.108	0.205
1.647	0.125	1.528	0.133	3.302	0.228
1.833	0.136	1.671	0.130	3.514	0.240
		1.836	0.148	3.739	0.256
		1.998	0.144	3.981	0.295
		2.156	0.146	4.242	0.328
		2.321	0.151	4.529	0.420
		2.494	0.162	4.844	0.483
		2.675	0.179	5.185	0.579
		2.862	0.182	5.559	0.608
		3.060	0.207	5.973	0.777
		3.272	0.211	6.382	0.961
		3.500	0.254	6.769	1.063
		3.741	0.291		
		3.999	0.316		
		4.275	0.385		
		4.573	0.411		
		4.904	0.505		
		5.266	0.524		
		5.666	0.637		
		6.115	0.808		
		6.589	1.024		
		7.041	1.172		

Table V-6 Molar heat capacity of CH_4 incommensurate monolayer on graphite for n_s = 1.14 mmol.

T / K	C_m / $JK^{-1}mol^{-1}$	T / K	C_m / $JK^{-1}mol^{-1}$	T / K	C_m / $JK^{-1}mol^{-1}$
0.771	0.309	0.760	0.322	1.985	0.158
0.808	0.261	0.799	0.341	2.204	0.166
0.845	0.259	0.843	0.261	2.562	0.196
0.881	0.242	0.889	0.212	2.885	0.196
0.920	0.201	0.945	0.174	3.178	0.220
0.962	0.193	1.037	0.162	3.456	0.221
1.005	0.184	1.116	0.141	3.744	0.262
0.787	0.334	1.217	0.117	4.042	0.329
0.826	0.293	1.387	0.134	4.321	0.393
0.871	0.257	1.607	0.135	4.593	0.447
0.929	0.208	1.824	0.139	4.883	0.448
1.015	0.146	2.053	0.151	5.183	0.523
1.096	0.144	2.296	0.158	5.481	0.640
1.191	0.126	2.561	0.167	5.780	0.731
1.300	0.119	2.838	0.207	6.092	0.817
1.413	0.125	3.116	0.218	6.407	0.949
1.547	0.140	3.469	0.240	6.724	0.983
1.692	0.142	3.818	0.273	7.043	1.143
1.881	0.140	4.157	0.326		
2.089	0.144	4.497	0.421		
		4.859	0.489		
		5.240	0.583		
		5.624	0.606		
		5.998	0.753		
		6.378	0.857		
		6.840	1.083		

Table V-7 Molar heat capacity of CD_4 commensurate monolayer on graphite for n_a = 1.57 mmol.

T / K	C_m / $JK^{-1}mol^{-1}$	T / K	C_m / $JK^{-1}mol^{-1}$	T / K	C_m / $JK^{-1}mol^{-1}$
14.340	8.31	53.989	87.22	85.244	40.87
15.456	10.75	54.157	104.62	86.720	40.99
16.675	12.59	54.323	137.41	88.196	41.93
17.870	14.85	54.472	167.55	89.672	45.65
19.028	16.89	54.612	185.75	91.150	45.25
20.230	19.36	54.747	198.88	92.629	45.27
21.428	21.24	54.875	210.42	94.106	47.94
22.602	23.36	55.004	218.32	95.587	50.38
23.765	25.58	55.135	213.03	97.070	51.94
24.912	27.54	55.264	205.15	98.552	52.85
26.083	29.86	55.395	192.79	100.036	54.32
27.276	32.57	55.527	170.06		
28.450	36.04	55.658	156.02	2.311	0.199
29.570	39.00	55.789	127.78	2.624	0.221
30.492	40.80	55.921	108.37	2.989	0.237
31.243	42.51	56.055	89.61	3.366	0.333
31.997	43.46	56.187	80.71	4.408	0.568
32.753	43.77	56.320	76.42	4.877	0.671
33.524	43.44	56.452	69.51	5.347	0.862
34.298	43.55	56.593	65.09	5.822	1.051
35.055	43.80	56.767	63.70	6.320	1.285
35.842	44.90	56.985	61.04	6.856	1.635
36.666	45.36	57.247	58.50	7.427	1.935
37.583	46.48	57.588	57.44	8.030	2.370
38.561	47.23	58.071	60.43	8.652	2.835
39.607	47.88	58.634	55.94	9.303	3.405
40.801	48.40	59.385	54.70	9.996	4.132
41.944	48.89	60.397	52.47	10.721	4.988
43.034	49.24	61.665	51.79	11.468	5.772
44.155	49.34	63.120	50.11	12.243	6.713
45.061	49.77	64.572	45.16	13.017	7.644
45.835	51.20	66.022	46.30	13.784	8.631
46.643	53.32	67.478	44.40	14.509	9.496
47.417	71.75	68.939	43.12		
48.191	77.00	70.399	43.16	2.228	0.193
48.968	62.37	71.913	41.42	2.489	0.212
49.769	59.21	73.455	41.69	2.804	0.242
50.567	58.71	74.948	41.65	3.615	0.365
51.347	58.68	76.415	40.71	4.130	0.453
52.129	59.50	77.881	41.80	4.625	0.640
52.888	63.52	79.350	40.94	5.094	0.723
53.403	68.51	80.822	40.82	5.573	0.961
53.638	72.58	82.295	40.78	6.060	1.148
53.816	77.08	83.769	41.43	6.576	1.401

Table V-7 (continued).

T / K	C_m / $JK^{-1}mol^{-1}$	T / K	C_m / $JK^{-1}mol^{-1}$	T / K	C_m / $JK^{-1}mol^{-1}$
7.136	1.740	46.087	51.14	72.718	41.72
7.743	2.180	46.386	51.24	74.187	40.78
8.366	2.637	46.681	52.80	75.656	40.16
9.002	3.077	46.977	55.65	77.123	41.10
9.671	3.801	47.274	64.10	78.590	40.80
10.360	4.518	47.559	78.22	80.056	41.10
11.095	5.398	47.818	86.42	81.523	41.52
11.861	6.333	48.061	79.08	82.996	41.41
12.638	7.121	48.289	71.44	84.473	42.63
13.396	8.142	48.501	67.61	85.945	43.03
14.128	9.132	48.708	64.44	87.419	43.55
		48.918	62.99	88.893	44.40
14.835	9.95	49.128	60.16	90.367	45.96
15.979	11.59	49.451	59.61	91.843	47.22
17.274	13.65	50.108	58.80	93.322	48.02
18.500	15.42	50.981	58.76	94.802	49.17
19.471	18.08	51.834	59.12	96.281	50.77
20.782	20.67	52.641	61.92	97.760	51.58
21.975	22.00	53.235	66.55	99.241	54.24
23.209	24.20	53.637	74.02	100.721	59.13
24.327	26.82	54.029	95.38		
25.405	28.25	54.419	152.86		
26.590	30.53	54.782	196.57		
27.794	34.38	55.082	207.35		
28.911	37.38	55.365	190.96		
29.908	40.32	55.626	156.05		
30.786	41.50	55.848	116.92		
31.571	43.38	56.054	91.62		
32.309	43.80	56.368	71.99		
33.069	43.80	56.785	61.28		
33.826	43.43	57.195	58.02		
34.602	43.80	57.607	57.46		
35.426	44.54	58.004	55.84		
36.278	45.12	58.402	53.31		
37.130	46.29	59.015	53.13		
38.003	46.56	59.773	51.09		
38.904	47.38	60.460	51.01		
39.901	48.15	61.150	51.07		
41.180	48.47	61.841	49.67		
42.531	49.36	62.531	48.62		
43.712	49.18	63.694	48.49		
44.441	49.15	65.269	46.12		
44.775	49.98	66.799	44.03		
45.121	49.81	68.326	43.90		
45.469	49.87	69.807	41.45		
45.788	51.29	71.261	41.76		

Table V-8 Molar heat capacity of CD_4 commensurate monolayer on graphite for n_s = 0.968 mmol.

T / K	C_m / $JK^{-1}mol^{-1}$	T / K	C_m / $JK^{-1}mol^{-1}$	T / K	C_m / $JK^{-1}mol^{-1}$
0.761	0.033	0.876	0.050	0.755	0.039
0.784	0.051	0.893	0.044	0.780	0.040
0.811	0.051	0.916	0.036	0.808	0.036
0.844	0.056	0.942	0.065	0.842	0.056
0.880	0.081	0.988	0.097	0.885	0.064
0.924	0.091	1.054	0.099	1.017	0.082
0.975	0.095	1.133	0.109	1.111	0.090
1.031	0.093	1.228	0.108	1.247	0.102
1.100	0.106	1.338	0.128	1.461	0.150
1.215	0.107	1.479	0.140	1.718	0.162
1.347	0.127	1.697	0.174	1.971	0.198
1.492	0.137	1.945	0.194		
1.638	0.150	2.184	0.212	0.770	0.053
1.811	0.170	2.434	0.232	0.796	0.043
2.020	0.182	2.731	0.260	0.828	0.059
2.241	0.211	3.019	0.299	0.866	0.068
2.471	0.241	3.315	0.365	0.915	0.082
2.720	0.278	3.628	0.423	0.981	0.115
3.004	0.309	3.958	0.480	1.050	0.108
3.284	0.355	4.312	0.617	1.137	0.114
3.578	0.383	4.684	0.725	1.260	0.109
3.889	0.446	5.068	0.795	1.418	0.143
4.225	0.578	5.471	0.988	1.567	0.153
4.581	0.736	5.884	1.167	1.754	0.165
4.949	0.815	6.314	1.324	1.977	0.200
5.319	0.950	6.776	1.429	2.203	0.220
5.699	1.073	7.236	1.814	2.456	0.230
6.103	1.257			2.706	0.271
6.984	1.612			2.970	0.302
				3.256	0.329
				3.585	0.381
				3.944	0.420
				4.312	0.613
				4.700	0.726
				5.105	0.854
				5.550	1.051
				6.029	1.281
				6.529	1.495
				7.028	1.613

Table V-9 Molar heat capacity of CD_4 incommensurate monolayer on graphite for n_a = 1.15 mmol.

T / K	C_m / $JK^{-1}mol^{-1}$	T / K	C_m / $JK^{-1}mol^{-1}$	T / K	C_m / $JK^{-1}mol^{-1}$
0.731	0.014	0.755	0.024	1.015	0.043
0.752	0.020	0.776	0.029	1.113	0.065
0.777	0.033	0.803	0.038	1.218	0.077
0.809	0.034	0.836	0.050	1.320	0.090
0.937	0.055	0.882	0.053	1.441	0.118
1.013	0.048	0.944	0.045	1.588	0.147
1.107	0.047	1.015	0.075	1.747	0.153
1.231	0.102	1.120	0.056	1.934	0.151
1.389	0.102	1.217	0.084	2.152	0.181
1.551	0.132	1.345	0.112	2.382	0.191
		1.484	0.129	2.641	0.207
		1.620	0.146	2.955	0.220
		1.795	0.156	3.251	0.262
		2.007	0.153	3.537	0.306
		2.260	0.173	3.813	0.318
		2.498	0.206	4.116	0.396
		2.749	0.219	4.544	0.542
		3.014	0.239	5.053	0.634
		3.300	0.260	5.496	0.761
		3.608	0.314	5.898	0.915
		3.947	0.362	6.366	1.032
		4.321	0.447	6.853	1.252
		4.744	0.545	7.324	1.569
		5.206	0.632		
		5.666	0.787		
		6.119	0.920		
		6.591	1.180		
		7.078	1.358		

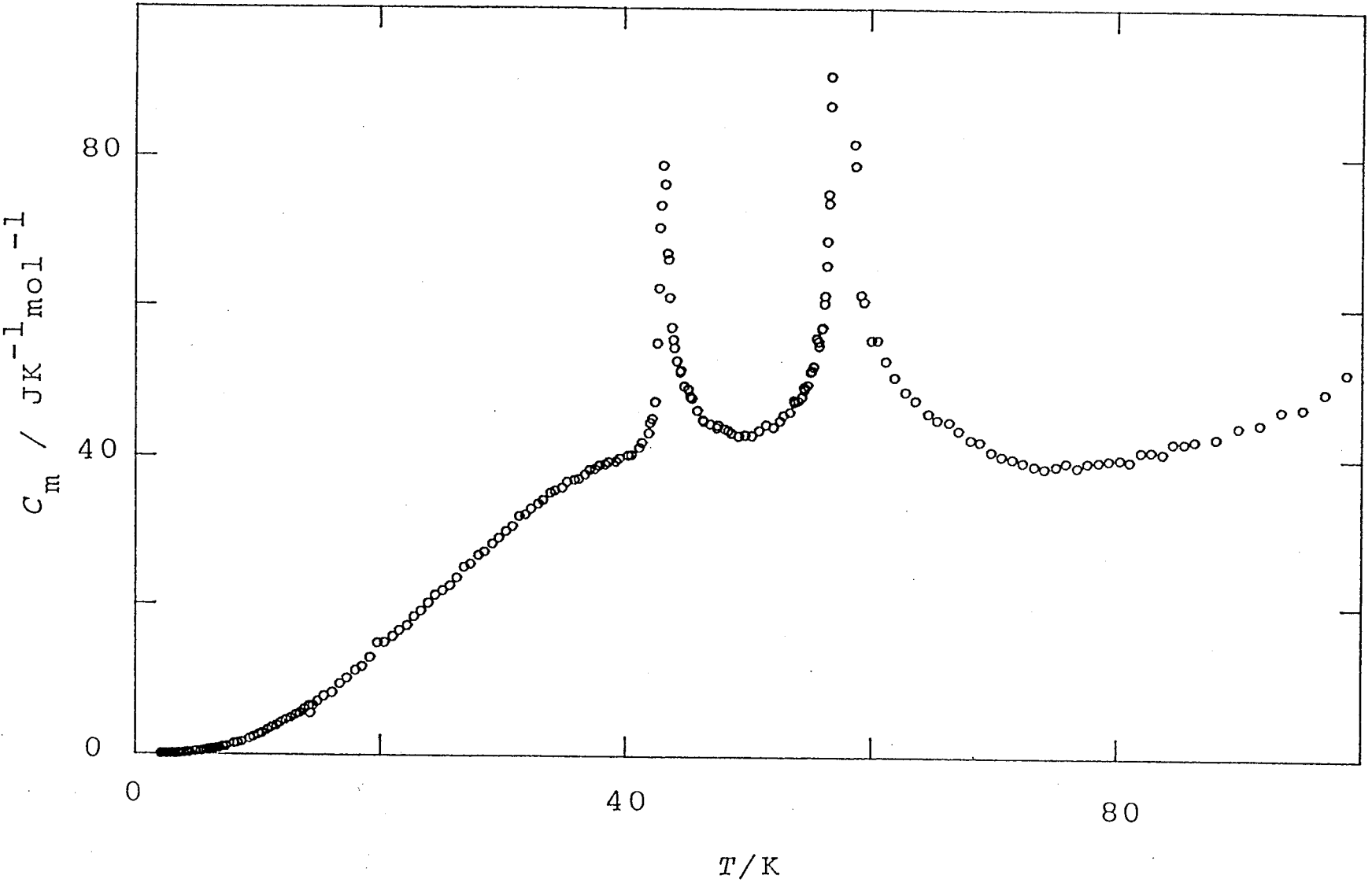

Fig. V-4(a) Molar heat capacity of CH_4 commensurate monolayer on graphite for n_s = 1.57 mmol.

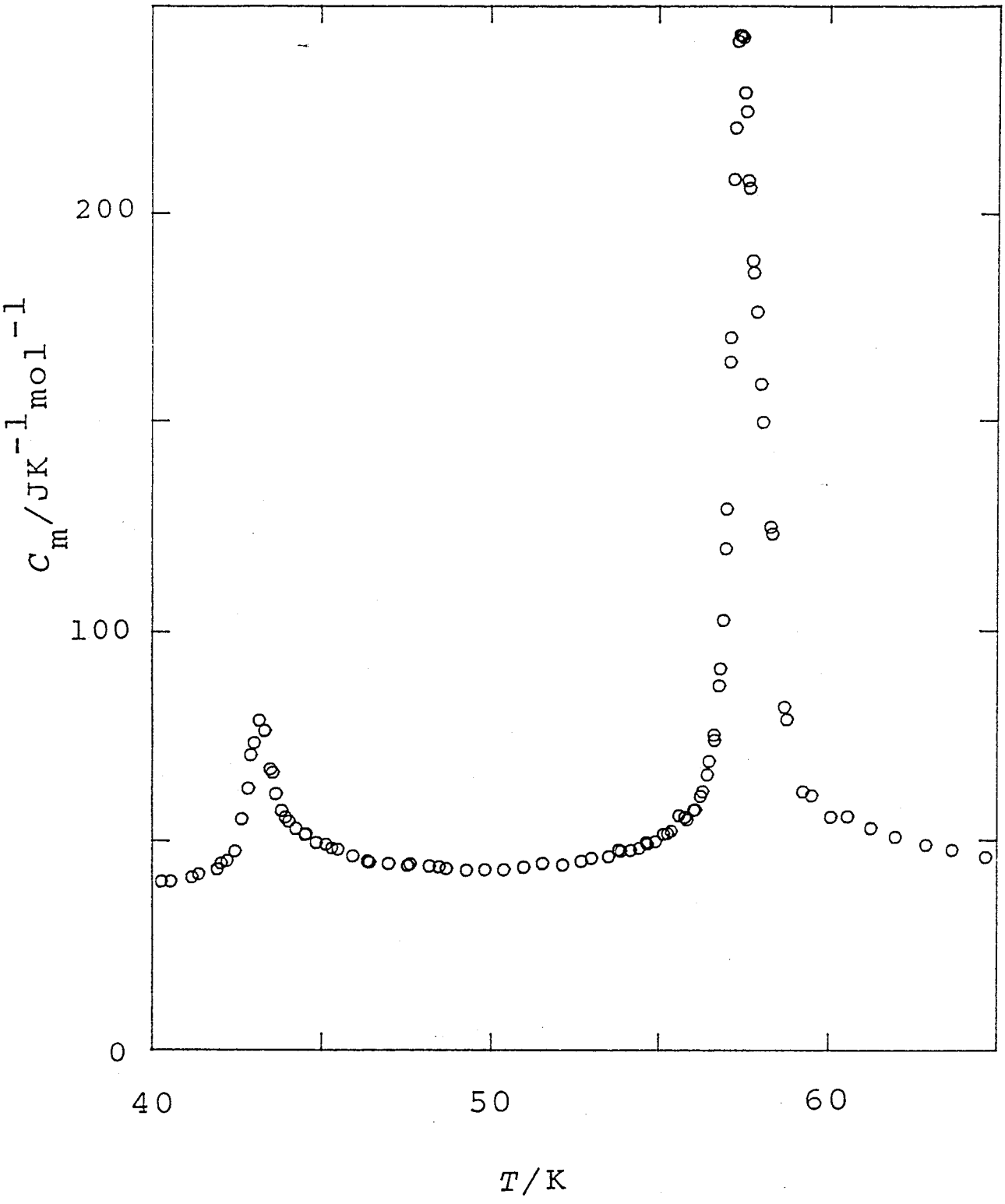

Fig. V-4(b) Molar heat capacity of CH_4 commensurate monolayer on graphite for n_s = 1.57 mmol (melting region).

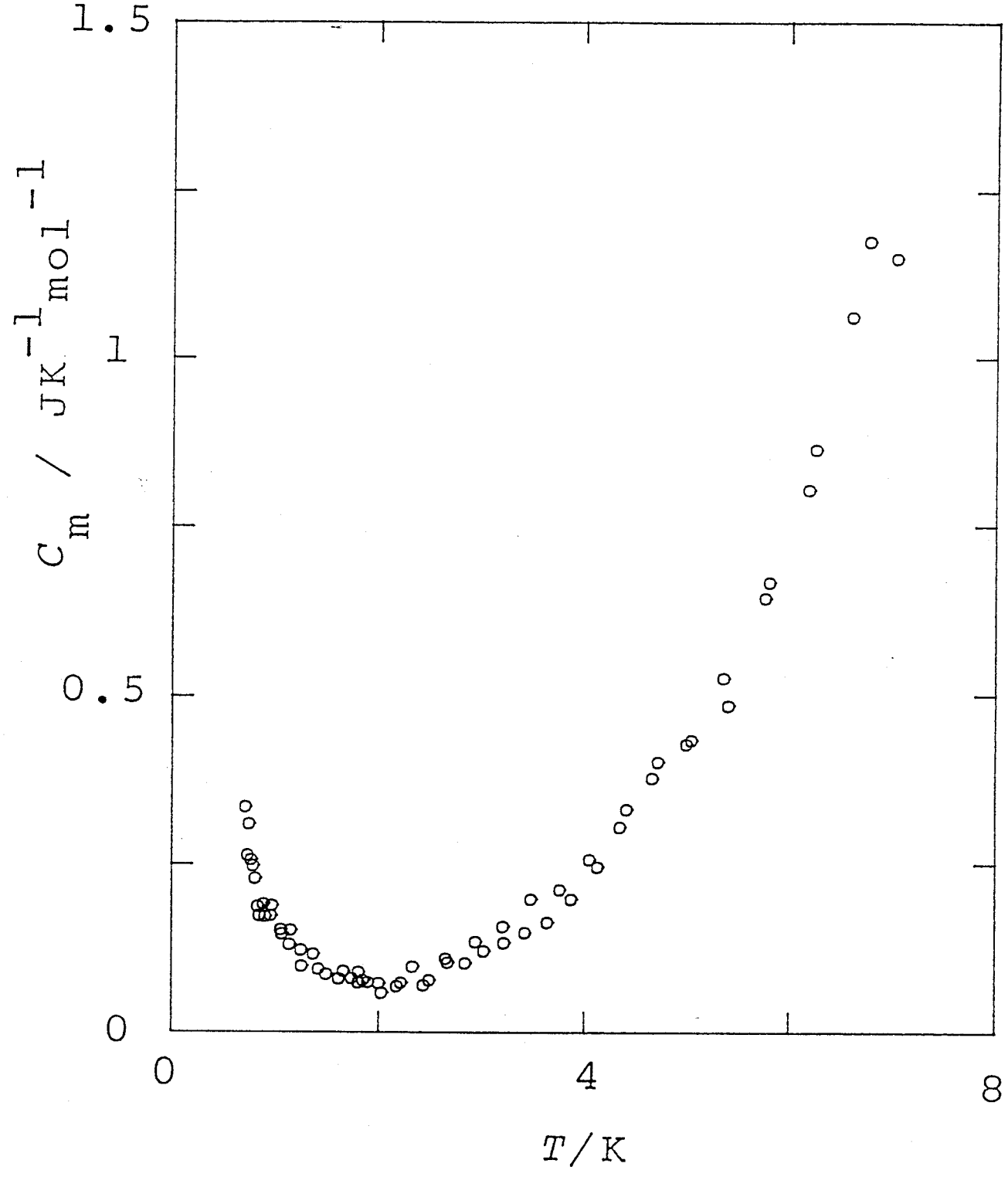

Fig. V-5 Molar heat capacity of CH_4 commensurate monolayer on graphite for n_a = 0.886 mmol.

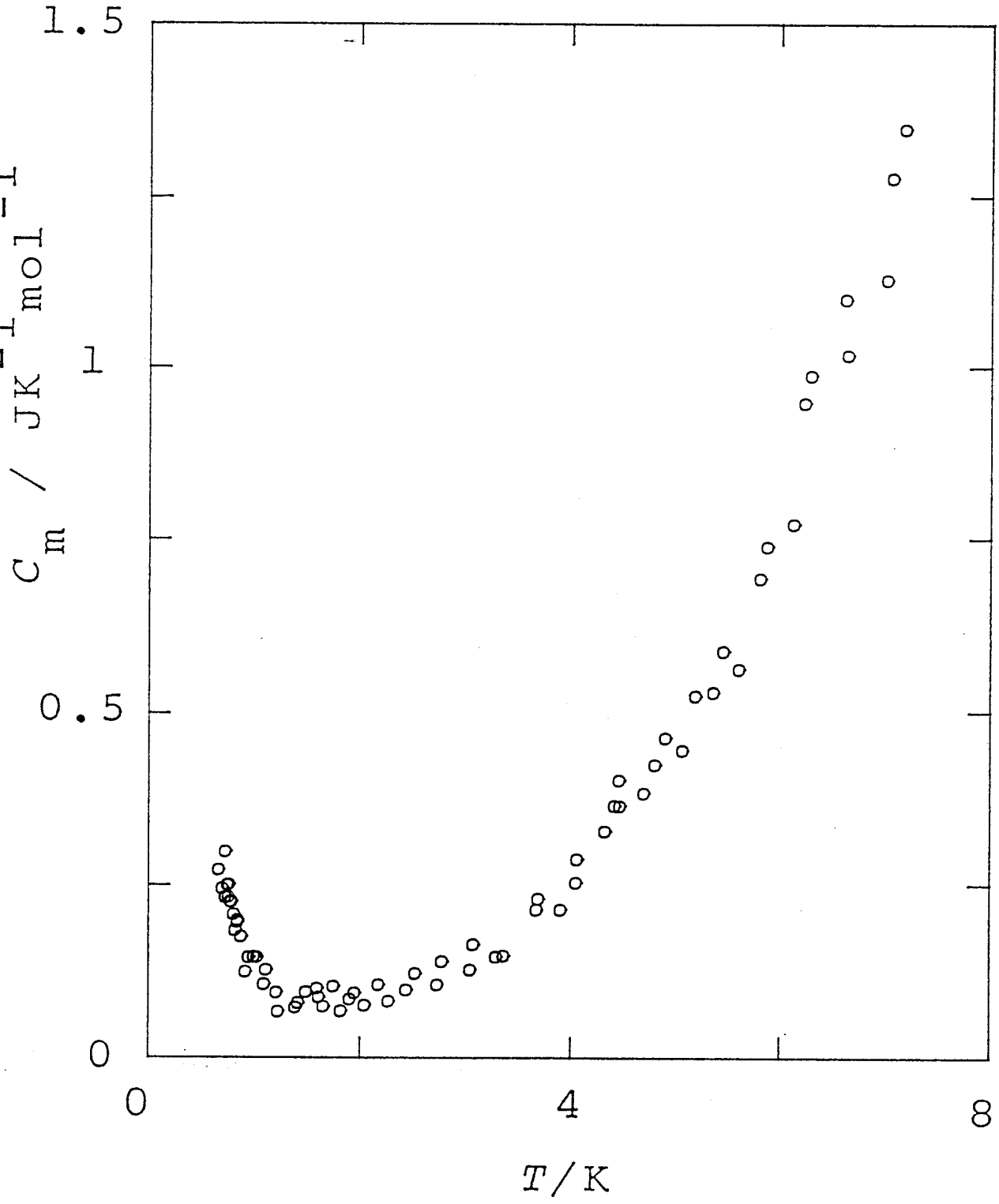

Fig. V-6 Molar heat capacity of CH_4 commensurate monolayer on graphite for n_s = 0.969 mmol.

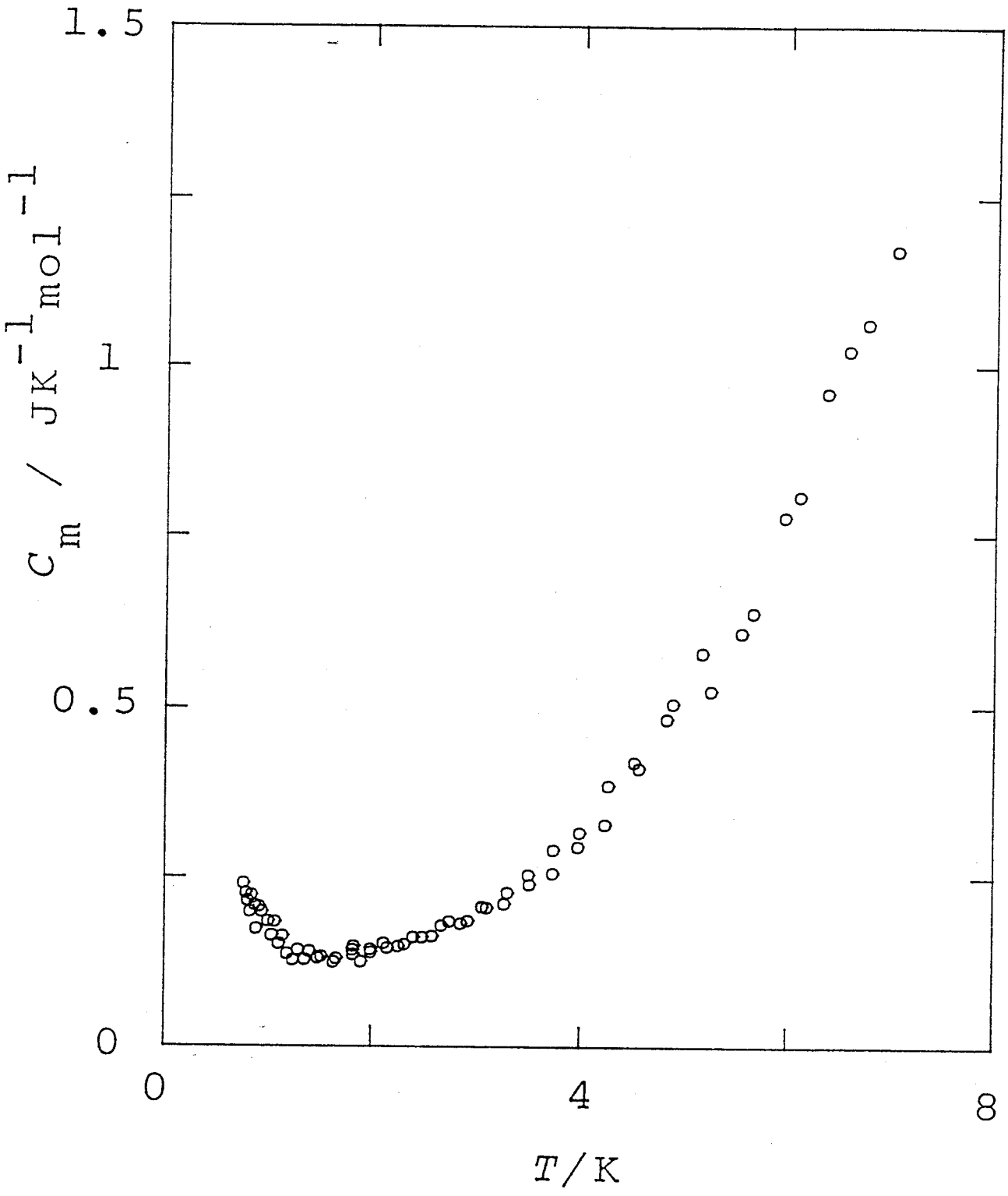

Fig. V-7 Molar heat capacity of CH_4 incommensurate monolayer on graphite for n_s = 1.05 mmol.

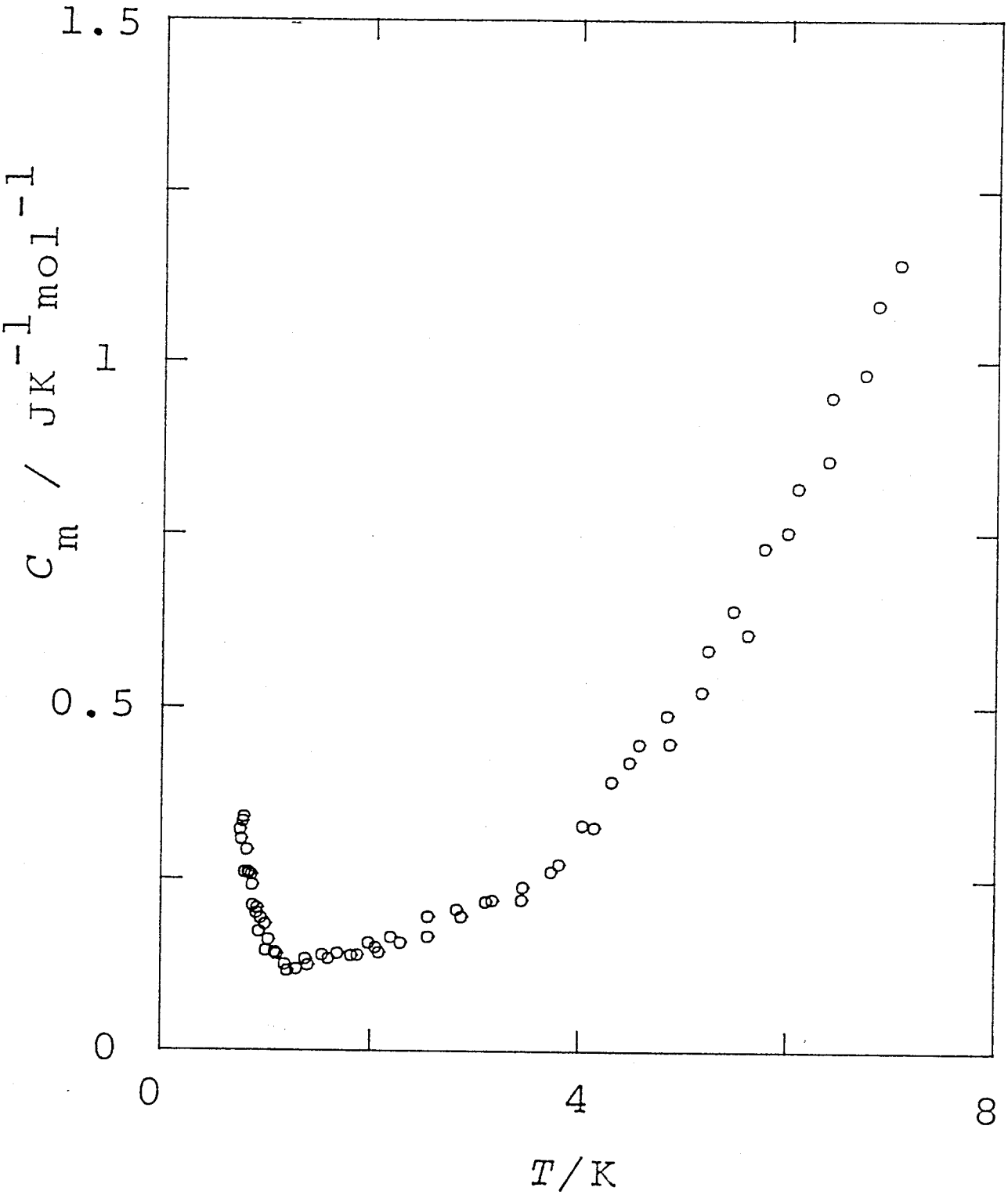

Fig. V-8 Molar heat capacity of CH_4 incommensurate monolayer on graphite for n_s = 1.14 mmol.

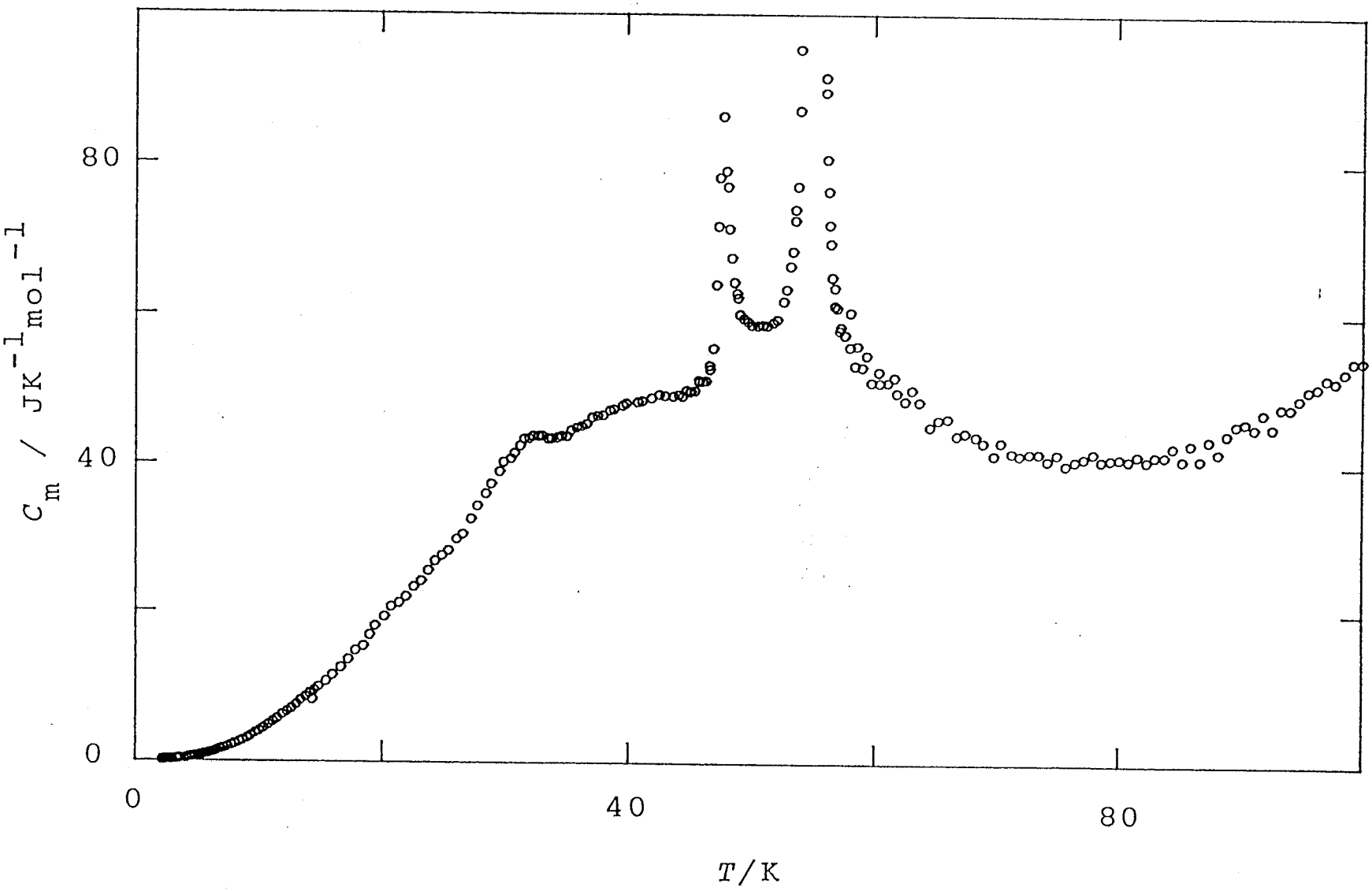

Fig. V-9(a) Molar heat capacity of CD_4 commensurate monolayer on graphite for n_s = 1.57 mmol.

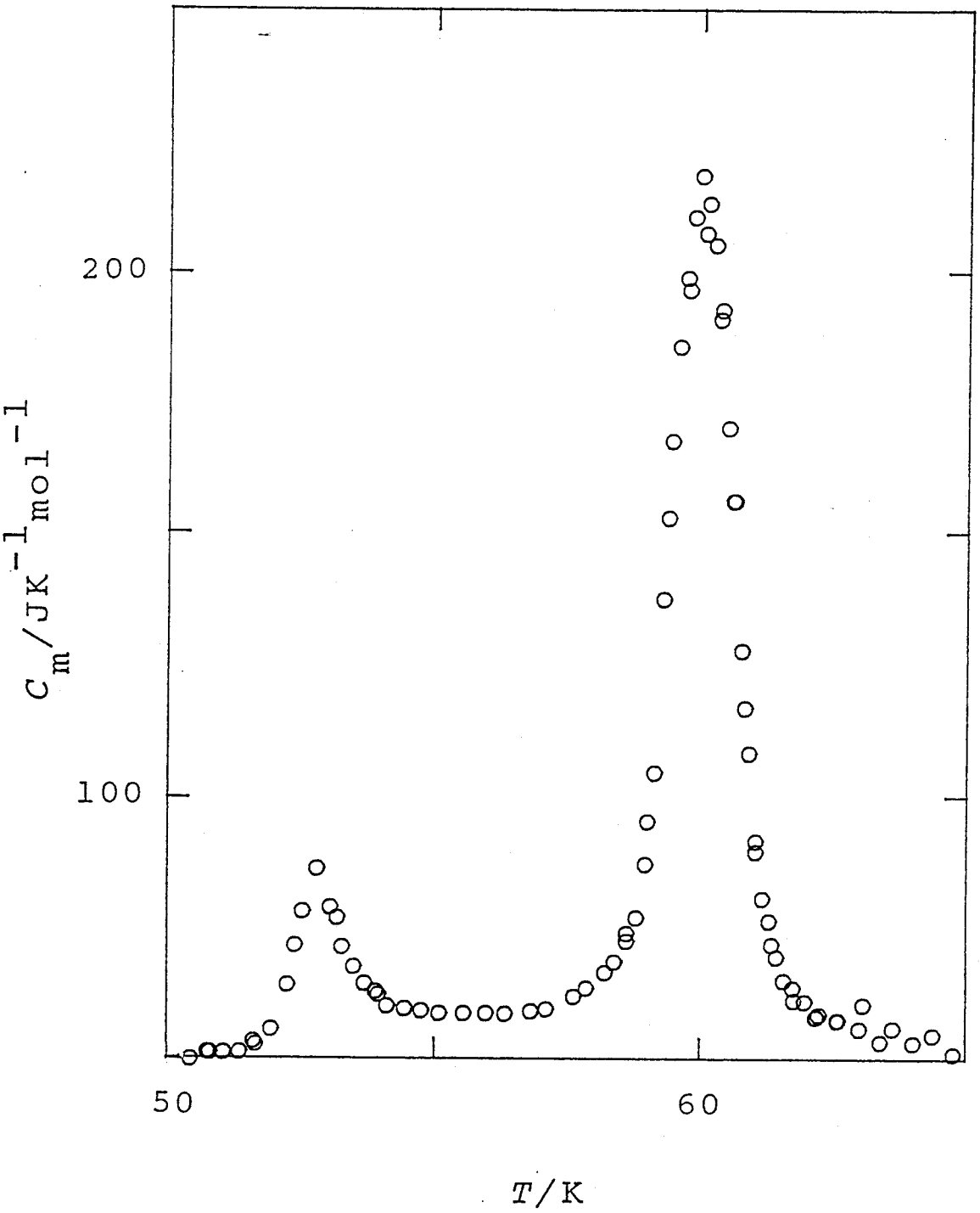

Fig. V-9(b) Molar heat capacity of CD_4 commensurate monolayer on graphite for n_s = 1.57 mmol (melting region).

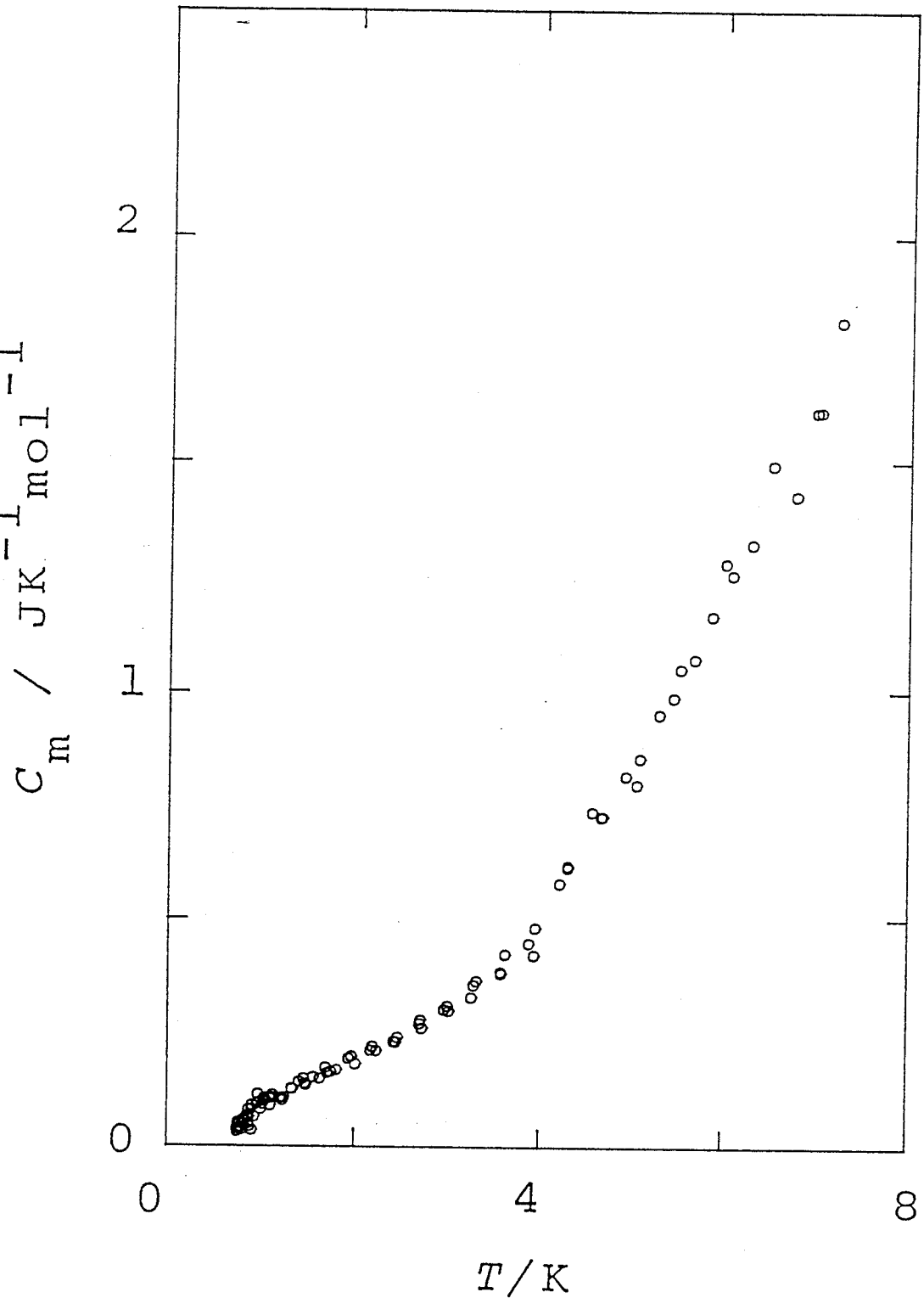

Fig. V-10 Molar heat capacity of CD_4 commensurate monolayer on graphite for n_a = 0.968 mmol.

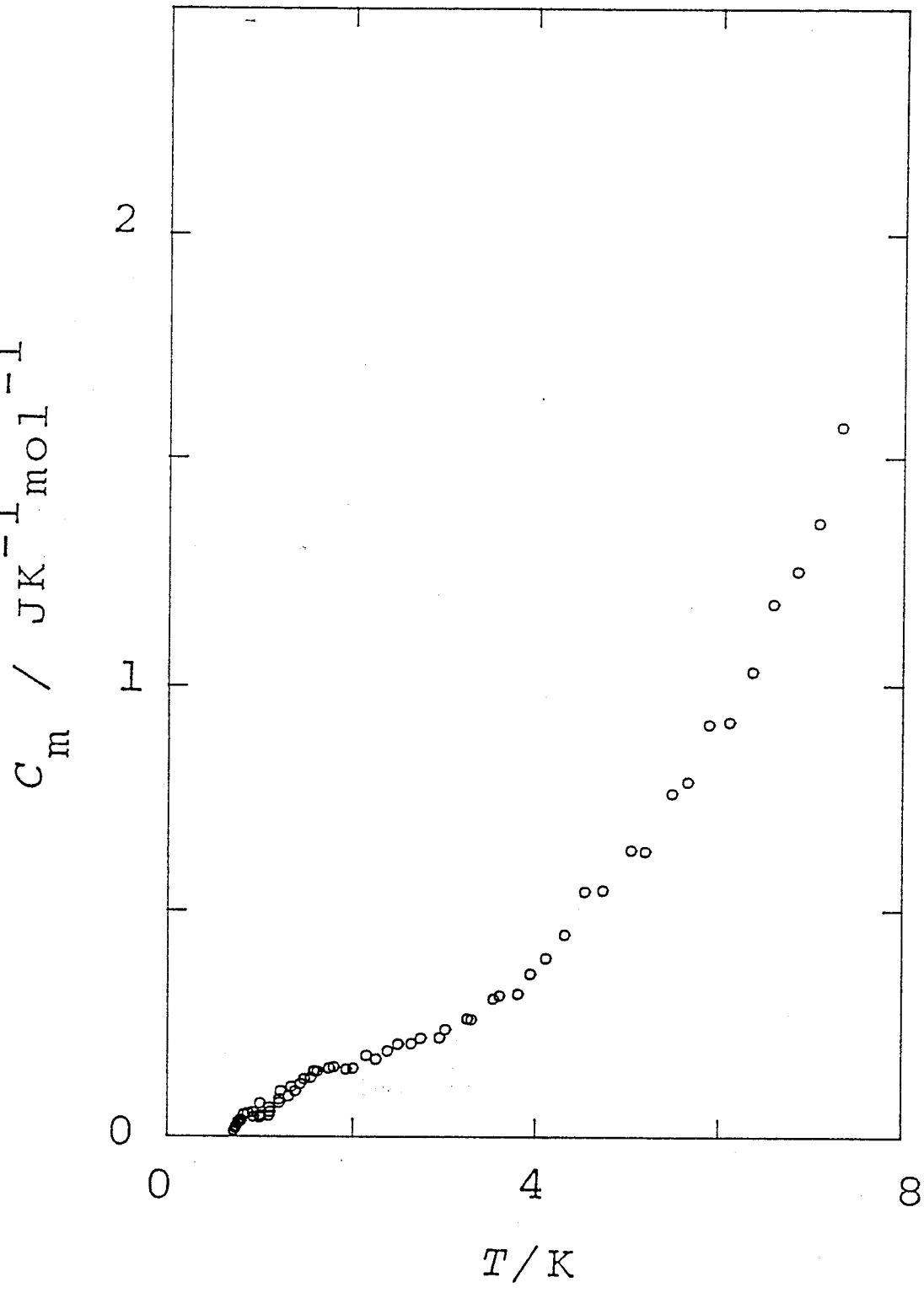

Fig. V-11 Molar heat capacity of CD_4 incommensurate monolayer on graphite for n_s = 1.15 mmol.

was estimated to be 123 K from the mass effect. The excess heat capacities over that arising from the lattice vibrations were thus obtained and are shown in Figs. V-12 and V-13 for CH_4 and CD_4, respectively. After subtraction of the normal portion of the heat capacity, an additional anomaly became discernible for CD_4 at 32 K. This is presumably due to the rotational phase transition in the commensurate phase which has been overlooked in the previous measurements. It should be noted that the transition point is higher than those obtained for the bulk solid (22.4 and 27.2 K for CD_4, ref. 17). For the CH_4 monolayer, such phase transition could not be specified. The rotational heat capacity exhibited only a slight hump around 40 K, suggesting that the hindered rotation rather than the librational motion would occur at higher temperatures.

V-3-4 Rotational Tunneling

The heat capacity obtained between 0.7 and 7 K for the commensurate CH_4 (n_a = 0.886 mmol) is plotted in Fig. V-14 as a function of temperature. Below 2 K, the experimental heat capacity curls up beyond the lattice contribution (solid curve in Fig. V-14), indicating that some low-energy excitations must be relevant. However, the contribution from the tunneling levels (broken curve in Fig. V-13) ought to be much larger than that observed, if the system is in equilibrium. The problem is now how this discrepancy can be compromised.

It should be noted here that the conversion between the different spin species (A, T and E) of methane must be extremely slow unless some magnetic interactions come to work. The situation is similar to the case of hydrogen, in which there are two spin species named ortho- and para-H_2. In the case of CH_4 on graphite, therefore, the excitation between the two T levels ($T_{2,3} \leftrightarrow T_1$) should only be relevant. Moreover, the composition of the spin species may be frozen-in at the ratio of 5 : 9 : 2 for A, T and E, which is the equilibrium composition at sufficiently high temperatures.

In Fig. V-15, the excess heat capacities over the lattice contribution are plotted both for the commensurate CH_4 (a) and

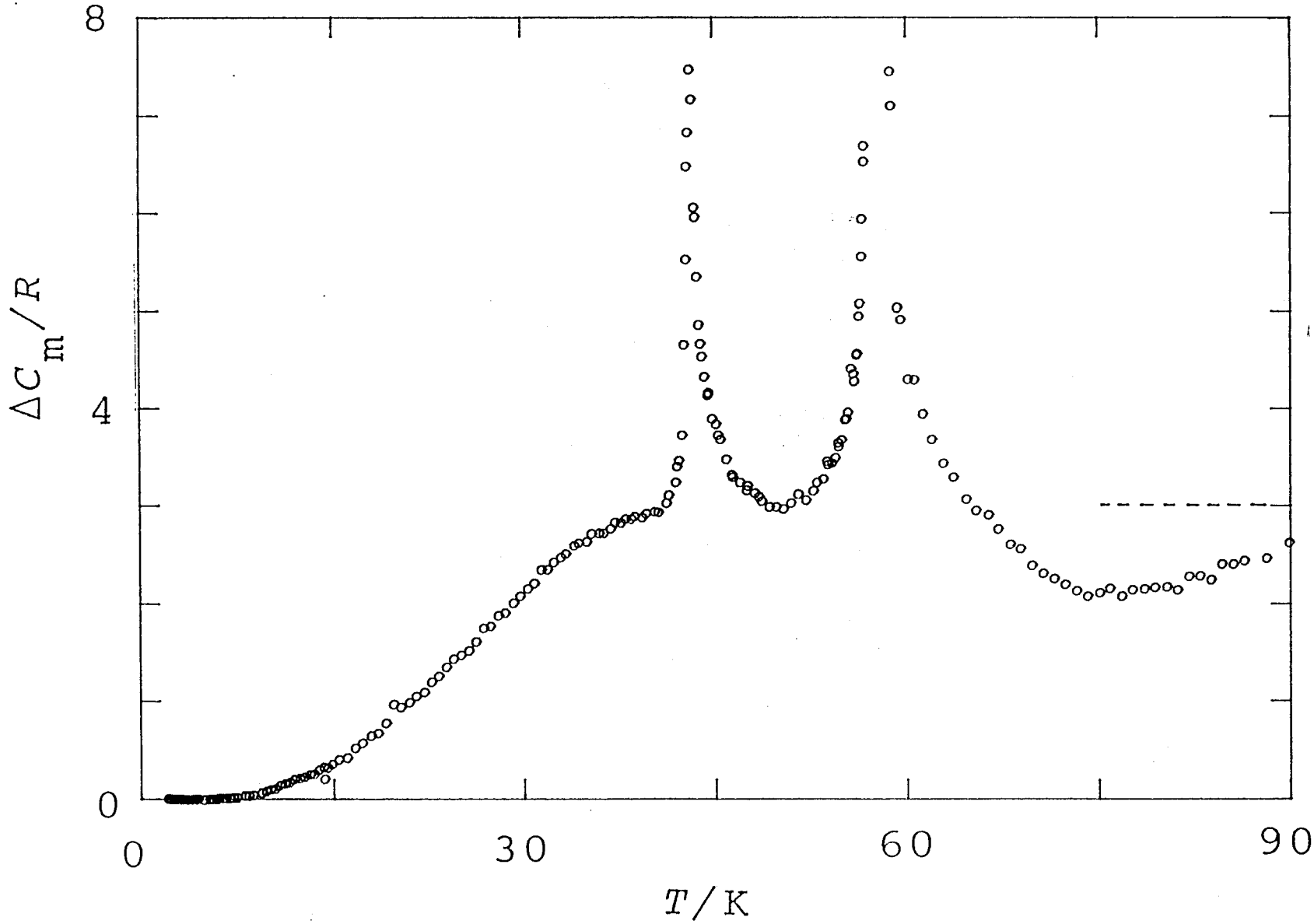

Fig. V-12 Excess heat capacity including the rotational contribution for the CH_4 monolayer in the commensurate phase. The broken line indicates $3R$.

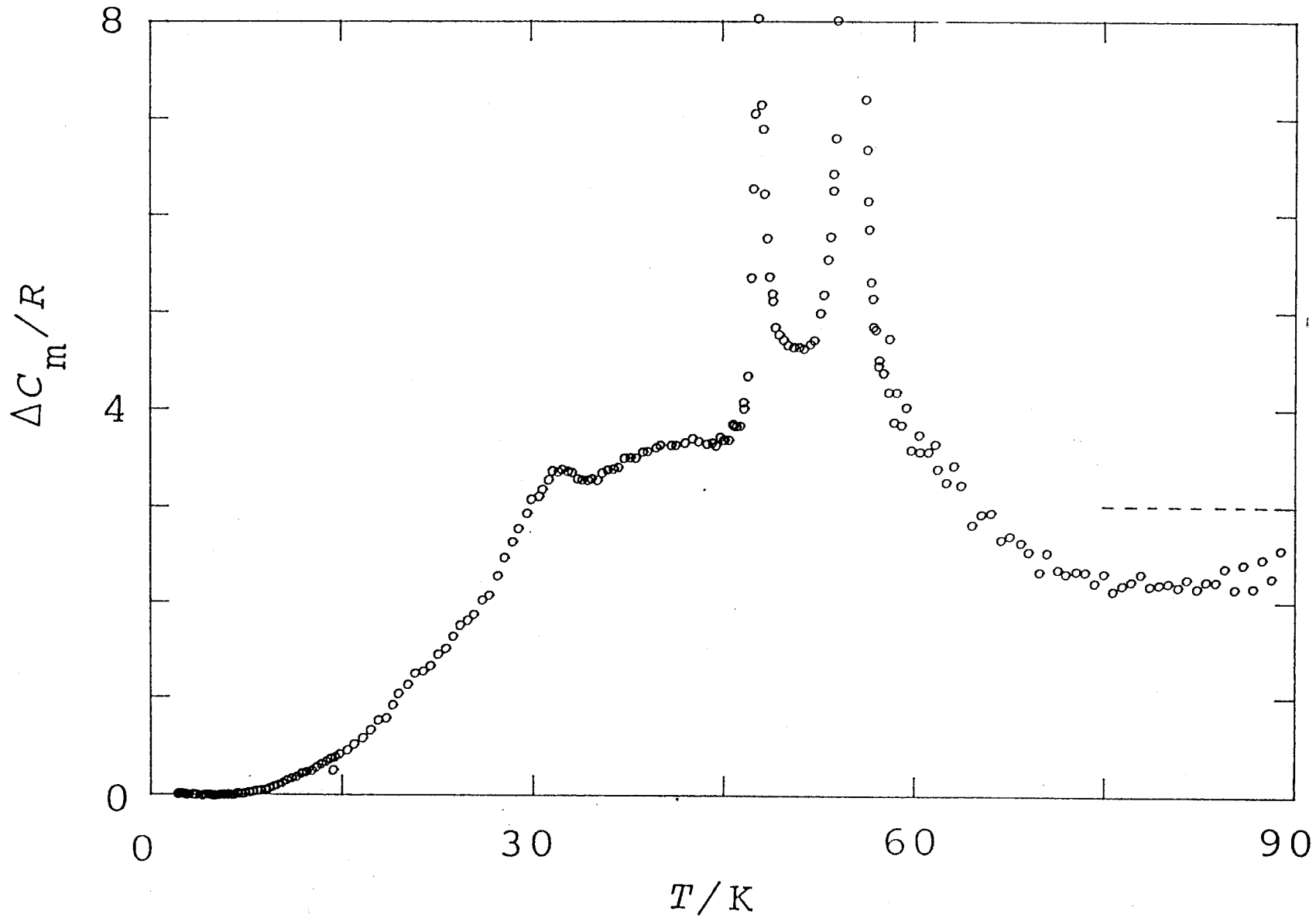

Fig. V-13 Excess heat capacity including the rotational contribution for the CD_4 monolayer in the commensurate phase. The broken line indicates $3R$.

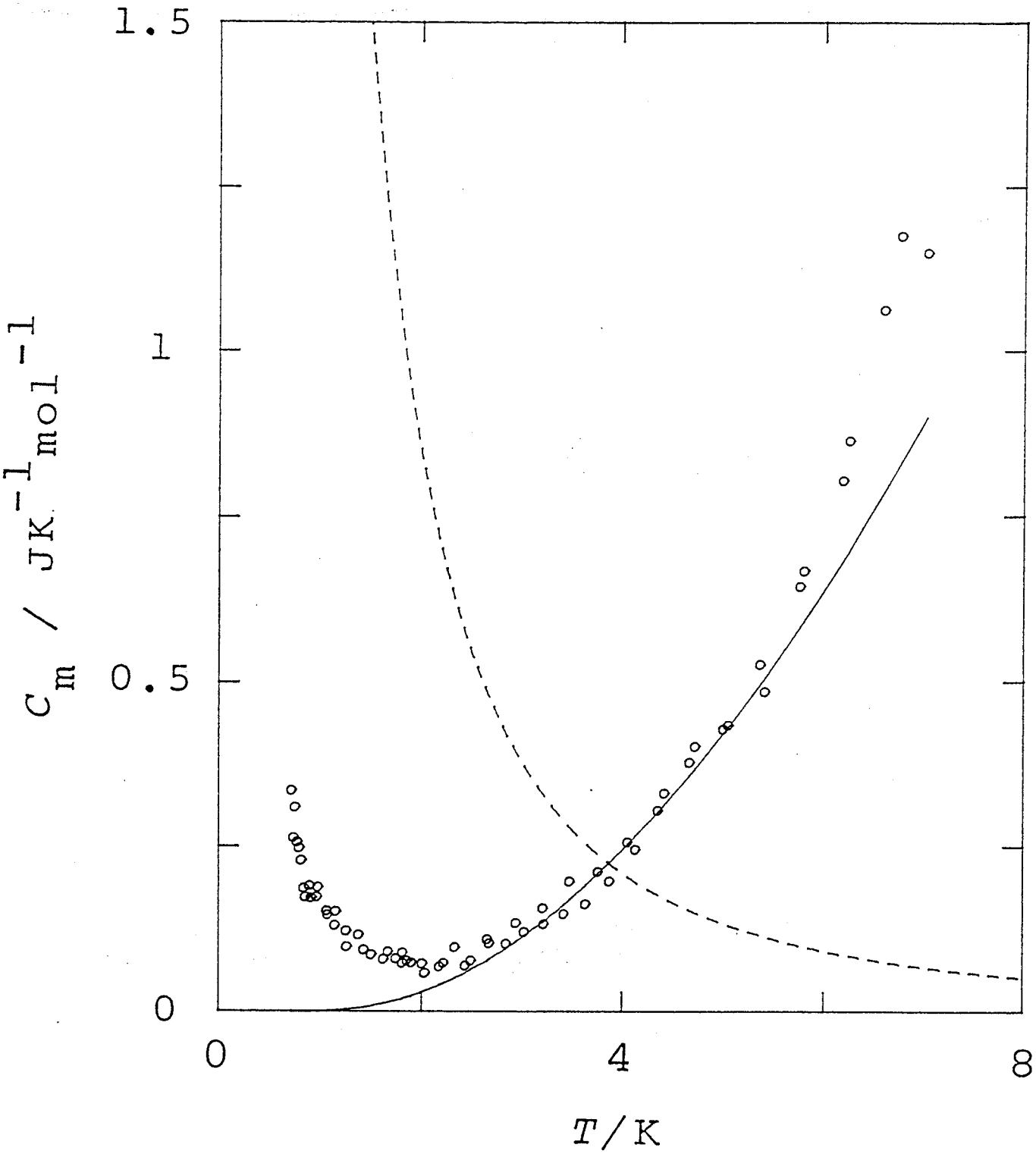

Fig. V-14 Molar heat capacity of the CH_4 commensurate phase for n_s = 0.886 mmol: The solid line indicates the lattice contribution and the broken line indicates the contribution from Schottky heat capacity calculated from the values listed in Table V-1.

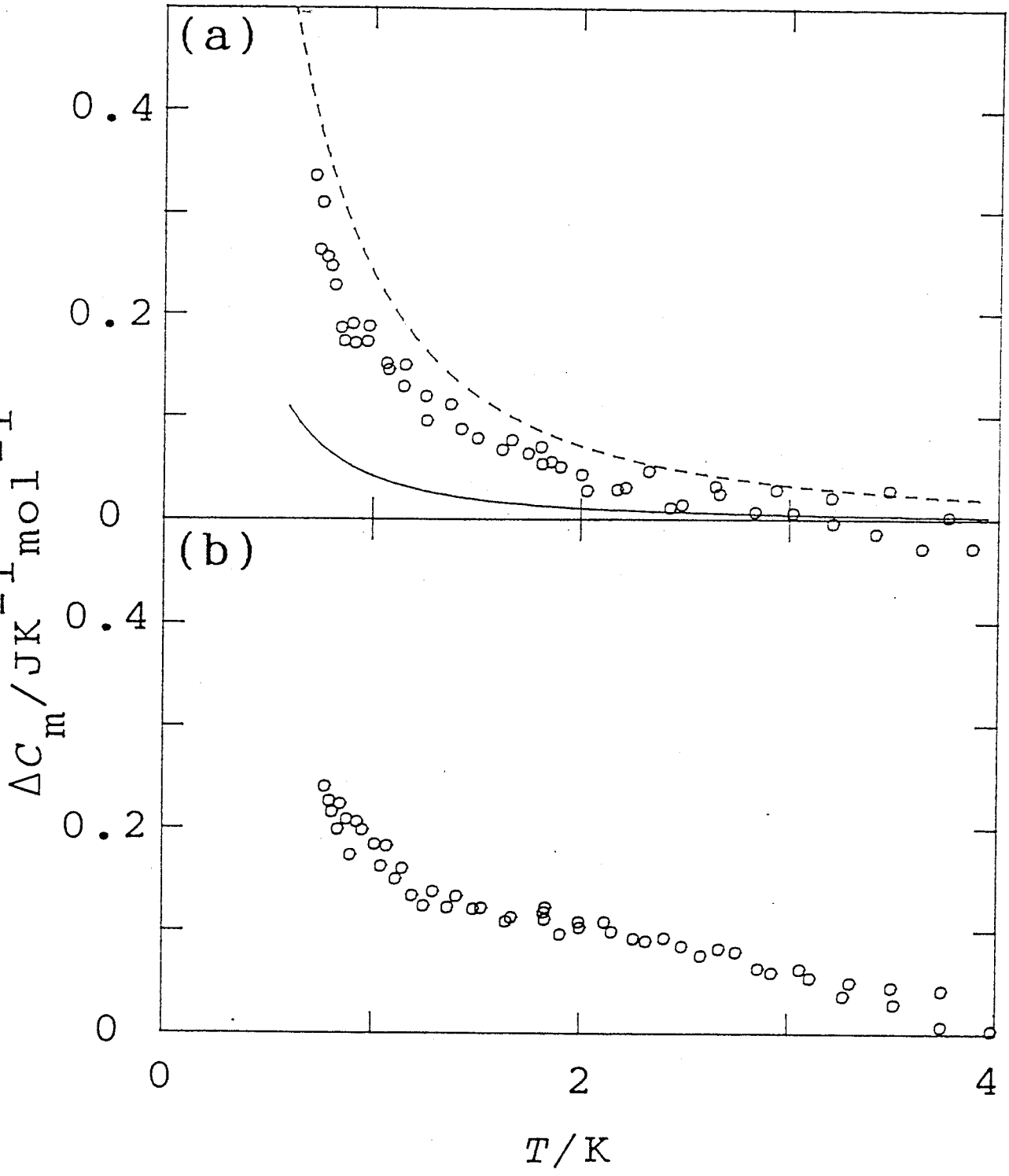

Fig. V-15 Excess heat capacities over the lattice contribution for the (a) commensurate and (b) incommensurate phases of CH_4 on graphite. The solid curve indicates the contribution from the *T-T* transition only. The broken curve iindicates the contribution from the *E-T* and *T-T* transitions.

the incommensurate $_{\perp}CH_4$ (b). If no conversion occurs between the different spin species, only the small contribution from ($T_{2,3} \leftrightarrow T_1$) can be seen as shown by the solid curve in Fig. V-15(a). On the other hand, if the conversion between the E and T species is allowed, the contribution becomes larger (broken curve in Fig. V-15(a)). Our experimental heat capacities are located somewhere between them. The fact may indicate that the system contains small amount of some magnetic impurities which can convert the spin species slowly to some extent toward the equilibrium value during the measurement time.

In order to accelerate the rate of spin conversion, a small amount of O_2 was doped in the monolayer. The results will be described in the following chapter. Before doing it, an impurity effect of CHD_3 contained in CD_4 on the thermal property is described briefly.

V-3-5 CHD_3 as an Impurity in CD_4

The heat capacity of the CD_4 monolayer showed a hump around 2 K both in the commensurate and incommensurate phases. The excess heat capacities over the lattice contribution are plotted in Fig. V-16. Here, the cut-off temperature Θ_c was estimated to be 8 K, being smaller than that obtained from a neutron scattering study (= 14.5 K, ref. 16). Initially the anomaly puzzled us because the contribution from the tunneling in CD_4 on graphite must be shifted to much low temperatures. It turned out that the anomaly came from the tunneling of CHD_3 contained in the CD_4 sample as an impurity.

According to a combined study of theoretical calculation, calorimetric and neutron scattering experiments for CH_3D on graphite (refs. 19, 20 and 21), there are two types of the pocket states (ref. 22); one for the D atom pointing away from the surface (D-up state) and the other for the D atom pointing toward the surface (D-down state). Analysis of the Schottky heat capacity observed previously (ref. 21) indicated that the D-down state is more stable than the D-up state by 380 μeV (= 4.4 K). Since CHD_3 has the same symmetry as CH_3D, the situation should be analogous. We then assume that the H-up

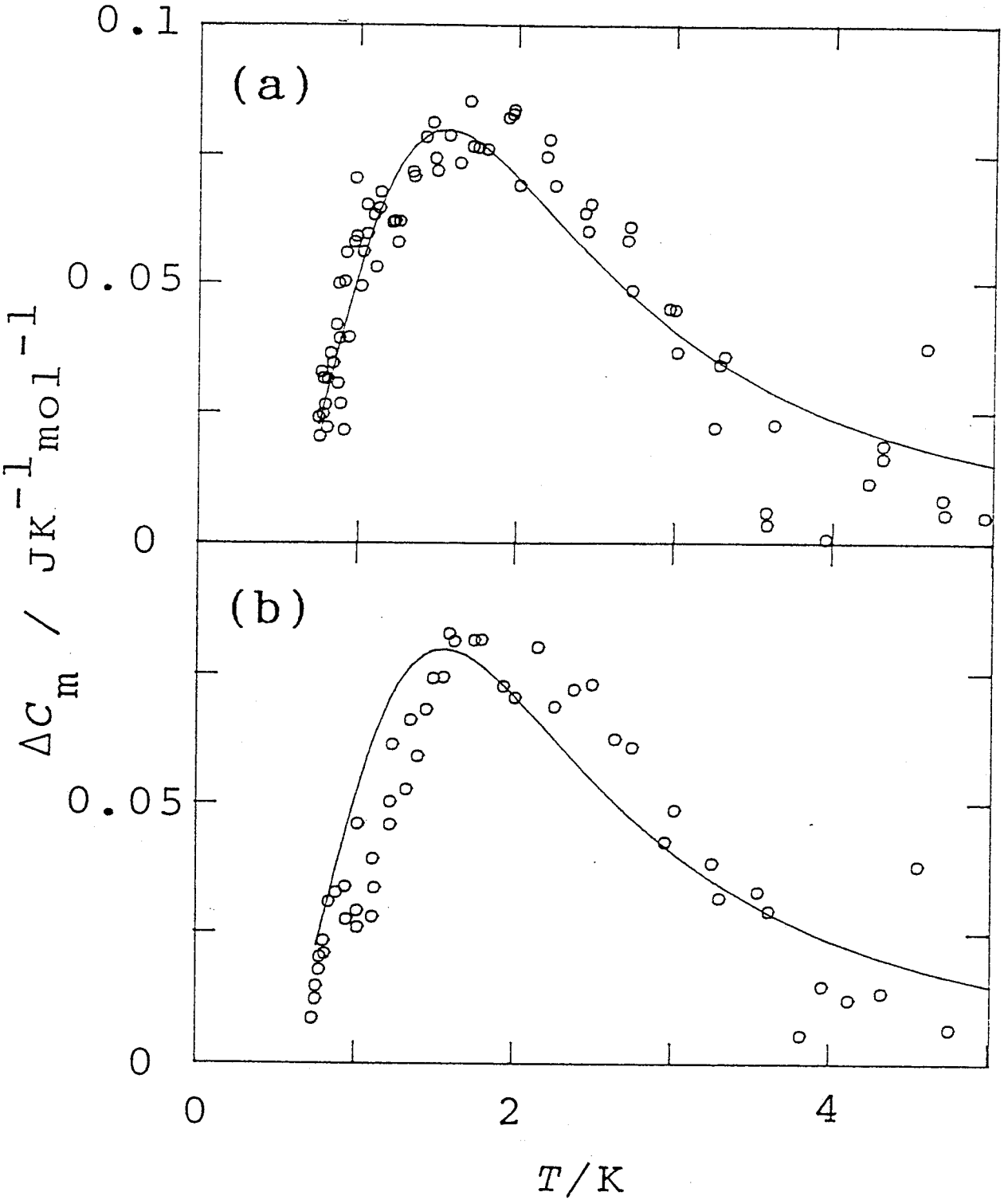

Fig. V-16 Excess heat capacities observed for the CD_4 sample: (a) commensurate and (b) incommensurate phases. They are attributed to the tunnel splitting of CHD_3 contained in the sample. The solid curves indicate the contribution of the isotopic impurity the concentration of 1.5 mol % of CHD_3.

state is more stable than the H-down state by the same energy. The amount of CHD_3 was obtained from the fitting of the experimental heat capacity data (solid curve in Fig. 16) both for the commensurate and incommensurate phases. The result gave us the isotopic purity of CD_4 as 99.62 %, which is slightly poorer than that stated (99.9 %).

References to Chapter V

1. N.C. Parsonage and L.A.K. Staveley, *Disorder in Crystals*, Oxford Univ. Press, (1978) and references therein.
2. H.M. James and T.A. Keenan, *J. Chem. Phys.* 31, 12 (1959).
3. W. Press, *J. Chem. Phys.* 56, 2597 (1972).
4. T. Nagamiya, *Prog. Theor. Phys.* 6, 702 (1951).
5. W. Press, *Single-Particle Rotations in Molecular Crystals*, Springer-Verlag, (1981).
6. A. Thomy and X. Duval, *J. Chim. Phys.* 67, 1101 (1970).
7. P. Vora, S.K. Sinha, and R.K. Crawford, *Phys. Rev. Lett.* 43, 704 (1979).
8. T. Rayment, R.K. Thomas, G. Bomchil and J.W. White, *Mol. Phys.* 43, 601 (1981).
9. R. Marx and E.F. Wassermann, *Surf. Sci.* 117, 267 (1982).
10. J.Z. Larese and R.J. Rollefson, *Phys. Rev.* B31, 3048 (1985).
11. M.V. Smalley, A. Ḧuller, R.K. Thomas and J.W. White, *Mol. Phys.* 44, 533 (1981).
12. H.K. Kim, Q.M. Zhang and M.H.W. Chan, *Phys. Rev.* B34, 4699 (1986).
13. M.W. Newbery, T. Rayment, M.V. Smalley, R.K. Thomas and J.W. White, *Chem. Phys. Lett.* 59, 461 (1978).
14. G. Bomchil, A. Hüller, T. Rayment, S.J. Roser, M.V. Smalley, R.K. Thomas and J.W. White, *Phil.Trans. R. Soc. Lond.* B290, 537 (1980).
15. R.P. Humes, M.V. Smalley, T. Rayment and R.K. Thomas, *Can. J. Chem*, 66, 557 (1988).
16. H.J. Lauter, V.L.P. Freank, H. Taub and P. Leiderer, *Physica* B165&166, 611(1990).
17. J.H. Colwell, E.K. Gill and J.A. Morrison, *J. Chem. Phys.*

39, 635 (1963).
18. E.B. Wilson, Jr., *J. Chem. Phys.* 3, 276 (1935).
19. K. Maki, *J. Chem. Phys.* 74, 2049 (1981).
20. A. Inaba and J.A. Morrison, *Bull. Chem. Soc. Jpn.* 61, 25 (1988).
21. P.C. Ball, A. Inaba, J. A. Morrison, M.V. Smalley and R.K. Thomas, *J. Chem. Phys.* 92, 1372 (1990).
22. A. Hüller, *Phys. Rev.* B16, 1844 (1977).

Chapter VI Methanes on Graphite Part II. Rate of Spin Conversion

VI-1 Introduction

It is well known that the spin conversion problem was first considered for hydrogen. According to an early theory (ref. 1), the dipole-dipole interactions between the protons are relevant to the ortho-para conversion in solid hydrogen. Moreover, it was claimed that only the intermolecular interactions are effective. The intramolecular interactions cannot cause conversion because of the selection rule for parity.

In the case of methane, there are three different spin species; meta-, ortho- and para-CH_4 (or A,T and E species). It was pointed out that both the inter- and intra-molecular dipole-dipole interactions are relevant to the conversion (refs. 2 and 3), which complicates the problem. Moreover, in the case of solid CH_4, three-forth of the constituent molecules are located at a site of D_{2d} symmetry, whereas the remainings are at a site of O_h symmetry. The energy scheme for the rotational ground state is totally different at the two sites. An NMR study indicated that the conversion rate for the molecules at O_h symmetry is much faster than that for those at D_{2d} symmetry (ref. 4). It is interesting to know how the rate of spin conversion is accelerated by a paramagnetic impurity such as molecular oxygen O_2 (ref. 5). According to an NMR study (ref. 6), the rate of spin conversion in bulk solid is proportional to the concentration of O_2. A theoretical consideration (ref. 3) supported this result.

For the CH_4 monolayer on graphite, all the molecules sit on a site of C_{3v} symmetry. Since the spin conversion should be accompanied by a large amount of heat, the rate may be determined calorimetrically by following the enthalpy relaxation under an adiabatic condition.

The objective of the study is two-fold. First, we determine the heat capacity of the CH_4 monolayer in its equilibrium state including the spin system. To achieve this, small amounts of O_2

were doped into the monolayer so as to achieve the rapid equilibrium among the three spin species. Secondary, we investigate the catalytic effect of O_2 in the monolayer as functions of temperature and concentration. It may suggest a possible mechanism for the conversion.

Incidentally, an additional investigation on the miscibility of methane and oxygen at the surface of graphite turned out to be necessary in order to understand the energy state of the oxygen itself. If the O_2 molecules are isolated in the matrix of methane molecules, the splitting of the triplet state of O_2 may be observed in the heat capacity (ref. 7). We also investigate the system of CD_4 doped with O_2.

VI-2 Experimental Details

The calorimeter assembly and the sample gases used were all the same as those described in the previous chapters. The amounts of sample gases used are summarized in Table VI-1.

VI-3 Results and Discussion

VI-3-1 Heat Capacity

For the CH_4 on graphite, the heat capacity measurement was performed between 1.5 - 7 K at two coverages; one at the commensurate coverage and the other at the incommensurate coverage. Different mole fraction of O_2 was used (see Table VI-1). The molar heat capacity of CH_4 is listed in Tables VI-2, VI-3, VI-4, VI-5, VI-6 and VI-7, respectively. It is plotted in Figs. VI-1, VI-2, VI-3, VI-4, VI-5 and VI-6, respectively. Here the contribution of the dopant to the monolayer heat capacity can be ignored because of the lowest temperature region where the contribution arising from the spin conversion of CH_4 overwhelms the remaining parts.

For the CD_4 doped with 1 mol % of O_2, the heat capacity measurement was performed between 0.7 and 7 K both at the commensurate and the incommensurate coverages. The molar heat

Table VI-1 The amount of gases used for the various samples.

phase	$\frac{CH_4}{mmol}$	$\frac{O_2}{\mu mol}$	O_2 mol %
commensurate	0.963	10.1	1.0
commensurate	0.963	6.4	0.66
commensurate	0.965	4.1	0.42
incommensurate	1.14	12.0	1.0
incommensurate	1.14	4.6	0.40
incommensurate	1.06	1.5	0.14
phase	$\frac{CD_4}{mmol}$	$\frac{O_2}{\mu mol}$	O_2 mol %
commensurate	0.948	10.0	1.1
incommensurate	1.15	11.6	1.0

Table VI-2 Molar heat capacity of CH_4 commensurate monolayer on graphite doped with 1.0 mol % O_2.

T / K	C_m / $JK^{-1}mol^{-1}$	T / K	C_m / $JK^{-1}mol^{-1}$	T / K	C_m / $JK^{-1}mol^{-1}$
1.405	1.092	2.843	0.685	4.946	0.685
1.591	1.021	3.112	0.657	5.310	0.780
1.770	0.864	3.383	0.629	5.665	0.854
1.956	0.792	3.664	0.618	6.038	0.964
2.139	0.779	3.951	0.606	6.442	1.155
2.325	0.712	4.252	0.638	6.883	1.154
2.559	0.688	4.581	0.677		

Table VI-3 Molar heat capacity of CH_4 commensurate monolayer on graphite doped with 0.66 mol % O_2.

T / K	C_m / $JK^{-1}mol^{-1}$	T / K	C_m / $JK^{-1}mol^{-1}$
1.840	0.776	1.649	1.068
2.085	0.628	1.886	0.831
2.402	0.490	2.077	0.759
2.824	0.479	2.283	0.539
3.312	0.441	2.531	0.519
3.852	0.427	2.818	0.435
4.396	0.521	3.131	0.458
4.936	0.622	3.500	0.418
5.489	0.747	3.957	0.453
6.050	0.988	4.503	0.530
		5.162	0.659
		5.802	0.899
		6.381	1.090

Table IV-4 Molar heat capacity of CH_4 commensurate monolayer on graphite doped with 0.42 mol % O_2.

T / K	C_m / $JK^{-1}mol^{-1}$	T / K	C_m / $JK^{-1}mol^{-1}$	T / K	C_m / $JK^{-1}mol^{-1}$
3.351	0.478	2.386	0.556	1.984	0.730
3.837	0.517	2.916	0.598	2.483	0.669
4.390	0.505	3.153	0.479	2.887	0.472
4.786	0.569	4.054	0.469	3.265	0.677
5.166	0.683	4.996	0.695	3.636	0.534
5.557	0.849	5.415	0.772	4.013	0.521
5.923	0.996	5.861	0.886	4.361	0.493
6.278	1.064	6.342	1.100	4.136	0.528
				4.496	0.536
				4.852	0.625
				5.230	0.762
				5.644	0.858
				6.117	0.981
				6.551	1.219
				7.013	1.221

Table VI-5 Molar heat capacity of CH_4 incommensurate monolayer on graphite doped with 1.0 mol % O_2.

T / K	C_m / $JK^{-1}mol^{-1}$	T / K	C_m / $JK^{-1}mol^{-1}$	T / K	C_m / $JK^{-1}mol^{-1}$
1.633	1.310	1.810	1.469	2.167	1.307
1.823	1.286	1.942	1.373	2.359	1.201
2.033	1.279	2.094	1.238	2.559	1.195
		2.572	1.155	2.763	1.102
1.316	2.203	2.731	1.075	2.972	1.046
1.479	1.865	3.121	0.883	3.190	1.003
1.629	1.638	3.328	0.950	3.433	0.912
1.779	1.491	3.551	0.934	3.713	0.848
1.929	1.413	4.052	0.827	3.995	0.846
2.120	1.264	4.328	0.825	4.290	0.845
2.347	1.145	4.626	0.820	4.593	0.858
2.508	1.144	4.949	0.834	4.918	0.839
		5.295	0.878	5.262	0.848
		5.640	0.908	5.638	0.901
		6.002	1.013	6.056	0.999
		6.397	1.088	6.508	1.222
		6.822	1.269	6.996	1.317

Table VI-6 Molar heat capacity of CH_4 incommensurate monolayer on graphite doped with 0.40 mol % O_2.

T / K	C_m / $JK^{-1}mol^{-1}$	T / K	C_m / $JK^{-1}mol^{-1}$
2.137	0.992	2.376	1.056
2.402	1.019	2.733	0.677
3.588	0.831	3.137	0.798
4.077	0.683	3.625	0.775
5.815	1.015	4.194	0.746
6.438	1.051	4.772	0.779
7.072	1.286	6.084	0.939
		6.798	1.182

Table VI-7 Molar heat capacity of CH_4 incommensurate monolayer on graphite doped with 0.14 mol % O_2.

T / K	C_m / $JK^{-1}mol^{-1}$	T / K	C_m / $JK^{-1}mol^{-1}$	T / K	C_m / $JK^{-1}mol^{-1}$
3.846	0.883	2.543	0.883	4.693	0.808
4.693	0.808	3.975	0.827	5.501	0.961
5.501	0.961	4.498	0.809	6.217	1.063
6.217	1.063	5.035	0.898	3.129	0.971
3.129	0.971	5.555	1.021	3.759	0.779
3.759	0.779	6.042	1.090	4.621	0.806
4.621	0.806	6.517	1.286	5.392	0.931
5.392	0.931	6.982	1.352	6.078	1.044
6.078	1.044				

Table VI-8 Molar heat capacity of CD_4 commensurate monolayer on graphite doped with 1.1 mol % O_2.

T / K	C_m / $JK^{-1}mol^{-1}$	T / K	C_m / $JK^{-1}mol^{-1}$	T / K	C_m / $JK^{-1}mol^{-1}$
0.813	0.079	2.858	0.281	0.787	0.056
0.827	0.065	3.095	0.349	0.811	0.054
0.843	0.080	3.361	0.362	0.838	0.070
0.861	0.077	3.653	0.426	0.868	0.099
0.881	0.087	3.950	0.488	0.906	0.088
0.905	0.085	4.272	0.607	0.957	0.072
0.934	0.106	4.612	0.674	1.015	0.130
0.970	0.104	4.981	0.757	1.073	0.142
1.018	0.132	5.389	1.028	1.132	0.162
1.071	0.158	5.799	1.218	1.196	0.176
1.127	0.148	6.187	1.275	1.269	0.166
1.195	0.162	6.556	1.493	1.366	0.177
1.284	0.165	6.920	1.632	1.456	0.202
1.393	0.193	7.282	1.910	1.745	0.205
1.528	0.202			1.850	0.225
1.675	0.226	0.885	0.057	1.968	0.233
1.856	0.217	0.903	0.070	2.116	0.246
		0.975	0.104	2.290	0.246
0.791	0.047	1.011	0.113	2.478	0.256
0.806	0.055	1.056	0.149	2.711	0.285
0.823	0.076	1.109	0.138	2.947	0.314
0.843	0.070	1.170	0.173	3.200	0.350
0.864	0.065	1.334	0.173	3.460	0.378
0.890	0.109	1.436	0.196	3.732	0.452
0.925	0.114	1.563	0.208	4.021	0.539
0.977	0.117	1.696	0.200	4.325	0.639
1.034	0.118	1.865	0.223	4.653	0.705
1.094	0.122	2.071	0.220	5.014	0.771
1.158	0.141	2.279	0.256	5.404	1.058
1.238	0.115	2.486	0.280	5.825	1.218
1.328	0.175	2.707	0.299	6.264	1.345
1.424	0.178	2.954	0.305	6.733	1.590
1.522	0.190	3.190	0.356	7.210	1.777
1.632	0.219	3.438	0.391		
1.731	0.231	3.707	0.450		
1.837	0.220	4.016	0.520		
1.950	0.221	4.360	0.664		
2.091	0.221	4.734	0.703		
2.261	0.238	5.122	0.839		
2.443	0.250	5.533	0.996		
2.645	0.271	5.979	1.231		
		6.408	1.442		
		6.772	1.674		

Table VI-9 Molar heat capacity of CD_4 incommensurate monolayer on graphite doped with 1.0 mol % O_2.

T / K	C_m / $JK^{-1}mol^{-1}$	T / K	C_m / $JK^{-1}mol^{-1}$	T / K	C_m / $JK^{-1}mol^{-1}$
0.834	0.026	0.810	0.015	0.787	0.019
0.858	0.041	0.858	0.030	0.807	0.016
0.884	0.016	0.888	0.069	0.831	0.014
0.916	0.045	0.919	0.048	0.855	0.051
0.964	0.057	0.961	0.023	0.885	0.062
1.006	0.072	1.003	0.053	0.919	0.078
1.051	0.097	1.062	0.107	0.960	0.088
1.101	0.077	1.113	0.085	1.000	0.055
1.171	0.109	1.178	0.125	1.058	0.107
1.266	0.147	1.264	0.149	1.107	0.078
1.382	0.146	1.369	0.156	1.172	0.138
1.492	0.159	1.480	0.156	1.257	0.137
1.627	0.162	1.621	0.167	1.347	0.149
1.787	0.167	1.803	0.168	1.443	0.156
1.954	0.178	1.999	0.175	1.553	0.153
2.130	0.182	2.201	0.193	1.685	0.162
2.354	0.204	2.416	0.202	1.833	0.167
2.586	0.219			1.994	0.172
2.841	0.229			2.171	0.183
3.116	0.260			2.410	0.196
3.410	0.301			2.656	0.223
3.727	0.333			2.956	0.246
4.059	0.369			3.303	0.274
4.412	0.470			3.649	0.326
4.785	0.528			3.997	0.353
5.172	0.653			4.345	0.427
5.573	0.729			4.653	0.496
5.998	0.868			4.970	0.559
6.445	1.178			5.323	0.695
6.881	1.385			5.722	0.802
7.270	1.578			6.160	0.966
				6.633	1.097
				7.102	1.225

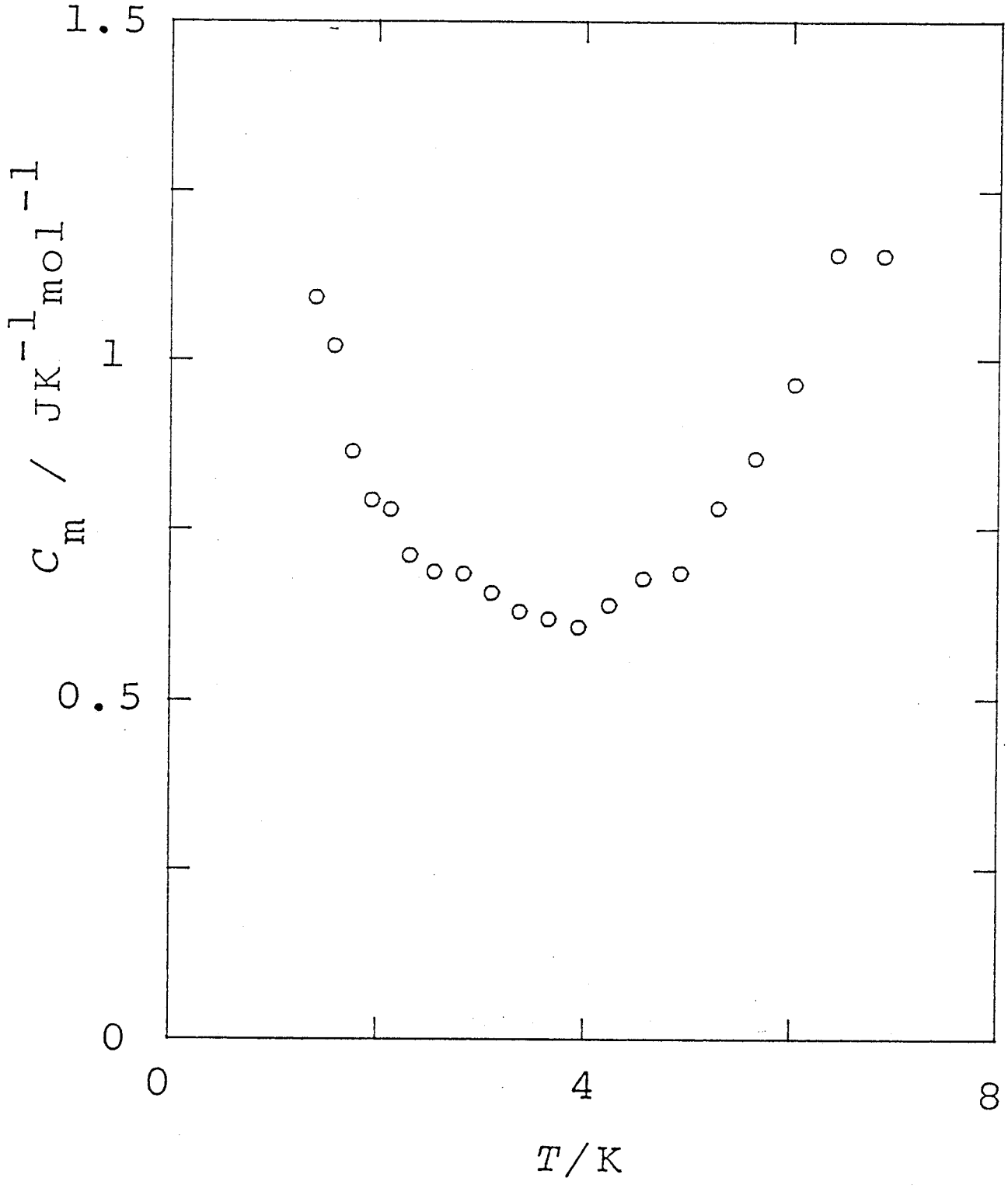

Fig. VI-1 Molar heat capacity of CH_4 commensurate monolayer on graphite doped with 1.0 mol % O_2.

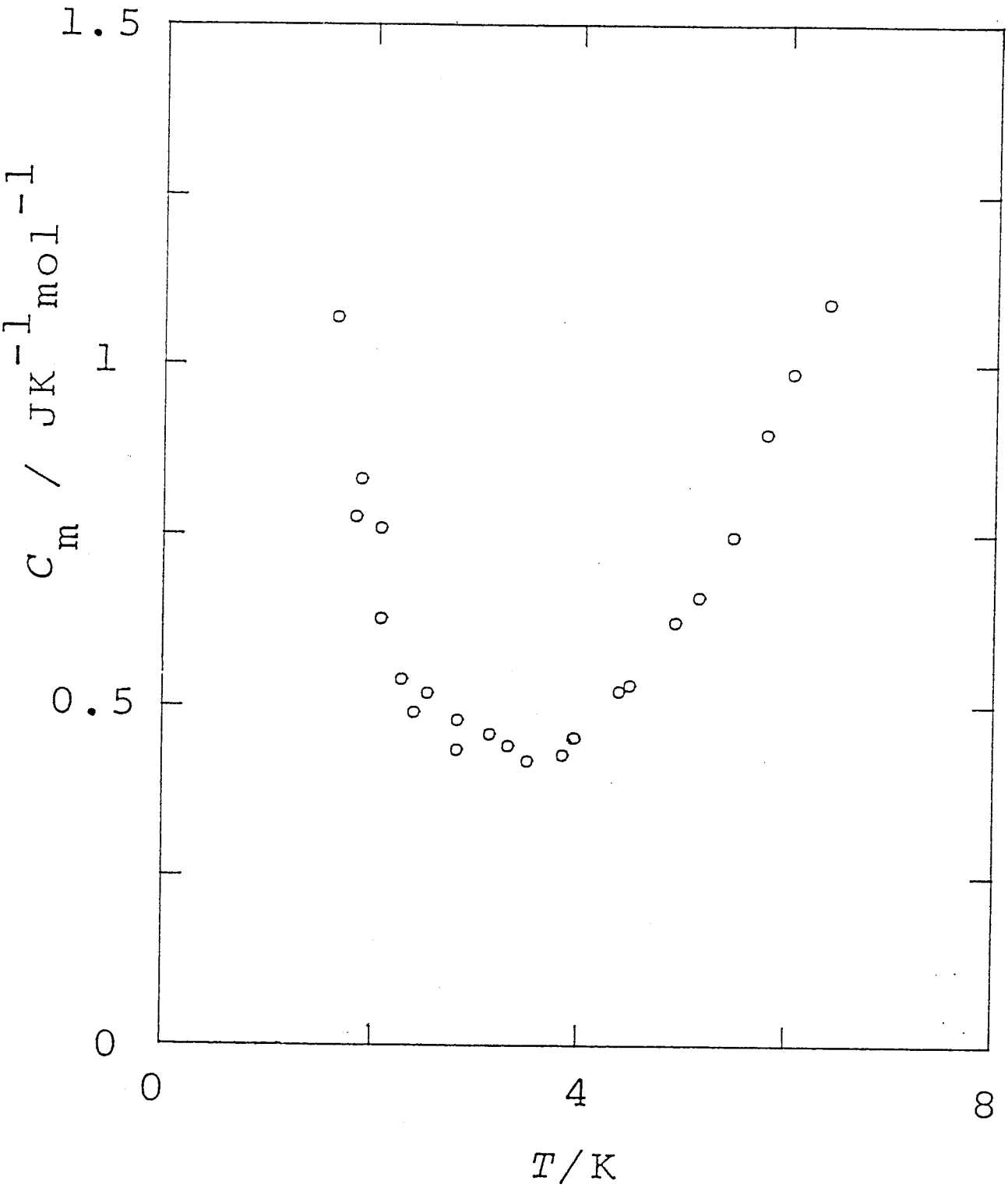

Fig. VI-2 Molar heat capacity of CH_4 commensurate monolayer on graphite doped with 0.66 mol % O_2.

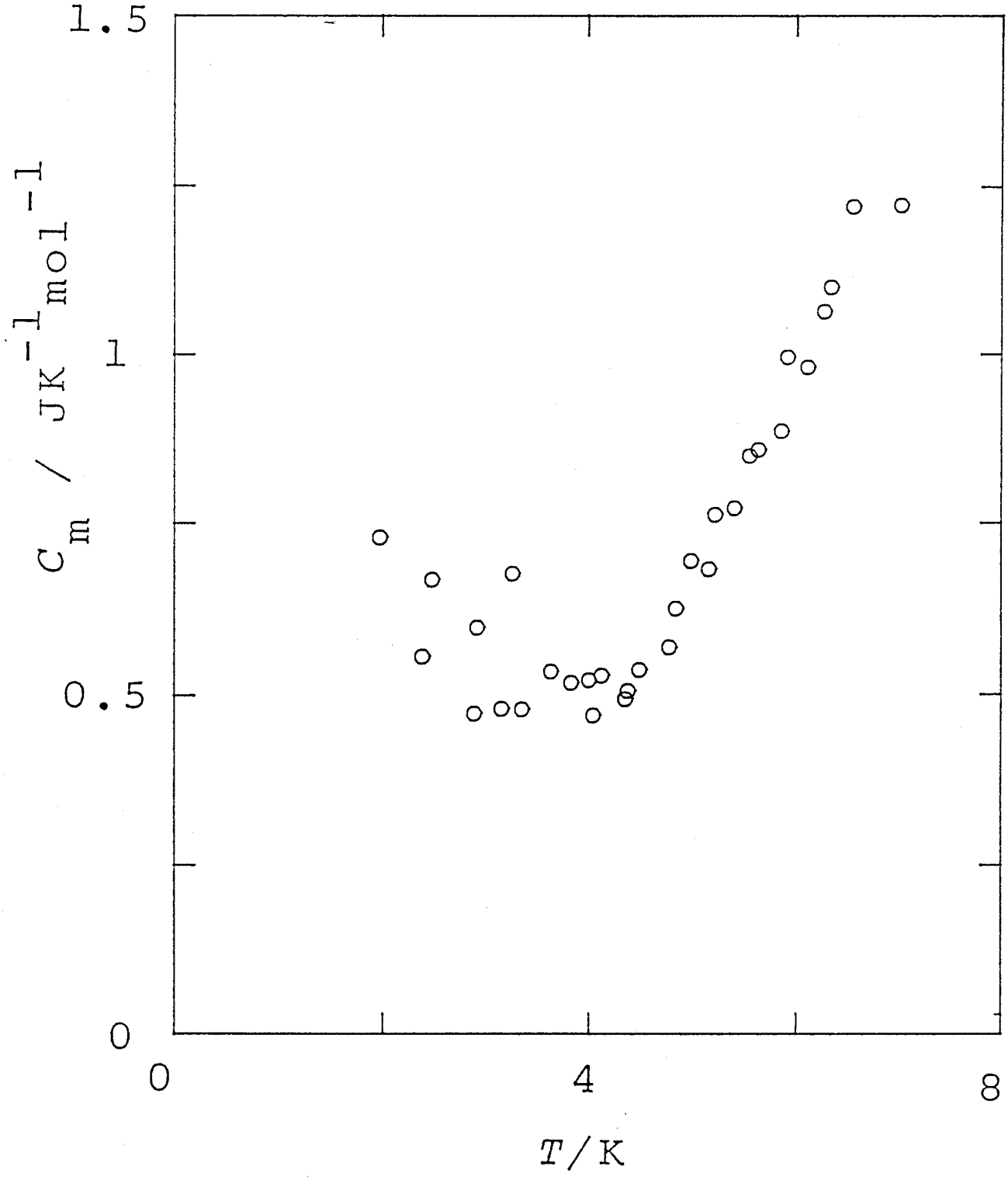

Fig. VI-3 Molar heat capacity of CH_4 commensurate monolayer on graphite doped with 0.42 mol % O_2.

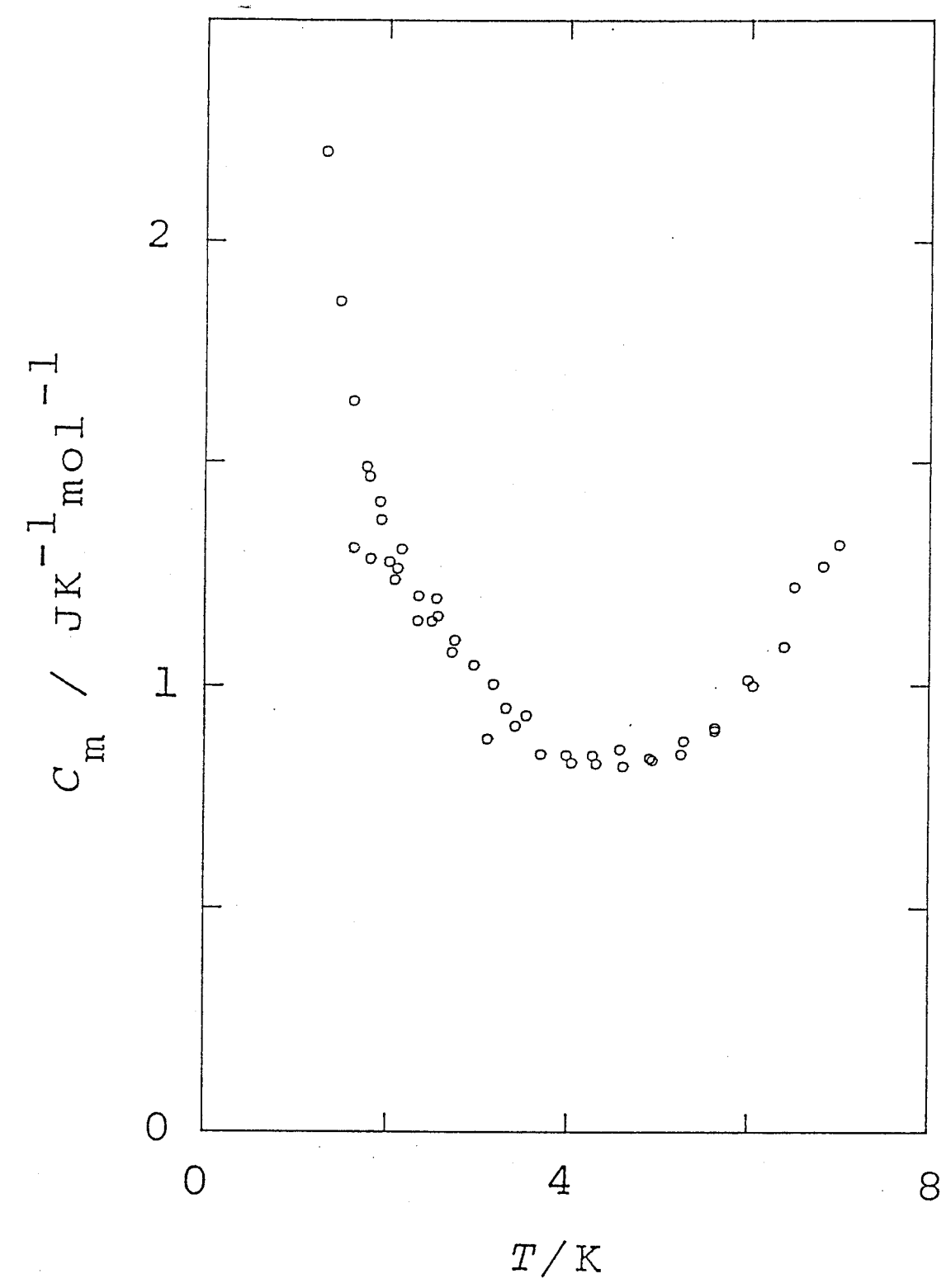

Fig. VI-4 Molar heat capacity of CH_4 incommensurate monolayer on graphite doped with 1.0 mol % O_2.

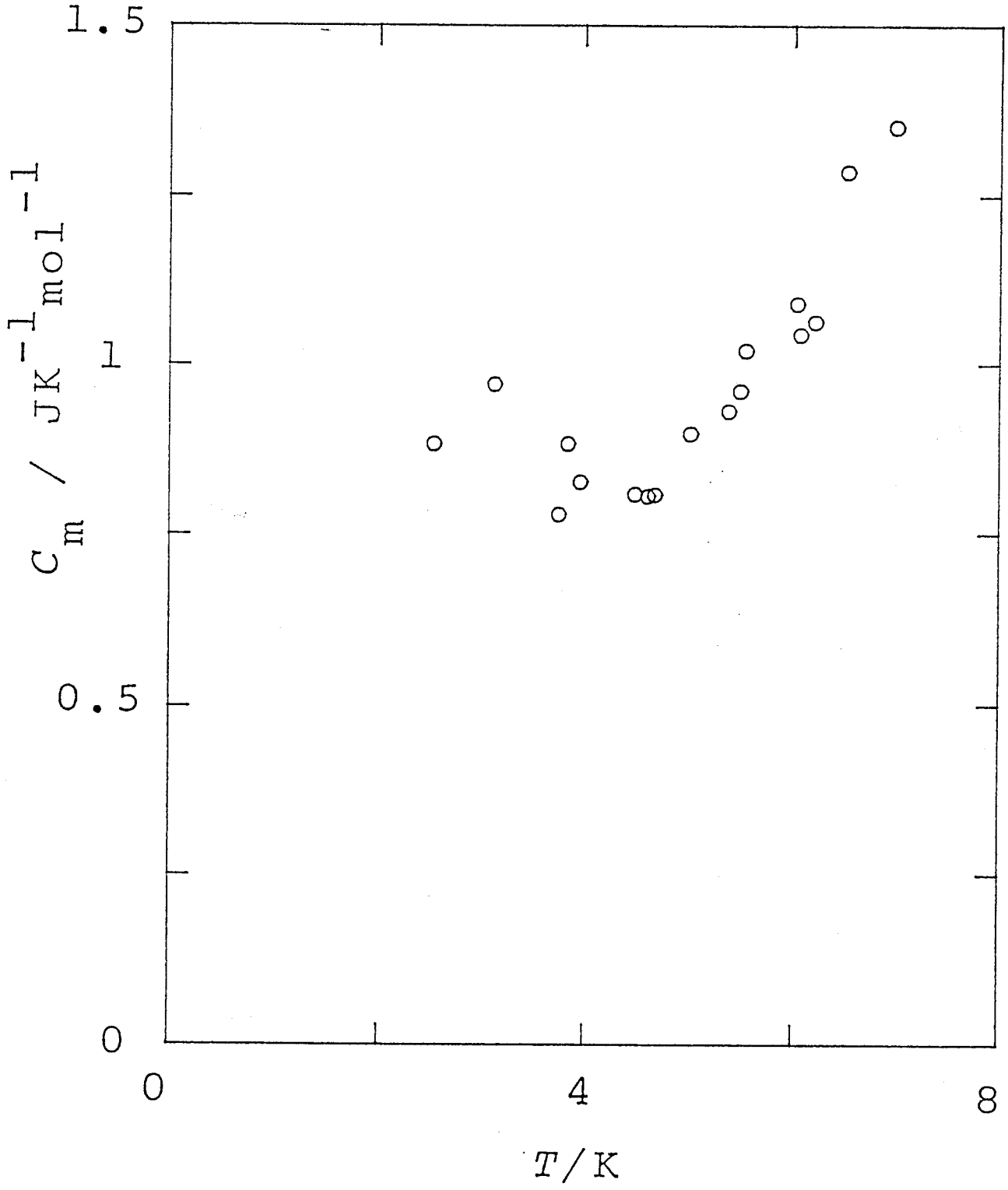

Fig. VI-5 Molar heat capacity of CH_4 incommensurate monolayer on graphite doped with 0.40 mol % O_2.

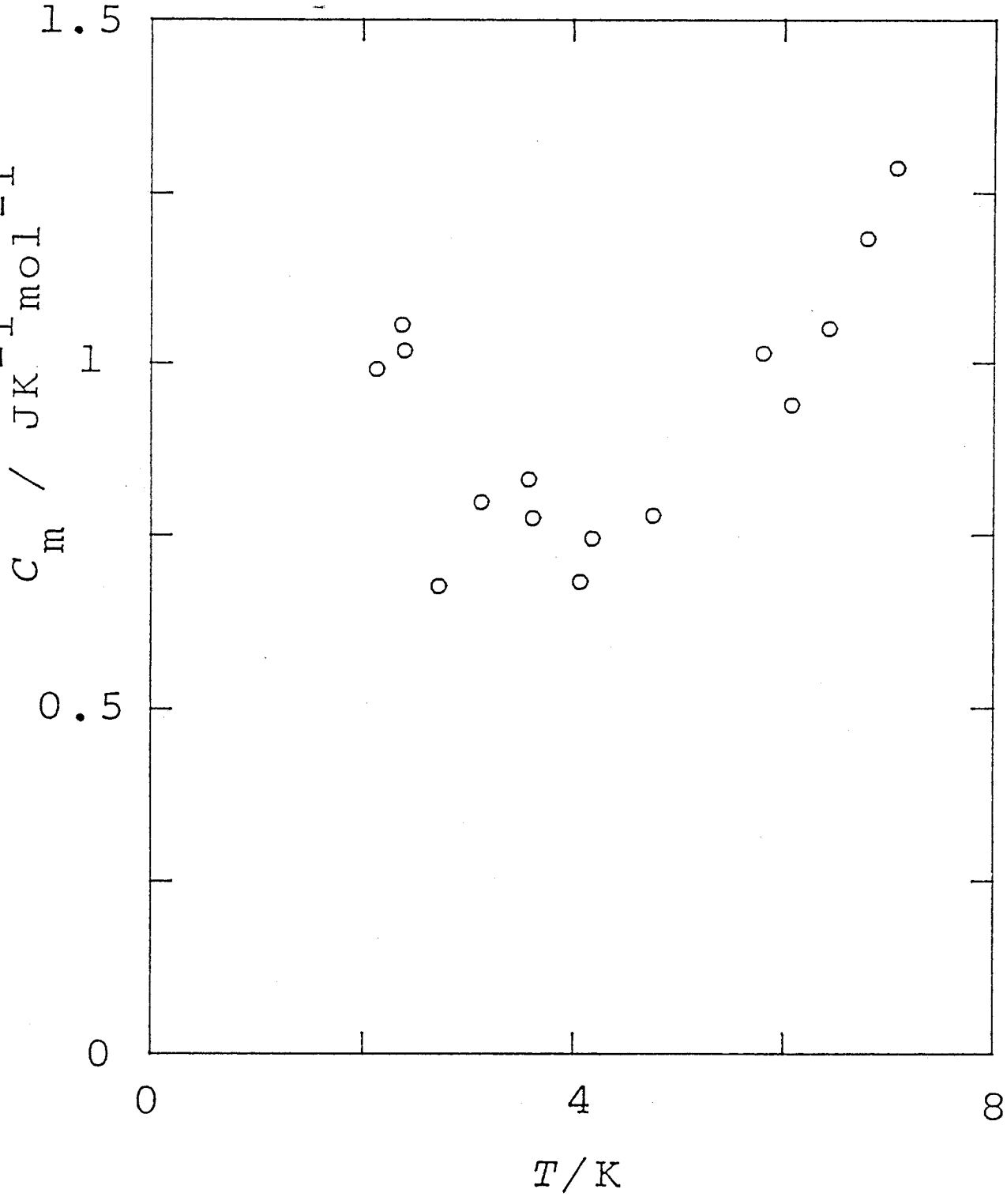

Fig. VI-6 Molar heat capacity of CH_4 incommensurate monolayer on graphite doped with 0.14 mol % O_2.

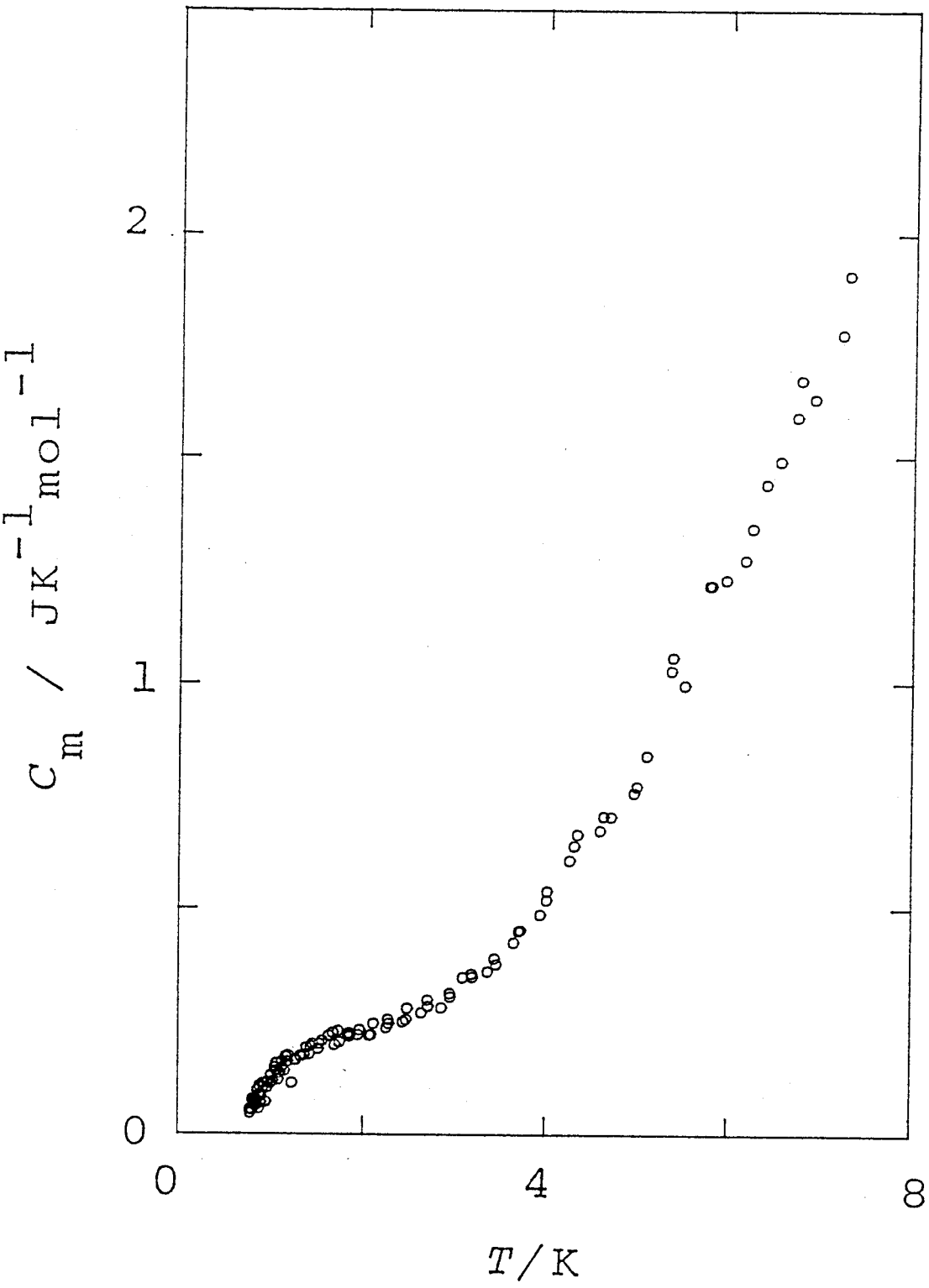

Fig. VI-7 Molar heat capacity of CD_4 commensurate monolayer on graphite doped with 1.1 mol % O_2.

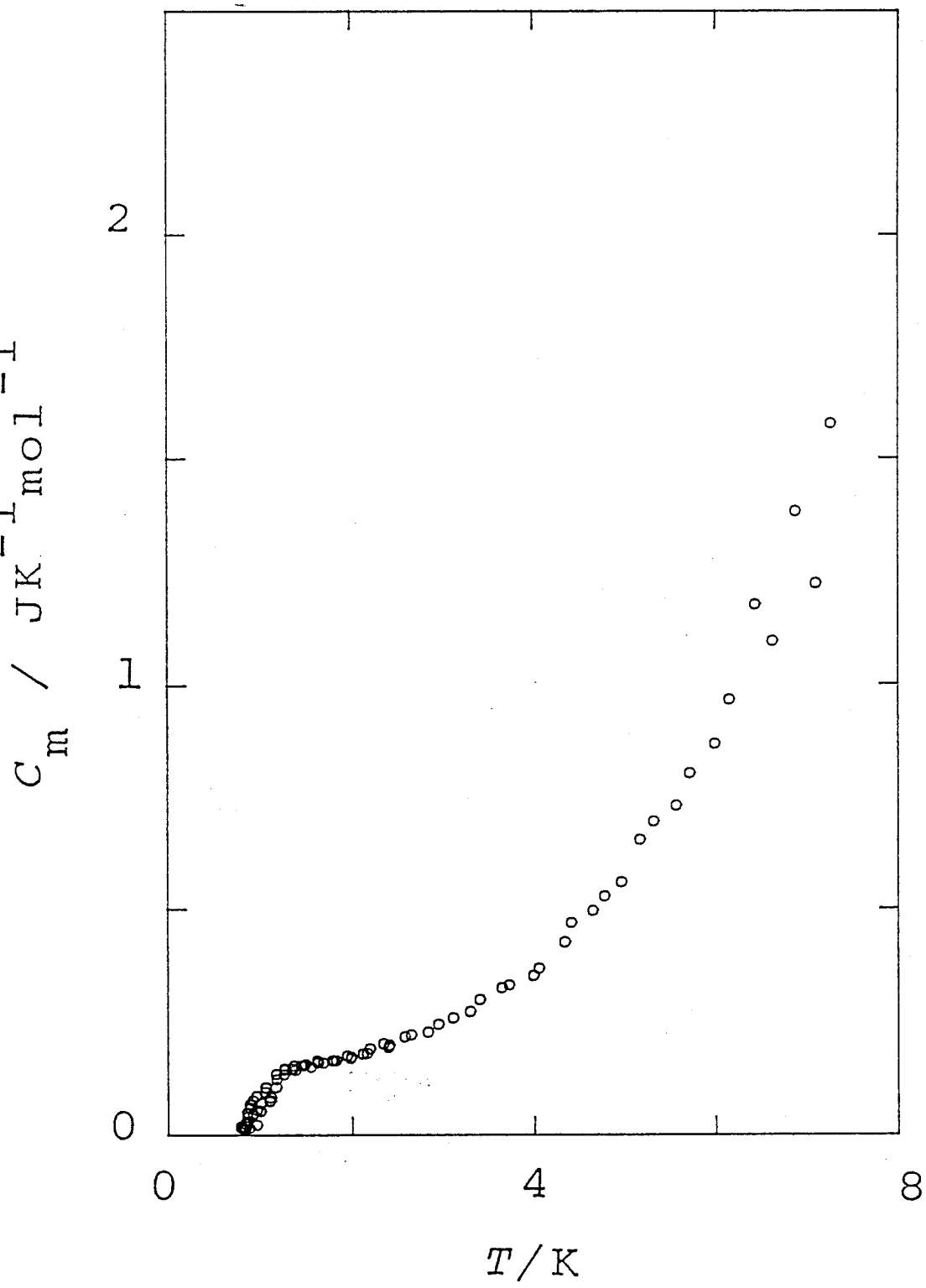

Fig. VI-8 Molar heat capacity of CD_4 incommensurate monolayer on graphite doped with 1.0 % mol O_2.

capacity is listed in Tables VI-8 and VI-9, respectively. and plotted in Figs. VI-7 and VI-8, respectively.

VI-3-2 Equilibrium Heat Capacity and Tunnel Splitting

It was found that the system came to equilibrium rapidly when some amount of O_2 was doped. Figure VI-9 shows the heat capacity obtained for the commensurate phase of CH_4 doped with 0.6 mol % of O_2. The experimental heat capacity is fairly in agreement with those calculated from the energy scheme mentioned above (ref. V-11). At low temperatures, however, the heat capacity could not be determined virtually below 1.5 K owing to the extremely slow rate of conversion.

For the incommensurate phase of CH_4, the heat capacity anomaly was much larger than that for the commensurate phase: Fig. VI-10 shows the result for the incommensurate phase doped with 1 mol % of O_2. The fact may indicate that the tunnel splitting becomes larger and therefore the barrier to rotation becomes lower in the "compressed" incommensurate phase. This observation was really surprising. Since the tunneling modes were broad in the incommensurate phase, little can be said about the energy scheme. One of the possibilities of this effect is that the methane molecules may sit on the surface in a way different from the incommensurate phase.

VI-3-3 Rate of Conversion

The rate of spin conversion was determined by a temperature-jump method. A brief introduction of this method may be helpful.

The rate equation is given by

$$\frac{d[A\text{-}CH_4]}{dt} = - k_a [O_2]^n [A\text{-}CH_4] + k_t [O_2]^n [T\text{-}CH_4], \qquad \text{(VI-1)}$$

where k_a and k_t are the rate constants which only depend on the temperature, and n is the order of reaction. For simplicity, the conversions to and from E-CH_4 are fully ignored and the

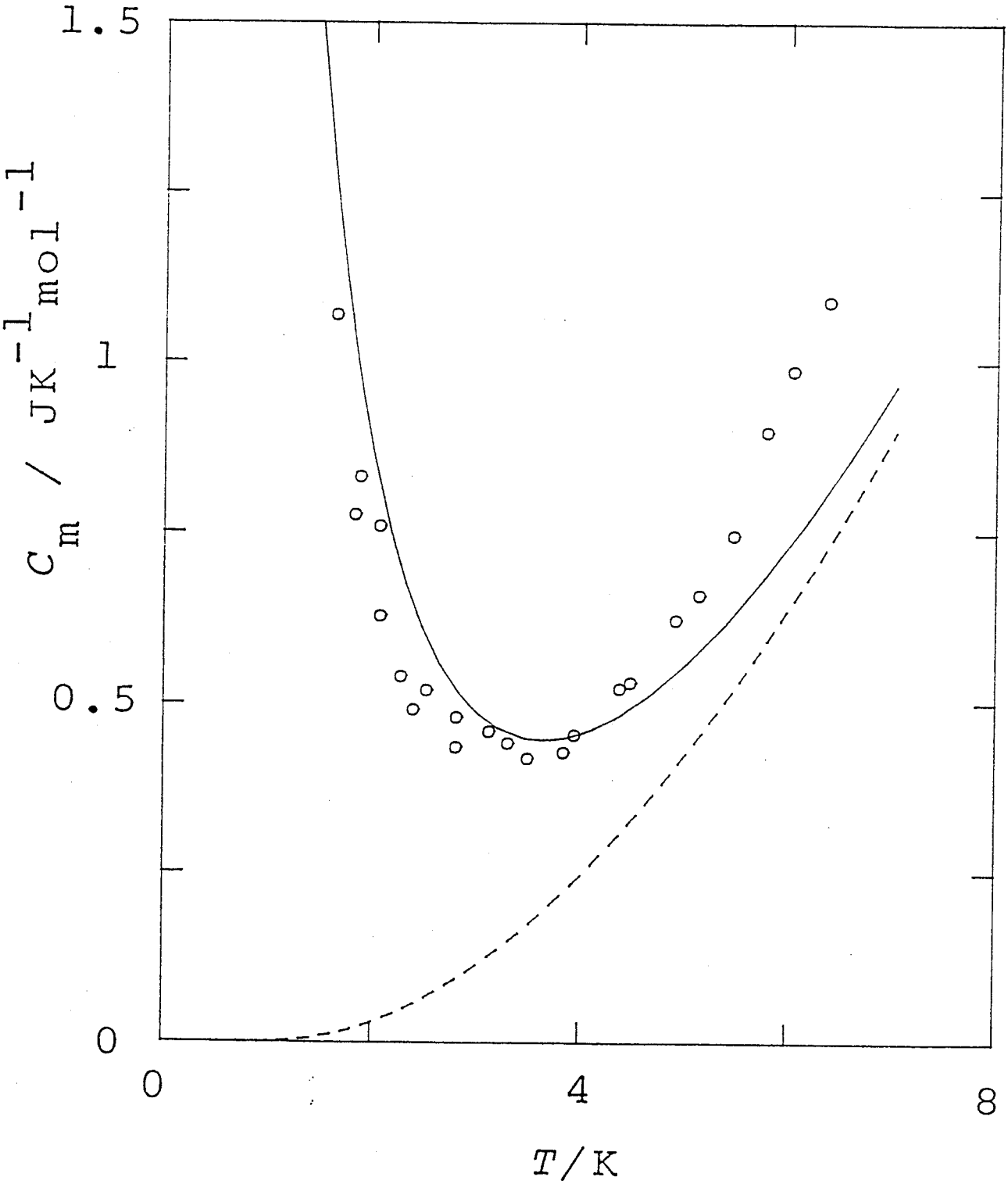

Fig. VI-9 Molar heat capacity of the commensurate CH_4 doped with 0.6 % mol of O_2: The dashed curve indicates the lattice contribution obtained for the pure CH_4. The solid curve indicates the sum of the calculated Schottky heat capacity and the lattice contribution.

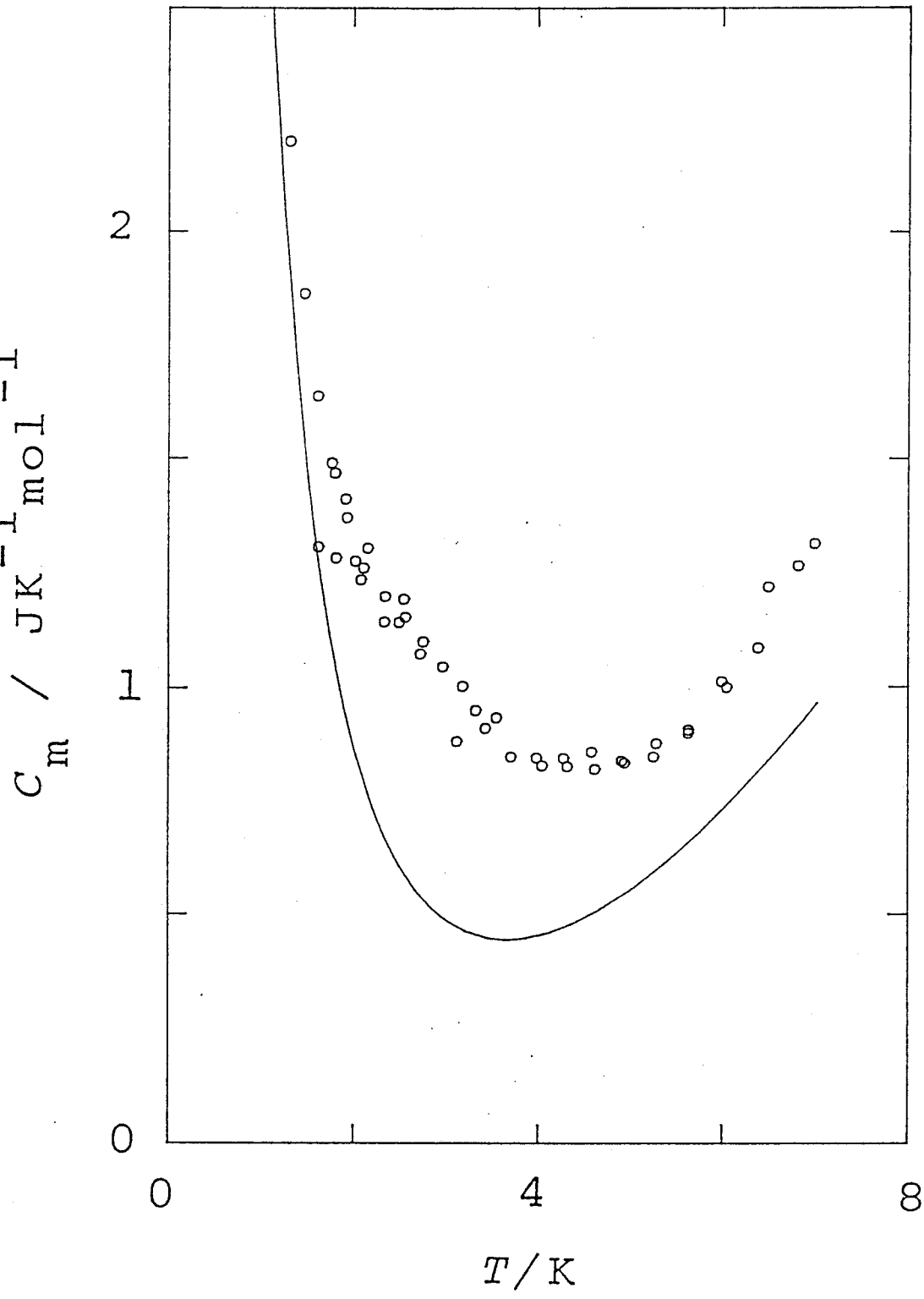

Fig. VI-10 Molar heat capacity of the incommensurate CH_4 doped with 1 mol % of O_2: The solid indicates the sum of the Schottky heat capacity calculated for the commensurate phase and the lattice heat capacity.

reaction is assumed to be the first order with respect to CH_4. When the system reaches the equilibrium, the calorimetric temperature is raised rapidly to bring the system out of equilibrium. The equation turns out to be

$$\frac{d\{[A\text{-}CH_4] + \Delta[A\text{-}CH_4]\}}{dt} = \frac{d\Delta[A\text{-}CH_4]}{dt} = -k_a [O_2]^n \{[A\text{-}CH_4]+\Delta[A\text{-}CH_4]\}$$

$$+ k_t [O_2]^n \{[T\text{-}CH_4]-\Delta[A\text{-}CH_4]\}$$

$$= -(k_a + k_t)[O_2]^n \Delta[A\text{-}CH_4] \equiv -\tau^{-1} \Delta[A\text{-}CH_4], \qquad \text{(VI-2)}$$

where τ is the relaxation time, and Δ is deviation from the equilibrium value.

As shown in Fig. VI-11, an Arrhenius plot gives a straight line for each sample with different concentration of O_2 for the commensurate phase. While the absolute value of τ becomes smaller with increasing O_2 concentration, the slope seems to be the same and gives an apparent activation energy, E_a, which is 3.5 ± 0.4 K. Here,

$$\tau^{-1} = \tau_0^{-1} \exp(-E_a/T). \qquad \text{(VI-3)}$$

The activation energy is obviously larger than the separation of tunnel splitting between the *A*- and *E*-states (= 1.7 K, ref. V-15). According to a theory dealing with the spin conversion of CH_4 (ref. 3), the activation energy should be equal to the tunnel splitting, unless the spin species are not converted with a Raman process. Two recent theories (refs. 8 and 9) suggested that the rate of spin conversion may follow such Arrhenius law at higher temperatures even in the Raman process. They explained the temperature dependence of the conversion rate for NH_4^+ embedded in a KBr matrix (ref. 10). For CH_4 on graphite, since the activation energy is much smaller than the libron energy (≃ 70 K , ref. V-14), it might be related to the electronic states of O_2. Figure VI-12 shows the Arrhenius plot for the incommensurate phase. The apparent activation energy is obtained to be 5.1 ± 0.7 K, which is also between the tunnel

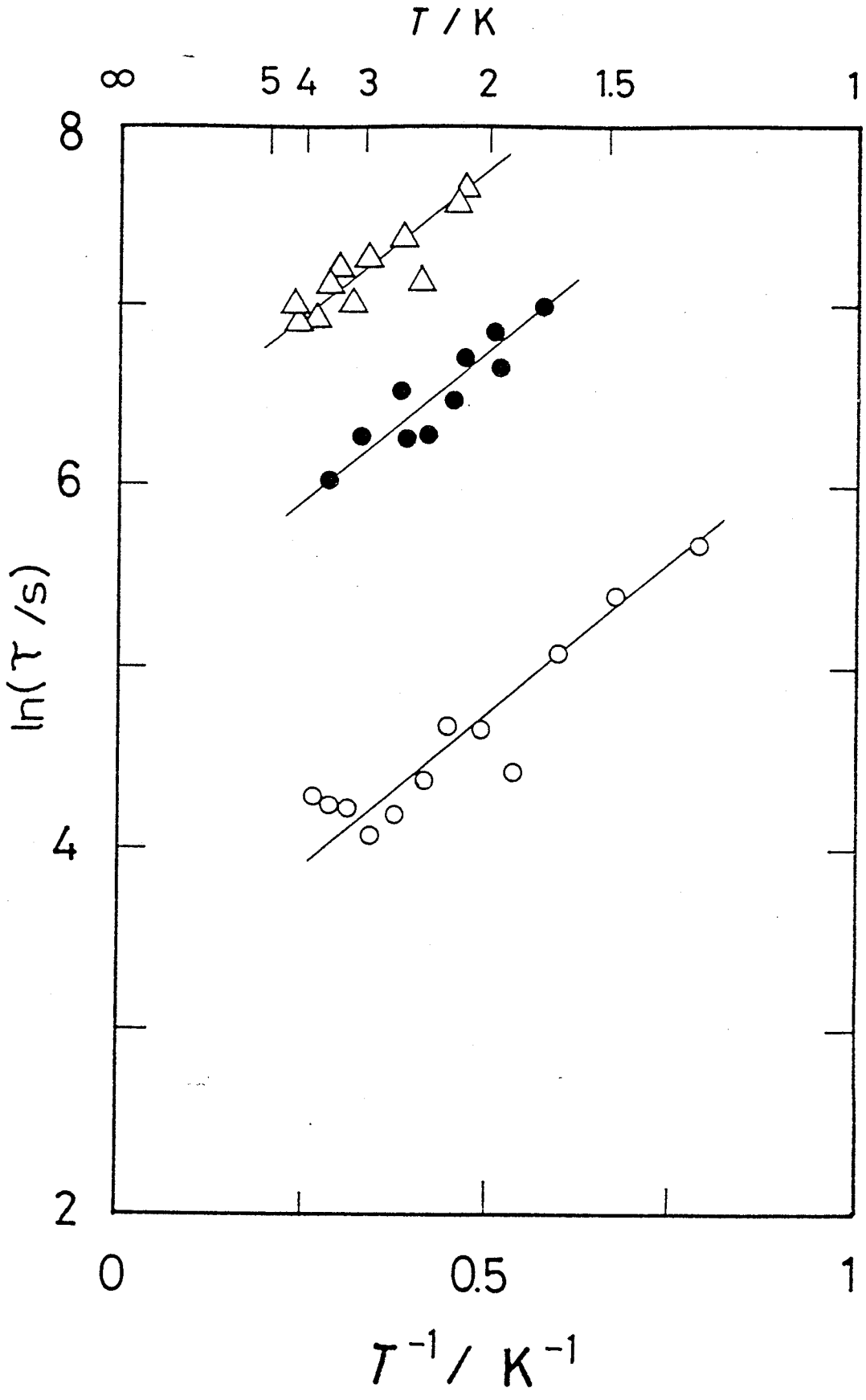

Fig. VI-11 Temperature dependence of the time constant obtained for the spin conversion in the commensurate CH_4 monolayer: o, 1.0 mol % of O_2; o, 0.66 mol % of O_2; Δ, 0.42 mol % of O_2.

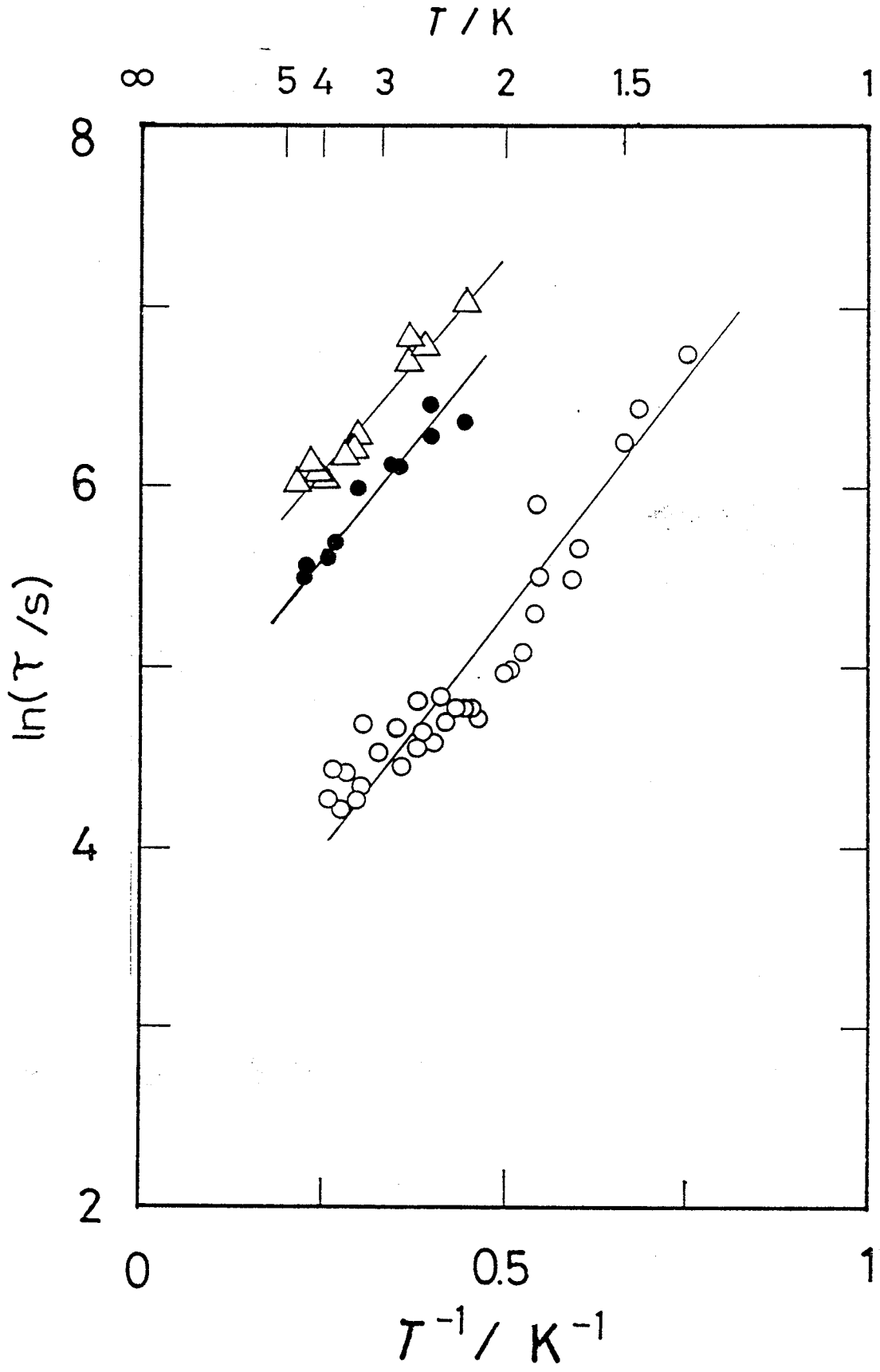

Fig. VI-12 Temperature dependence of the time constant obtained for the spin conversion in the incommensurate CH_4 monolayer: o, 1.0 mol % of O_2; o, 0.40 mol % of O_2; Δ, 0.14 mol % of O_2.

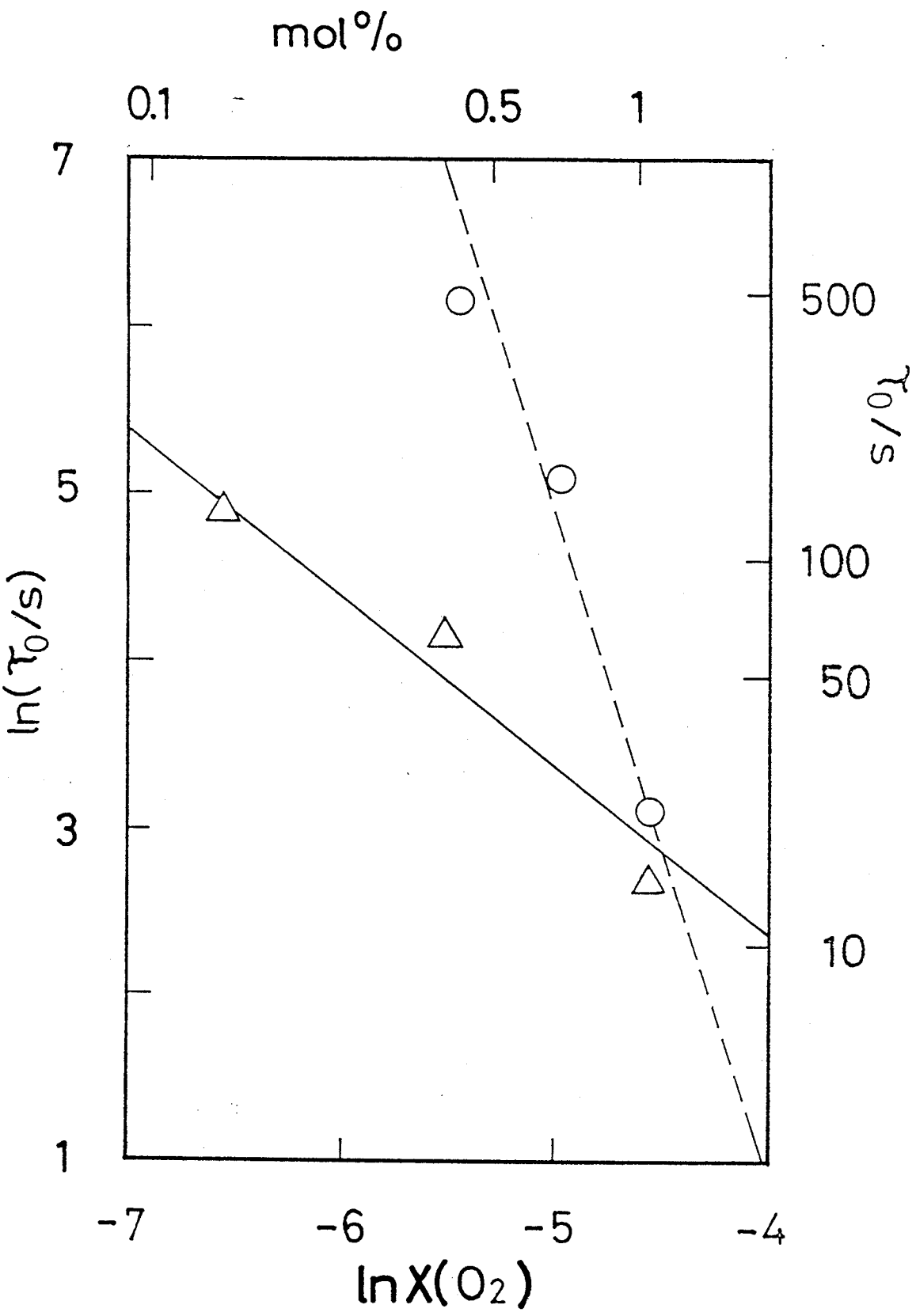

Fig. VI-13 Dependence of the pre-exponential factor for spin conversion on O_2 mole fraction x: o, commensurate phase; Δ, incommensurate phase. The solid and broken lines indicate the slope of 4 and 1, respectively.

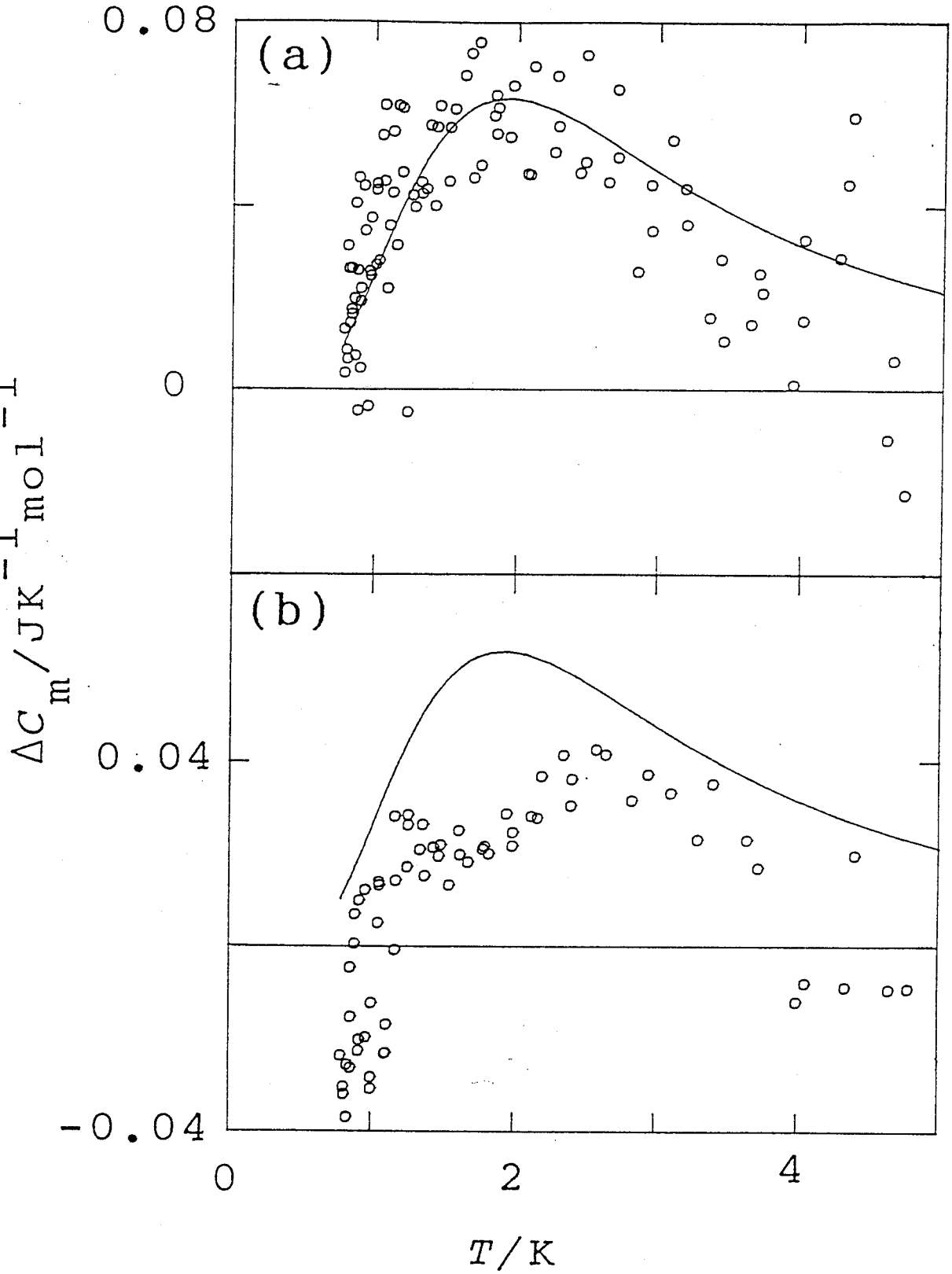

Fig. VI-14 Excess heat capacities obtained for the CD_4 monolayers containing 1 mol % of O_2. The contribution from the lattice and impurities have already been subtracted; (a) commensurate phase, (b) incommensurate phase. The solid curves indicate the Schottky heat capacity arising from the spin energy levels in the $^3\Sigma$ ground state of O_2.

splitting and the libron energy.

In order to obtain the order of the reaction from the τ_0 determined at different concentrations, a log-log plot as shown in Fig. VI-13 is useful. The slope determines the reaction order to be 4 for the commensurate phase and 1 for the incommensurate phase. The conversion process for the incommensurate phase would be of the first order, whereas that for the commensurate phase would be of higher order. Further investigation is necessary to understand the mechanism.

VI-3-4 Electronic State of O_2 in CD_4 on Graphite

Since the CD_4 sample contained CHD_3 as an impurity, the contributions from CHD_3 as well as the lattice vibrations to the heat capacity were subtracted from the total in order to see the intrinsic contribution of the dopant molecule O_2. The excess heat capacities are illustrated in Fig. VI-14 for both of the commensurate (a) and incommensurate (b) phases. They appear to be reproduced by a Schottky heat capacity function. The solid curves are the calculated ones based on the two-level Schottky heat capacity with a splitting of 5.14 K and a weight of 2 for upper level. Both of the values were the fitting parameters obtained in the case of bulk solid N_2 contaminated with O_2 (ref. 7). Conversely the fact proved that the spin splitting in the $^3\Sigma$ ground state of O_2 was observed in the present experiment and that O_2 is miscible with CD_4 on graphite.

It should be noted that the apparent activation energy for the spin conversion E_a is comparable in magnitude with the splitting of the ground state of O_2. It is also interesting that since the lower ground state of O_2 has no effective magnetic moment, and therefore has no catalytic activity for the spin conversion, the concentration of the active O_2 is increased as the temperature is raised.

References to Chapter VI

1. K. Motizuki and T. Nagamiya, *J. Phys. Soc. Jpn.* 11, 93

(1956).
2. A.J. Nijman and A.J. Berlinsky, *Phys. Rev. Lett.* 38, 408 (1977).
3. A.J. Nijman and A.J. Berlinsky, *Can. J. Phys.* 58, 1049 (1980).
4. R.F. Code and J. Higinbotham, *Can. J. Phys.* 54, 1248 (1976).
5. G.J. Vogt and K.S. Pitzer, *J. Chem. Thermodyn.* 8, 1011 (1976).
6. P. Van Hecke, P. Grobet and L. Van Gerven, *J. Magn. Reson.* 7, 117 (1972).
7. J.C. Burford and G.M. Graham, *J. Chem. Phys.* 49, 763 (1968).
8. W. Häusler, *Z. Phys.* B - *Condensed Matter* 81, 265 (1990).
9. A. Würger, *Z. Phys.* B - *Condensed Matter* 81, 273 (1990).
10. A. Inaba, H. Chihara, J.A. Morrison, H. Blank, A. Heidemann and J. Tomkinson, *J. Phys. Soc. Jpn.* 59, 522 (1990).

Chapter VII General Discussion

VII-1 Two-dimensional Lattice Vibrations

By means of a series of calorimetric investigations on the physisorbed monolayers, a common property has been elucidated as follows. The two-dimensional lattice vibrations of the admolecules are significantly affected by the corrugation of the substrate, particularly for the commensurate structure. The effect depends both on the admolecules and the substrates. Our calorimetric method can be an alternative to the inelastic neutron scattering to determine the cut-off at the low-frequency end in the phonon density of states, unless the heat capacity at low temperatures, say below 10 K, is contaminated by any anomaly. A large coherent region of the substrate is also necessary to avoid the size effect.

VII-2 Miscibility in Two-dimensional System

The miscibility in molecular solids is one of the tough problems to be solved. Sometimes calorimetry proves to be powerful in the clarification. The investigation of the miscibility in two-dimensional system is rather challenging because little is known about the structure and property. Both the heat capacity and the mixing entropy may allow us to understand what happens in the mixture. Low energy excitations are particularly useful as a probe.

VII-3 Two-dimensional Phase Transition

Calorimetry is still a powerful tool to characterize the phase transition in two-dimensional systems as well as the bulk systems. The phase diagram of the adsorbed monolayers is unknown for most of the systems yet. A new phase which can not be realized in the bulk system may be found as in the case of CO on graphite. Since a subtle balance of the molecular interactions is kept in the adsorbed system, the investigation may enable us to understand them more in detail.

Chapter VIII Summary

We first investigated calorimetrically the system of Kr monolayer on graphite. The vibrational states of the monolayer can be described by single Einstein mode, which is due to the vibrations perpendicular to the surface, as well as in-plane collective modes. For the latter, the phonon density of states has two cut-offs both at low and high frequency ends. In the commensurate phase, the cut-off at low-frequency end provides useful information on the amplitude of the surface corrugation. A re-entrant fluid phase was found between the commensurate and the incommensurate phases.

For the system of N_2 on graphite, an appropriate dynamical consideration was given to the vibrational states of the three phases; the commensurate, the uniaxially compressed incommensurate and the triangular incommensurate phases. An orientational order-disorder phase transition with respect to the molecular axis was found in the triangular incommensurate phase.

The CO/N_2 mixture was found to be miscible even on the surface of graphite. An analysis of the mixing entropy indicated that they form a Wannier lattice.

For the CH_4 on graphite, the rate of spin conversion was very slow. It was accelerated significantly by introducing O_2 as a magnetic impurity as in the case of bulk system. The splitting of the electronic ground state of O_2 may be responsible for the conversion. The heat capacity including that of the spin system was obtained for both of the commensurate and incommensurate phases.